

# **Robust Waveform Design for MIMO Radar from Information Theoretic and Machine Learning Principles**

Dissertation zur Erlangung des Grades eines Doktor-Ingenieurs  
der Fakultät für Elektrotechnik und Informationstechnik an  
der Ruhr-Universität Bochum

von

Aya Mostafa Ibrahim Ahmed  
aus Kairo, Ägypten

1. Bericht: Prof. Dr.-Ing. Aydin Sezgin
2. Bericht: Prof. Moeness Amin
3. Bericht: Prof. Henk Wymeersch

Tag der mündlichen Prüfung: 14.03.2022



Lehrstuhl für Digitale Kommunikationssysteme  
Ruhr-Universität Bochum

2022



# Contents

<b>Acknowledgement</b>	<b>v</b>
<b>Abstract</b>	<b>vii</b>
<b>Kurzfassung</b>	<b>ix</b>
<b>Abbreviations and Notation</b>	<b>x</b>
<b>Abbreviations and Notation</b>	<b>xi</b>
<b>1 Introduction</b>	<b>1</b>
1.1 Motivation and Objective . . . . .	1
1.2 Outline and Contributions . . . . .	4
1.3 Contributions Outside the Scope of the Thesis . . . . .	7
<b>2 Preliminaries</b>	<b>11</b>
2.1 Overview of Waveform design for MIMO Radars . . . . .	11
2.1.1 MIMO Radars . . . . .	11
2.1.2 Waveform Design Metrics . . . . .	12
2.2 Information Theory and Radar . . . . .	13
2.2.1 Mutual Information . . . . .	13
2.3 Majorization Basic Definitions . . . . .	14
2.4 Cognitive Radar (CR) . . . . .	16
2.5 Machine Learning (ML) and Radar . . . . .	16
2.5.1 ML: Neural Networks (NN) . . . . .	17
2.5.2 ML: Reinforcement Learning (RL) . . . . .	19
2.6 Direction of Arrival (DOA) . . . . .	20
2.6.1 System Model . . . . .	20
2.6.2 Beamforming Methods: Minimum Variance Distortionless Response (MVDR) . . . . .	22
2.6.3 Subspace Methods: Multiple-Signal Classification (MUSIC) . . . . .	22
<b>3 Mutual Information (MI) based MIMO Radar Beamforming</b>	<b>25</b>
3.1 Why MI is a good metric for waveform design ? . . . . .	25
3.2 Related Work . . . . .	26
3.3 Transmit - Receive Beamforming . . . . .	28
3.3.1 Colocated MIMO Radar System Model . . . . .	29

3.3.2	Optimization Problem . . . . .	32
3.3.3	Numerical Analysis . . . . .	36
3.3.4	Beamforming design only . . . . .	37
3.4	Impact of Spatial Correlation . . . . .	39
3.4.1	Statistical MIMO Radar System Model . . . . .	39
3.4.2	Measure of Spatial correlation of MIMO Radar . . . . .	43
3.4.3	The Effect of Spatial Correlation on MI-based waveform . . . . .	45
3.4.4	Numerical Analysis . . . . .	48
3.4.5	Spatially Correlated MIMO Radar Setup . . . . .	49
3.5	Summary . . . . .	50
<b>4</b>	<b>RL based cognitive Beamforming</b>	<b>53</b>
4.1	Related Work . . . . .	53
4.2	Problem Formulation . . . . .	55
4.2.1	System Model . . . . .	55
4.2.2	Disturbance Model . . . . .	56
4.2.3	Detection Problem . . . . .	57
4.3	RL-Based Massive MIMO CR . . . . .	58
4.3.1	SARSA Algorithm and Target Detection . . . . .	58
4.3.2	The set of States . . . . .	59
4.3.3	The Set of Actions . . . . .	59
4.3.4	The Reward . . . . .	60
4.3.5	Policy . . . . .	62
4.4	Optimization Problem . . . . .	63
4.5	Numerical Analysis . . . . .	65
4.5.1	Simulation Setup . . . . .	66
4.5.2	Disturbance Model . . . . .	67
4.5.3	Study Case 1 : Stationary Environment . . . . .	67
4.5.4	Dynamic Environment . . . . .	73
4.5.5	Robustness . . . . .	79
4.5.6	Varying the Disturbance non-Gaussianity Levels . . . . .	81
4.5.7	Varying the Order of Auto-Regressive (AR) Process . . . . .	82
4.6	Summary . . . . .	84
<b>5</b>	<b>Deep Learning based DOA for Small MIMO Antenna Arrays</b>	<b>85</b>
5.1	Related Work . . . . .	85
5.2	System Model . . . . .	86
5.3	Deep Learning Architecture . . . . .	88
5.3.1	Can the same DNN estimate the DOA directly ? . . . . .	90
5.3.2	Computational Complexity . . . . .	90
5.4	Numerical Analysis . . . . .	90
5.4.1	Deep Neural Network (DNN) Performance Analysis . . . . .	91
5.4.2	DOA Performance . . . . .	93
5.4.3	Cramér Rao Bound (CRB) Analysis . . . . .	96

---

5.4.4	The Best Training Signal-to-Noise ratio (SNR) Values . . . . .	97
5.5	Summary . . . . .	98
<b>6</b>	<b>Deep Learning for DOA for Coherent Targets using Imperfect Antenna Array</b>	<b>101</b>
6.1	Related Work . . . . .	101
6.2	Array Imperfections . . . . .	102
6.3	Multipath . . . . .	103
6.4	DOA based on Deep Learning . . . . .	104
6.4.1	DNN Architecture . . . . .	104
6.4.2	Learning Scheme . . . . .	106
6.4.3	Training Process . . . . .	107
6.4.4	Scanning . . . . .	107
6.5	Numerical Analysis . . . . .	108
6.5.1	Gain Responses of each Decoder (i.e., Filter) . . . . .	108
6.5.2	Performance against Spatial Smoothing-MUSIC . . . . .	109
6.5.3	Performance against Algorithm in [LZY18a] . . . . .	110
6.6	Summary . . . . .	110
<b>7</b>	<b>Conclusion and Future Work</b>	<b>111</b>
7.1	Summary of Main Contributions . . . . .	111
7.2	Future Work Directions . . . . .	112
	<b>Appendix</b>	<b>115</b>
A.1	Asymptotic distribution of $\Lambda_{b,RW}^k$ . . . . .	115
A.2	Proof of Proposition 1 . . . . .	115
	<b>Bibliography</b>	<b>117</b>
	<b>Curriculum Vitae</b>	<b>125</b>
	<b>List of Publications</b>	<b>127</b>



# Acknowledgement

First of all, I am very grateful for Prof. Dr.-Ing. Aydin Sezgin for giving me the opportunity to pursue my PhD within his institute. I would like to further express my gratitude for our fruitful discussions, his guidance and support throughout my PhD journey. Besides my supervisor, I would like to thank Prof. Moeness Amin and Prof. Henk Wymeersch for reviewing the thesis.

Many sincerest thanks to Dr. Stefano Fortunati for his support.

I would like to thank the Deutsche Forschungsgemeinschaft (DFG) for supporting this work financially.

Special thanks to my colleagues at the chair of Digital Communication Systems for the insightful discussions and ideas exchange.

Last but not least, I wish to express my gratitude to my family for their endless love. My life time supporter, my mother, I would not be who i am if it was not for you, words are not enough to thank you. My husband Dr. Ing Abdelfattah Megahed, your endless love and support is what keeps me going forward, I cant describe my love and gratitude to you, thanks for everything you have done to me. Thanks to my father and brother. For my beautiful daughters Lara and Lina, you are the sunshine of my life, i love you.





# Abstract

In recent years, radar has emerged as a key technology for many civilian applications, for instance, autonomous driving, industrial monitoring, urban sensing and assisted living for elderly. However, many problems related to interference mitigation, detection within clutter, antennas imperfections and poor resolution remain fundamental challenges. Hence, there is a pushing need to develop innovative, efficient and robust signal processing techniques to solve inherent radar challenges.

A crucial element affecting a radar operation is the surrounding environment. The undesired returns from the environment can result from mutual interference between targets or clutter due to terrain scattering. Correspondingly, those returns can greatly degrade the radar systems performance. In this regard, the waveform diversity offered by MIMO radar is exploited where each antenna can transmit different waveform, that can be adapted dynamically to the surrounding environment. To this end, the existence of a priori information about the surroundings is crucial for the classical waveform design. In this thesis, we tackle this problem proposing different strategies based on the radar operation mode and the priori information available. Those strategies are stemmed from information theory and machine learning perspectives proposing novel and robust solutions for the current environmental challenges facing radar systems. This dissertation intensively discusses those strategies within two main parts. In the first part, we assume the radar scene consists of spatially close multiple extended targets, whose spectrum overlaps in the frequency domain while the radar's goal is to identify those targets. However, high interference might obstruct the information extraction, and directing the beamformers towards the targets' locations as in conventional beamforming might not be convenient in this case. Thus, we propose a joint information-theoretic transmit-receive beamforming design, where we utilize mutual information (MI) as a metric to design beamformers. We devise an optimization procedure to maximize the MI between the target returns and the received signal. Interestingly, our results show that MI is greatly affected by how spatially near the targets are. For a deeper understanding of those findings, we further mathematically analyze the prominent effect of MI on spatial correlation, which is shown to vary based on the signal to noise ratio regime (SNR).

In the second part, we reconsider the availability of a priori information. In this regard, we assume the radar is in detection mode, with no information about the surroundings nor the targets. An additional encountered difficulty is the presence of an unknown dynamic environment, where the targets can change their directions and fade away. Furthermore, we assume the presence of disturbance (clutter plus noise) of unknown statistics. Thus, a model based approach as proposed in the first part would be too complicated and simplified models would be prone to mismatches.

Therefore, we address this problem utilizing the advances of reinforcement learning (RL) to explore unknown environments. Herein, the radar acts as an agent which interacts with the unknown dynamic environment and learns through trial and error. Subsequently, the agent develops its own behavior rules based on the experience gained from this interaction. Those rules are then used to optimize the transmit beamformers for cognitive multi-target detection. We further prove the robustness of such approach across different harsh environments and sophisticated disturbance models.

Motivated by our interesting findings in machine learning, this thesis further seeks the potential of utilizing data driven approaches to tackle several challenges related to direction of arrival estimation (DOA). In general, it is difficult to enhance the resolution of the current DOA algorithms without either increasing the number of antennas or the antenna array aperture. However, for many applications, such requirement might be problematic, thus we present a more efficient alternative. This thesis proposes to use the received signal of a small number of antennas to extrapolate the received signal of other virtual antennas using a novel deep neural network (DNN) architecture. Our findings show that a small antenna array can notably achieve the resolution of a larger one. In addition the DNN can even de-noise the received signal in the prediction procedure. This one particular advantage arising from using DNNs can be further utilized to remove distortions in the received signals. For instance, multipath and array imperfections are considered two of the foremost sources of signal distortions affecting DOA precision and accuracy. In this regard, we propose a DNN framework enhancing the performance of the state of the art multiple signal classification (MUSIC) algorithm. Such solution enables MUSIC to resolve coherent sources resulting from multipath and at the same time overcome the errors arising from imperfections of the antenna array.

# Kurzfassung

In den letzten Jahren hat sich das Radar als Schlüsseltechnologie für viele zivile Anwendungen herauskristallisiert, z. B. für das autonome Fahren, die industrielle Überwachung, die Stadtüberwachung und das betreute Wohnen für ältere Menschen. Viele Probleme im Zusammenhang mit der Störungsminde rung, der Erkennung in Stör-signalen, der Unzulänglichkeit der Antennen und der geringen Auflösung stellen jedoch nach wie vor grundlegende Herausforderungen dar. Daher besteht ein dringender Bedarf an der Entwicklung innovativer, effizienter und robuster Signalverarbeitungstechniken, um die mit dem Radar verbundenen Herausforderungen zu lösen.

Ein entscheidendes Element, das den Betrieb eines Radars beeinflusst, ist die Umgebung. Unerwünschte Reflektionen aus der Umgebung können durch gegenseitige Interferenzen zwischen Zielen oder durch Störungen aufgrund von Geländestreunungen entstehen. Dementsprechend können diese Reflektionen die Leistung des Radarsystems erheblich beeinträchtigen. In diesem Zusammenhang wird die Wellenformdiversität des MIMO-Radars genutzt, bei der jede Antenne eine andere Wellenform übertragen kann, die dynamisch an die Umgebung angepasst werden kann. Zu diesem Zweck ist das Vorhandensein von A-priori-Informationen über die Umgebung ein entscheidender Faktor für den klassischen Wellenformwurf. In dieser Arbeit gehen wir dieses Problem an und schlagen verschiedene Strategien vor, die auf der Betriebsart des Radars und den verfügbaren Vorabinformationen basieren. Diese Strategien stammen aus der Informationstheorie und der Perspektive des maschinellen Lernens und bieten neuartige und robuste Lösungen für die aktuellen Herausforderungen, denen sich Radarsysteme in der Umwelt stellen müssen. In dieser Dissertation werden diese Strategien in zwei Hauptteilen intensiv diskutiert. Im ersten Teil gehen wir davon aus, dass die Radarszene aus mehreren, räumlich nahen, ausgedehnten Zielen besteht, deren Spektrum sich im Frequenzbereich überschneidet, während das Ziel des Radars darin besteht, diese Ziele zu identifizieren. Starke Interferenzen können jedoch die Informationsgewinnung behindern, und die Ausrichtung der Beamformer auf die Standorte der Ziele, wie beim herkömmlichen Beamforming, ist in diesem Fall nicht sinnvoll. Daher schlagen wir ein gemeinsames informationstheoretisches Sendempfangs-Beamforming-Design vor, bei dem wir die Transinformation als Metrik für das Design von Beamformern verwenden. Wir entwickeln ein Optimierungsverfahren zur Maximierung der Transinformation zwischen dem Zielsignal und dem empfangenen Signal. Interessanterweise zeigen unsere Ergebnisse, dass die Transinformation stark davon beeinflusst wird, wie nah die Ziele räumlich beieinander liegen. Um diese Ergebnisse besser zu verstehen, analysieren wir darüber hinaus mathematisch die herausragende Wirkung von Transinformation auf die räumliche Korrelation, die

nachweislich in Abhängigkeit des Signal-Rausch-Verhältnisses (SRV) variiert.

Im zweiten Teil betrachten wir die Verfügbarkeit von A-priori-Informationen. Dabei gehen wir davon aus, dass sich das Radar im Erfassungsmodus befindet und keine Informationen über die Umgebung oder die Ziele vorliegen. Eine weitere Schwierigkeit ist das Vorhandensein einer unbekannt dynamischen Umgebung, in der die Ziele ihre Richtung ändern und verschwinden können. Außerdem gehen wir davon aus, dass Störungen (Clutter plus Rauschen) mit unbekannter Statistik vorhanden sind. Ein modellbasierter Ansatz, wie er im ersten Teil vorgeschlagen wurde, wäre daher kompliziert, und vereinfachte Modelle wären anfällig für Unstimmigkeiten. Daher gehen wir dieses Problem an, indem wir die Fortschritte des Reinforcement Learning (RL) nutzen, um unbekannte Umgebungen zu erkunden. Dabei agiert das Radar als Agent, der mit der unbekannt dynamischen Umgebung interagiert und durch Versuch und Irrtum lernt. Anschließend entwickelt der Agent seine eigenen Verhaltensregeln auf der Grundlage der aus dieser Interaktion gewonnenen Erfahrungen. Diese Regeln werden dann verwendet, um die Sendestrahler für die kognitive Mehrzielerfassung zu optimieren. Wir beweisen außerdem die Robustheit eines solchen Ansatzes in verschiedenen rauen Umgebungen und bei anspruchsvollen Störungsmodellen.

Motiviert durch unsere interessanten Erkenntnisse im Bereich des maschinellen Lernens, wird in dieser Arbeit das Potenzial datengesteuerter Ansätze zur Bewältigung verschiedener Herausforderungen im Zusammenhang mit der Schätzung der Ankunftsrichtung (DOA) untersucht. Im Allgemeinen ist es schwierig, die Auflösung der aktuellen DOA-Algorithmen zu verbessern, ohne entweder die Anzahl der Antennen oder die Öffnung des Antennenfeldes zu erhöhen. Für viele Anwendungen könnte eine solche Anforderung jedoch problematisch sein, weshalb wir eine effizientere Alternative vorstellen. In dieser Arbeit wird vorgeschlagen, das Empfangssignal einer kleinen Anzahl von Antennen zu verwenden, um das Empfangssignal anderer Antennen mit Hilfe einer neuartigen Deep Neural Network (DNN) Architektur zu extrapolieren. Unsere Ergebnisse zeigen, dass eine kleine Antennengruppe die Auflösung einer größeren erreichen kann. Darüber hinaus kann das DNN das empfangene Signal bei der Vorhersage sogar entzaubern. Dieser besondere Vorteil, der sich aus der Verwendung von DNNs ergibt, kann weiter genutzt werden, um Verzerrungen in den empfangenen Signalen zu entfernen. Zum Beispiel werden Mehrwegeeffekte und Array-Unvollkommenheiten als zwei der wichtigsten Quellen von Signalverzerrungen angesehen, die die DOA-Präzision und Genauigkeit beeinträchtigen. In diesem Zusammenhang schlagen wir einen DNN-Framework vor, der die Leistung des modernen Algorithmus zur Klassifizierung mehrerer Signale (MUSIC) verbessert. Eine solche Lösung ermöglicht es MUSIC, kohärente Quellen, die aus Mehrwegeeffekten resultieren, aufzulösen und gleichzeitig die Fehler zu überwinden, die durch Unzulänglichkeiten der Antennengruppe entstehen.

# Abbreviations and Notation

## Symbols

$P_D$	probability of detection
$P_{Fa}$	probability of false alarm
<b>AE</b>	autoencoder
<b>AR</b>	auto-regressive
<b>ARMA</b>	Auto regressive-moving average
<b>BCD</b>	block coordinate descent
<b>CFAR</b>	constant false alarm rate
<b>CR</b>	cognitive radar
<b>CRB</b>	Cramér Rao bound
<b>DNN</b>	deep neural network
<b>DOA</b>	direction-of-arrival-estimation
<b>DoF</b>	degrees of freedom
<b>FMCW</b>	Frequency modulated Continuous Waveform
<b>GLRT</b>	<i>generalized likelihood ratio test</i>
<b>ICA</b>	inner convex approximations
<b>KKT</b>	Karush-Kuhn-Tucker
<b>MDP</b>	Markov decision process
<b>MI</b>	mutual information
<b>MIMO</b>	multiple-input multiple-output
<b>ML</b>	machine learning
<b>MMIMO</b>	massive multiple input multiple output
<b>MMSE</b>	minimum-mean squared error
<b>MSE</b>	mean-squared error
<b>MUSIC</b>	multiple-signal classification
<b>MVDR</b>	minimum variance distortionless response
<b>NN</b>	neural network
<b>PSD</b>	power spectral density

<b>RCS</b>	radar cross section
<b>ReLU</b>	rectified linear unit
<b>RIS</b>	reconfigurable intelligent surface
<b>RL</b>	Reinforcement Learning
<b>RMSE</b>	root mean square error
<b>ROC</b>	receiver operating characteristics
<b>Rx</b>	receiver
<b>SARSA</b>	state-action-reward-state-action
<b>SDP</b>	semi-definite programming
<b>SINR</b>	signal-to-interference-and-noise ratio
<b>SNR</b>	signal-to-noise ratio
<b>SS-MUSIC</b>	spatial smoothing MUSIC
<b>TL</b>	training loss
<b>Tx</b>	transmitter
<b>UAV</b>	unmanned vehicles
<b>ULA</b>	uniform linear array
<b>VL</b>	validation loss

# 1 Introduction

## 1.1 Motivation and Objective

For decades radar has played a significant role in military and security applications. However, its development has gradually broadened to include civilian applications, including traffic control, indoor surveillance, and urban sensing. Furthermore, radar has become a key technology for the ongoing advances of autonomous driving. In fact, the fast-growing market of fully autonomous vehicles has fueled the ongoing interest to develop innovative signal-processing techniques for radar systems. It is foreseeable that if the technical issues are resolved, by 2030 up to 15 % of the cars could be fully autonomous [Mck].

The term radar is stemmed from the acronym *RA*dio *D*etection *A*nd *R*anging, where a classical radar transmits electromagnetic waves to illuminate a certain area. The reflected waves are then exploited to detect targets, providing range and speed measurements. With multiple antennas, radars can also estimate the **direction-of-arrival-estimation (DOA)** which enables along with the range information both target detection and localization. As a matter of fact, the recent leap in computing architectures and high-speed processors have enabled the application of sophisticated and effective signal processing methodologies to render even further information. Specialized radars nowadays can even perform signature analysis providing details on the shape, size, and components of the target as well as its material composition. This has opened the door for further radar applications such as through-the-wall imaging, indoor monitoring for vital signs detection, and assisted living for elders [Ami17]. Despite the significant advances in radar signal processing, there are still several inherent challenges facing the current radar systems hindering the further development of radar for those new areas. The undesired returns from the surrounding environment remain one major challenge as it is a key performance degradation factor. Those returns can appear in many forms, for instance, they can result due to mutual interference between targets that might be all of the equal importance within the illumination area. Another form would be clutter originating from terrain scattering, which is of no interest to the radar, user due to reflections from the operating radar or other radar or wireless systems. The radar must distinguish *true* targets from other objects, however, the fore-mentioned reflections might be mistaken for a genuine target, hence generating a false alarm. Furthermore, strong clutter reflections can even mask far-range targets leading to a missed detection.

Such a problem can be tackled by appropriately managing the radar-transmitted radiation power. This is done through shaping a desired transmit beampattern

that minimizes clutter and interference from other targets. This can be achieved primarily if the transmitted beampattern has a null in the interference direction, consequently, it can be eliminated by the receiver enhancing the target's detection. Traditional phased array radar focuses the transmitted beam in the direction of the expected target by changing the relative phases of the transmitted waveform from the transmit antennas [GDH<sup>+</sup>15]. However, if the interference source is near the target direction, phased array radars will be incapable of simultaneously mitigating sources of interference and at the same time efficiently detecting the existing targets. This is due to the fact that the transmitter must focus the beampattern forming a phase front in the target direction. Unlike phased array radar, **multiple-input multiple-output (MIMO)** radar has the ability to transmit an independent waveform from each antenna. This waveform can be chosen freely, either to maximize the power at the target locations or minimize the cross-correlation among the reflected signals at the receiver [Fri12a, BF03, LS07]. At each receive antenna, all the returns are processed using  $M$  different matched filters. Each of those filters is matched to the  $M$  independent transmitted waveforms. Thus, for every **transmitter (Tx)-receiver (Rx)** antenna pair, the channel properties can be processed (i.e., virtual array [LS07]). This waveform diversity empowered MIMO radar with superiority in multiple aspects compared to phased array radar, including higher parameter identifiability, flexible transmit beampattern design, and direct applicability of adaptive localization and parameter estimation techniques. For those reasons, in the past several years the research in waveform diversity has intensely flourished. With the aid of the latest advances in digital waveform generators and solid-state transmitters, the transmitted waveform can be dynamically adapted to optimize radar performance for certain tasks and scenarios. Fundamentally, the optimal waveform design problem can be casted according to a certain desired performance criterion. For instance, the waveform can be optimized to improve robustness to clutter or interference or to enhance detection [Fri07]. The radar design is usually driven by assumed models of target and interference plus noise environment. Those models are known a priori in some scenarios, possibly based on previous radar experiences, whereas in other scenarios, the radar has to interpret the environment without any prior knowledge sources. An important question here is how the waveform can be designed in both cases (i.e., known and unknown environments) to provide robustness across various sources of interference.

In this thesis we exploit both cases to provide an answer to this question. The known environment case is exploited in chapter 3, where we assume that the Tx has prior knowledge of the targets' second-order statistics, locations and their number. This scenario can be explained in a target identification mode, assuming it has already been detected. In other words, the primary goal here is to extract more information about a certain target decreasing the a priori uncertainty about it. In this case, an appropriate metric to design the waveform is to maximize the amount of information retrieved about each target. In this sense, information theory is known to provide a method to quantify the decrease in the uncertainty about a certain random variable [FG12]. In section 3.3, the surrounding environment consists of two closely



spaced extended targets mutually interfering with each other plus noise. To maximize the mutual information between the received signal and the target signature, we jointly design the transmit-receive beamformers. The results show that optimizing the beamformers for very close targets significantly affected the **mutual information (MI)**. This motivated further analysis on how spatial correlation affects the **MI** in section 3.4. Using the notions of majorization theory, we prove mathematically that **MI** has a changing behavior with respect to the spatial correlation of the target matrix elements.

In chapter 4, the latter case of an unknown environment is exploited. We assume that the surrounding scene consists of multiple point targets plus clutter and noise. The environment is further assumed to be non-stationary and totally unknown. In fact, the radar has no prior information about the number of targets, their locations, and clutter statistics. The radar here is in a target acquisition mode, where the receiver blindly performs multi-target detection. Here, we make use of the current advances in machine learning, where **Reinforcement Learning (RL)** techniques can offer a solution to such a problem. **RL** is a learning approach that addresses model-free problems through using a software-defined agent, which learns from the observations collected from the environment and takes the best possible action according to a reward function [SB18]. By utilizing a cognitive **MIMO** radar system as this software agent, it can develop its own behavior rules gaining environmental experience driven by those observations. This experience can be then passed to the transmitter to optimize the transmitted waveforms to maximize the **probability of detection ( $P_D$ )** through a perception-action cycle of cognition. Due to the non-stationarity of the environment, this cycle is repeated continuously. Our algorithm shows robustness regardless of the disturbance statistics in stationary and non-stationary cases.

In chapter 4, a massive **MIMO** radar system model is adopted, where the performance of the algorithm is assessed as the number of virtual transmit-receive spatial channels  $N_v$  increase asymptotically. Our findings proved that as  $N_v$  increases, the **probability of false alarm ( $P_{Fa}$ )** decreases asymptotically ( $N_v \rightarrow \infty$ ) till it reaches the nominal value while the  $P_D$  increases. Furthermore, in [HBH10] it has been shown that the target localization accuracy increases as the number of antennas increases as well as the clutter suppression capabilities. In addition, [HBH10] concludes that more antennas provide better resolution. The question here is: can we enhance the estimation accuracy and increase the resolution without increasing the number of antennas? This is possible by increasing the antenna array aperture using sparse arrays. In [WYWL14, LV18, PV10] several sparse arrays structures are presented, showing that it is possible to use fewer antennas in a large aperture to provide similar performance to a linear filled array. Although such an approach provides a low hardware cost solution, however, it is characterized by its large aperture size, which might not be preferable if compactness is the driving design requirement. In this regard, we propose a novel solution to this problem in chapter 5 using deep learning. Our approach employs deep learning for reconstructing the signals of a virtual large antenna array. The algorithm uses the received signal of a small antenna array to extrapolate the received signal of other antennas in a larger antenna array.

In other words, we try to emulate the received signal of a large ULA using only a significantly smaller sub-array, without the need to increase the array aperture size, through training a deep neural network. Such a solution can enhance the angular resolution and target detection while satisfying both the low cost and compactness requirements. Furthermore, we prove that such technology can be used to boost the DOA estimation accuracy of a small antenna array. Surprisingly, our results show that the deep neural network has further denoising capabilities, as the performance obtained by using actual high antenna arrays is not only tightly approximated, but exceeded at low SNR for high angle ranges.

Motivated by the key strengths of deep learning in denoising the input signals, in chapter 6 we propose using deep learning to overcome two of the most common challenges facing the State-of-the-art DOA algorithms (i.e. coherent sources and array imperfections). In general, the current DOA estimation algorithms encounter several problems such as accuracy and precision of estimates in non-ideal scenarios, e.g., multipath and antenna imperfections. For instance, in the presence of multipath propagation, the signal coming directly from the target and the corresponding multipath signal becomes correlated. In such a scenario, the rank of the received signal covariance matrix is less than the number of impinging signals, which significantly affects the estimation performance. This is due to the fact that most of the existing state-of-the-art algorithms require a full rank covariance matrix to output an accurate estimation [LWS05, TC13]. Spatial smoothing techniques have been widely applied to solve this problem de-correlating the received signals, however, this adds more processing overhead, which might be a limiting factor in real-time applications. Another major challenge is antenna array imperfections which generally occur in practical applications due to the non-idealities in the antenna array such as mutual coupling, gain and phase gradual changes over time and as well as changes in the antenna locations. Along with multipath, those two challenges affect the DOA estimation greatly. Hence, we proposed deep learning as a unique solution to both problems yielding a robust DOA estimation without the need for any pre-processing in real-time. Fundamentally, neural networks are only trained once, then they can be directly used for estimation.

In the following, we provide the outline and contributions of this thesis.

## 1.2 Outline and Contributions

As previously discussed, there are several challenges facing the current radar systems. This thesis's primary focus is to design and optimize the transmitted waveform based on information theory and machine learning perspectives that is robust against possible sources of interference and clutter. Furthermore, we provide an analysis of how the information retrieved about the target can be affected by spatial correlation. In addition, we utilize machine learning capabilities to enhance the DOA performance at the receiver providing further robustness against antenna array imperfections and multipath. Next, we provide a summary and focus on the main contribution of each

chapter in this thesis.

- **Chapter 2: Preliminaries** provides some theoretical foundations to the content of this thesis. We discuss why information theory is a proper metric in radar and machine learning. In addition, we provide some relevant definitions as **MI**, **neural network (NN)** and **RL**. Furthermore, we discuss the Majorization theory which will be later used for our analysis of spatial correlation and its effects on **MI**. Moreover, we discuss the **DOA** problem and some of the state-of-the-art **DOA** algorithms.
- **Chapter 3: MI based MIMO Radar Beamforming** is divided into two main parts. Part 1 proposes a joint information-theoretic design for transmit and receive radar beamformers for spatially near multiple extended targets. We maximize the **MI** between the received signals and the target signatures, which allows the extraction of the unknown features, which may include shape, dimensions, and material. However, high interference caused by spatially near targets might obstruct the information extraction, and directing the beamformers towards the steering vector as done in conventional beamformers does not solve this problem, especially for extended targets. In this chapter, an iterative algorithm is presented to solve this problem using alternative minimization, dividing it into two blocks. The first block is solving for the transmit beamformers successively using **block coordinate descent (BCD)**, and the second one is solving for the receiver beamformers using **minimum variance distortionless response (MVDR)**. We also show the effect of using our beamformers on the waveform design problem. Numerical results indicate that this algorithm can achieve substantially higher **MI** than the existing conventional methods. Thus, except for some degenerate cases, having fixed beamformers instead of optimized ones lead to significant performance degradation. Part 2 further analyses the effect of spatial correlation **MI** for **MIMO** radars. Unlike the work done in literature for statistical **MIMO** radar, we consider the spatial correlation of the target matrix elements to study the correlated **MIMO** radar performance. There is a trade-off between coherent processing gain in correlated **MIMO** radar and spatial diversity gain of target scatterers in uncorrelated **MIMO** radar. We address how the **MI** between the received signal and target channel matrix is affected by spatial correlation. Using majorization theory and the notion of Schur-convexity, we prove that **MI** has a changing behavior with respect to spatial correlation, where at low **signal-to-noise ratio (SNR)**, the **MI** is Schur-convex, i.e. showing increasing performance as correlation increases. However, this behavior changes at high **SNR**, since **MI** is Schur-concave at high **SNR**, hence it decreases as the spatial correlation increases. Moreover, we investigate the conditions for spatially uncorrelated **MIMO** radar. According to these conditions, as the operating frequency increases with respect to the target location and dimensions, the received paths become more uncorrelated. Hence, the setup with lower operating frequency (more correlated) performs better compared to the higher frequency setup at

low **SNR**. However, at high **SNR**, this behavior is reversed. The content of this chapter is based on the work done in the following papers:

- [J1] A. M. Ahmed, A. A. Ahmad, D. Erni and A. Sezgin, "Maximizing Information Extraction of Extended Radar Targets Through MIMO Beamforming," in *IEEE Geoscience and Remote Sensing Letters*, vol. 16, no. 4, pp. 539-543, April 2019.
- [C2] A. M. Ahmed, A. Sezgin and E. A. Jorswieck, "Impact of Spatial Correlation in MIMO Radar," 2019 53rd Asilomar Conference on Signals, Systems, and Computers, CA, USA, Nov. 2019, pp. 1528-1533.

- **Chapter 4: based Cognitive Beamforming** considers the problem of multi-target detection for **massive multiple input multiple output (MMIMO) cognitive radar (CR)**. The concept of **CR** is based on the perception-action cycle that senses and intelligently adapts to the dynamic environment in order to optimally satisfy a specific mission. However, this usually requires a priori knowledge of the environmental model, which is not available in most cases. We propose a **RL** based algorithm for cognitive multi-target detection in the presence of unknown disturbance statistics. The radar acts as an agent that continuously senses the unknown environment (i.e., targets and disturbance) and consequently optimizes transmitted waveforms in order to maximize the  $P_D$  by focusing the energy in specific range-angle cells (i.e., beamforming).

Furthermore, we propose a solution to the beamforming optimization problem with less complexity than the existing methods. Numerical simulations are performed to assess the performance of the proposed **RL**-based algorithm in both stationary and dynamic environments. The **RL** based beamforming is compared to the conventional omnidirectional approach with equal power allocation and to adaptive beamforming with no **RL**. As highlighted by the proposed numerical results, our **RL**-based beamformer outperforms both approaches in terms of target detection performance. The performance improvement is even particularly remarkable under environmentally harsh conditions such as low **SNR**, heavy-tailed disturbance and rapidly changing scenarios. The content of this chapter is based on the following works:

- [J3] A. M. Ahmed, A. A. Ahmad, S. Fortunati, A. Sezgin, M. S. Greco and F. Gini, "A Reinforcement Learning Based Approach for Multitarget Detection in Massive MIMO Radar," in *IEEE Transactions on Aerospace and Electronic Systems*, vol. 57, no. 5, pp. 2622-2636, Oct. 2021.
- [C3] (**Invited Paper**) A. M. Ahmed, S. Fortunati, A. Sezgin, M. S. Greco and F. Gini, "Robust Reinforcement Learning-based Wald-type Detector for Massive MIMO Radar," *The 29th European Signal Processing Conference (EUSIPCO 2021)*, Dublin, Ireland, August 2021, pp. 846-850.

- **Chapter 5: Deep Learning based DOA Estimation for Small MIMO Antenna Arrays** presents a **multiple-signal classification (MUSIC)**-based **DOA**

estimation strategy using small antenna arrays, via employing deep learning for reconstructing the signals of a *virtual* large antenna array. To achieve the required high angular resolution, radars require large aperture, which impacts the hardware complexity. With the aid of **NN** we overcome this problem. Not only does the proposed strategy deliver significantly better performance than simply plugging the incoming signals into **MUSIC**, but surprisingly, the performance is also better than directly using an actual large antenna array with **MUSIC** for high angle ranges and low test **SNR** values. We further analyze the best choice for the training **SNR** as a function of the test **SNR**, and observe dramatic changes in the behavior of this function for different angle ranges. The work done in this chapter is based on the following paper:

- [J2] A. M. Ahmed, U. S. K. P. M. Thanthrige, A. E. Gamal and A. Sezgin, "Deep Learning for DOA Estimation in MIMO Radar Systems via Emulation of Large Antenna Arrays," in *IEEE Communications Letters*, vol. 25, no. 5, pp. 1559-1563, May 2021.

- **Chapter 6: Deep Learning for DOA Estimation for Coherent Sources using Imperfect Antenna Array** proposes a robust algorithm for **DOA** estimation of coherent sources in presence of antenna array imperfections is presented. We exploit the current advances of deep learning to overcome two of the most common problems facing the state-of-the-art **DOA** algorithms (i.e. coherent sources and array imperfections). We propose a deep **autoencoder (AE)** that is able to correctly resolve coherent sources without the need for spatial smoothing, hence avoiding possible processing overhead and delays. Moreover, we assume the presence of array imperfections in the received signal model such as mutual coupling, gain/ phase mismatches, and position errors. The deep **AE** is trained using the covariance matrix of the received signal, where it alleviates the effect of imperfections, and at the same time act as a filter for the coherent sources. The results show significant improvement compared to the methods used in the literature. The material in this chapter is based on the following paper:

- [C1] A. M. Ahmed, O. Eissa and A. Sezgin, "Deep Autoencoders for DOA Estimation of Coherent Sources using Imperfect Antenna Array," 2020 Third International Workshop on Mobile Terahertz Systems (IWMTS), Essen, Germany, May 2020, pp. 1-5.

Fig. 1.1 summarizes the challenges discussed in the previously mentioned chapters along with the solutions proposed. As this figure suggests, those solutions are stemmed from machine learning and information theory perspectives.

## 1.3 Contributions Outside the Scope of the Thesis

There are other contributions with my students and colleagues that are not included in this thesis as the following:

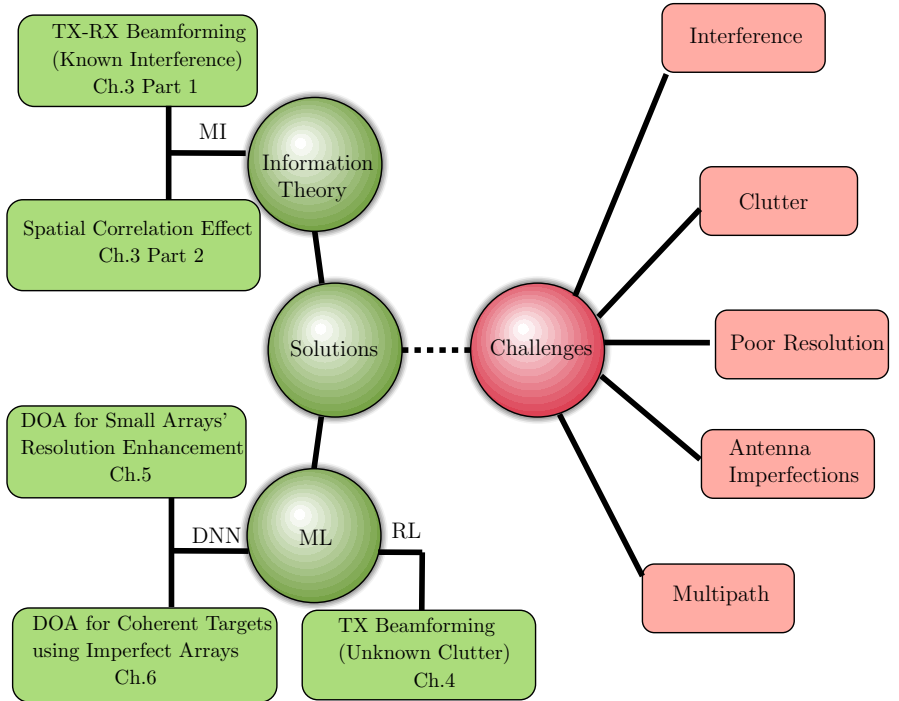


Figure 1.1: Overview of some of the challenges facing the current radar systems and the proposed solutions covered in this thesis from Information Theory and Machine Learning (ML) perspectives.

• **Journal Papers**

- [J4] P. Hillger, P., M. van Delden, U.S.M Thanthrige, A.M. Ahmed et al. "Toward Mobile Integrated Electronic Systems at THz Frequencies," Journal of Infrared, Millimeter, and Terahertz Waves, vol. 41, pp. 846-869, June 2020.

- **Conference Papers**

- [C5] U. S. K. P. M. Thantrige, A. M. Ahmed and A. Sezgin, "Supervised Learning based Super-Resolution DOA Estimation utilizing Antenna Array Extrapolation," 2020 IEEE 91st Vehicular Technology Conference (VTC2020-Spring), Antwerp, Belgium, 2020, pp. 1-5.
- [C4] J. Wittemeier, A. M. Ahmed, T. N. Tran, A. Sezgin and N. Pohl, "3D Localization Using a Scalable FMCW MIMO Radar Design," 2020 German Microwave Conference (GeMiC), Cottbus, Germany, 2020, pp. 100-103.
- [C7] (**Invited Paper**) E. Čišija, A. M. Ahmed, A. Sezgin and H. Wymeersch, "Ris-Aided mmWave MIMO Radar System for Adaptive Multi-Target Localization," 2021 IEEE Statistical Signal Processing Workshop (SSP), Rio de Janeiro, Brazil, 2021, pp. 196-200.





## 2 Preliminaries

This chapter provides an overview of the key theoretical concepts used throughout the thesis. The thesis presents solutions to radar challenges from both information theory and machine learning perspectives, as illustrated in Fig. 1.1. Thus, this chapter explains the fundamental principles of both concepts and how they can be applied to radar systems. The thesis is divided into two main parts. The first part examines solutions from the transmitter's perspective, and the second part explores solutions from the receiver's perspective. Chapters 3 and 4, mainly focus on the waveform design from the transmitter side to aid MIMO radars to overcome traditional limitations like interference and clutter. Therefore, the related concepts are explained in section 2.1. Therein, the concept of waveform diversity and related metrics are introduced. Additionally, section 2.3 provides an introduction to majorization and other related definitions that will be used in the waveform design problem discussed in chapter 3. In section 2.4, the concept of cognitive radar is introduced, which is further discussed in chapter 4. Section 2.5 provides a brief introduction to some machine learning concepts used throughout the thesis, including NN and RL. Lastly, in section 2.6, we address the problem of DOA estimation from the receiver side and investigate the use of machine learning techniques to improve estimation performance. The basic problem of DOA estimation and some state-of-the-art algorithms and their challenges are discussed.

### 2.1 Overview of Waveform design for MIMO Radars

The first part of this thesis (chapters 3 and 4) discusses the waveform design problem for MIMO radars. This section proposes relevant definitions and metrics proposed in these chapters.

#### 2.1.1 MIMO Radars

Generally, MIMO radars can be classified into two types: colocated or widely distributed (statistical) radars. In colocated MIMO radar, the transmitter and receiver are relatively close, such that the radar observes the same target's radar cross section (RCS). This allows significant coherent gain when combining the probing signals, such gain can be achieved through designing the transmit beampattern. In this case, the radar offers better resolution, higher parameter identifiability, and higher sensitivity to detect slow targets [LS07]. This type of radar is explored in our work in the first half of chapter 3 and in chapter 4.

In the latter type, a **MIMO** radar with widely separated antennas captures the spatial diversity of the target's RCS. With the aid of non-coherent processing, the diversity gain for target detection and parameter estimation can be obtained [HBC08]. The statistical radar model is used in our work in the second half of chapter 3.

For both types of radar, the corresponding waveform design problem has been under on-going research, to optimize not only target detection but also identification, revealing its unknown characteristics [FG12]. Characteristics of interest might include shape, dimensions and material. Perhaps one of the first questions to arise is the choice of the design metric to satisfy different radar goals.

In this thesis, we study the problem of waveform design for both radar types to improve radar detection and classification capabilities. The selection of a proper metric is based on the radar operation as further explained in the next subsection.

### 2.1.2 Waveform Design Metrics

**MIMO** radars offer waveform diversity, meaning different antennas can transmit different waveforms, that can be correlated or uncorrelated. Consequently, this diversity offers better utilization of the available degrees of freedom, through designing the transmit waveform. This in turn improves the performance of target detection and parameter estimation, availing as well new operating modes such as classification and identification. The waveform design problem has been under ongoing research, where the transmitted waveform is optimized based on the environment and the radar's different operating modes. To achieve this, several optimization metrics have been proposed in the literature, each tailored to a specific radar operating mode as explained next.

#### Optimal Detection vs Optimal Estimation Waveforms

The related work in this thesis is divided into two main categories. In the first category, we assume that the radar is in detection or search mode in chapter 4, where we propose optimizing the transmit beampattern as a metric to detect unknown deterministic point targets. In more detail, the transmitted waveform is optimized to concentrate the transmitted power towards the angles that most likely contain the targets while minimizing transmitted power in the other angles. This waveform can be described as a detection waveform, where no prior information is assumed about the target locations [Bel93]. Hence, to detect the presence or absence of a certain target, a relevant threshold test can be utilized from detection theory. In more detail, greater energy can be expected in the reflected waveform if a target is present compared to a no-target case.

In the second category, we propose information-theoretic metric (i.e., **MI**) to optimize the transmitted waveform to minimize the mutual signal-dependent interference between multiple stochastic extended targets in chapter 3. An extended target can be characterized as a group of infinite point targets. It can be described with a certain impulse response, while a point target is described with a scalar **RCS** [Che09].

The waveform design problem for an extended target is different from other radar waveform types. These types of waveforms require more information about the target and interference (i.e., their second-order statistics). Hence information theoretic waveform design metrics can be optimal in such cases, where the goal is detecting a particular target of interest. Such waveforms can be beneficial for parameter estimation, identification, and, classification purposes after the targets have been successively detected in the initial probing phase. Those waveforms are called estimation waveforms as explained in [Bel93]. In the next section, we further define these information-theoretic metrics and explain their relevance to radar.

## 2.2 Information Theory and Radar

Information theory has been first applied to radar signal processing in 1953 in [WD53]. The concept of information in radar differs completely from its counterpart in communications. Radar systems mainly seek information about a target, whereas a communication system exploits information regarding a transmitted message. In that sense, Bell in [Bel93] addressed the use of information theory to adaptively design the radar-transmitted waveform. He formulated the waveform design problem to extract more information about the target from the received signal observations. The target was modeled as an extended target, which is defined as a target of a significant physical extent, hence, they do not act as a simple point target that reflects an attenuated scaled version of the transmitted waveform. However, due to their physical extent, they experience significant interference in the reflected signal. For narrow bandwidth waveforms, the point target assumption is often valid, however, as the bandwidth of the transmitted waveform  $B_s$  becomes comparable to  $c\Delta z$ , where  $c$  is the speed of light and  $\Delta z$  is the spatial extent of the target, the point target model will not be accurate. In this case, the reflected signal must be modeled as the reflection of several point in an extended region of space. The designed waveform in that sense is considered optimal to identify or characterize the extended target under investigation. Bell called those waveforms extraction waveforms. A proper metric, in this case, would be **MI**. The next subsection provides more details about **MI** and its definition.

### 2.2.1 Mutual Information

**MI** is an information-theoretic quantity that measures the mutual dependence between two random variables. Specifically, it quantifies the amount of shared information between those variables. In more details, the **MI** denoted as  $I(X;Y)$  between two random variables  $X$  and  $Y$  represents the amount of information provided about  $X$  when observing  $Y$ . Hence, intuitively **MI** is zero if  $X$  and  $Y$  are statistically independent. This in turn means that knowing  $X$  gives no information about  $Y$  and vice versa. However, if both variables are dependent then as the **MI** increases, the uncertainty about variable  $X$  decreases when observing  $Y$ . The formal definition of

$I(X; Y)$  in terms of the joint probability distribution  $P(X, Y)$  of  $X$  and  $Y$  is

$$I(X; Y) = \sum_{x \in \mathcal{X}} \sum_{y \in \mathcal{Y}} P(x, y) \log \frac{P(x, y)}{P(x)P(y)}, \quad (2.1)$$

where  $P(x)$  and  $P(y)$  are the marginal distributions of  $X$  and  $Y$  respectively [Sha48]. **MI** can be also defined in terms of both random variables' entropy (i.e., entropy measures the amount of uncertainty associated with the random variable) such that

$$I(X; Y) = H(X) - H(X|Y), \quad (2.2)$$

where  $H(X)$  is the entropy of  $X$  and  $H(X|Y)$  the conditional entropy (i.e., amount of information needed to describe  $X$  given that  $Y$  is known) [CT06].

Therefore, in the context of radar, **MI** can be used to measure the amount of information that the received signal provides on the target's parameters and characteristics. Thus, if we observe a received signal (i.e.,  $Y$ ) reflected from a target to estimate a certain parameter (i.e.,  $X$ ), then if the waveform is designed to maximize the **MI** between them, the more accurately we can classify this target. In chapter 3, further discussion is provided on the operational meaning of using **MI** in radar and how it can be related to other waveform design metrics.

## 2.3 Majorization Basic Definitions

In this section, we introduce the Majorization theory used in 3.4 and the related definitions.

Majorization is a useful mathematical tool to describe describes a partial order between two vectors  $\mathbf{x}, \mathbf{y} \in \mathbb{R}^n$  [MOA11], it depicts if the components of  $\mathbf{x}$  is less spread out or more nearly equal than the components of  $\mathbf{y}$ .

*Definition 1.* If  $\mathbf{x}$  and  $\mathbf{y}$  have a descending order components, where  $x_1 \geq x_2 \geq x_3 \dots x_n \geq 0$  and  $y_1 \geq y_2 \geq y_3 \dots y_n \geq 0$ , then we say  $\mathbf{x}$  majorizes  $\mathbf{y}$  with notion  $\mathbf{x} \succeq \mathbf{y}$  if [JB07]

$$\sum_{k=1}^m x_k \geq \sum_{k=1}^m y_k, m = 1, \dots, n-1 \quad \text{and} \quad \sum_{k=1}^n x_k = \sum_{k=1}^n y_k. \quad (2.3)$$

The next definition describes the behavior of function  $f$  when applied to vectors  $\mathbf{x}$  and  $\mathbf{y}$ .

*Definition 2.* A function  $f$  defined on  $\mathcal{A} \subset \mathbb{R}^n$  is said to be Schur-convex on  $\mathcal{A}$  if

$$\mathbf{x} \succeq \mathbf{y} \text{ on } \mathcal{A} \implies f(\mathbf{x}) \geq f(\mathbf{y}),$$

and Schur-concave on  $\mathcal{A}$  if

$$\mathbf{x} \succeq \mathbf{y} \text{ on } \mathcal{A} \implies f(\mathbf{x}) \leq f(\mathbf{y}).$$

The next lemma provides a condition to test the Schur convexity of a valued vector function.

*Lemma 1* (Schur-Ostrowski Condition, [JB07, Lemma 2.5]). Let  $\mathcal{I} \subset \mathbb{R}$  be an open interval and let  $f : \mathcal{I}^n \rightarrow \mathbb{R}$  be continuously differentiable.  $f$  is said to be Schur-convex on  $\mathcal{I}^n$  if

$f$  is symmetric <sup>1</sup> on  $\mathcal{I}$ ,

and for all  $\mathbf{a} \in \mathcal{I}^n$

$$(x_i - x_j) \left( \frac{\partial f}{\partial x_i} - \frac{\partial f}{\partial x_j} \right) \geq 0 \quad \forall 1 \leq i, j \leq n, \quad (2.4)$$

and Schur-concave if the inequality in eq. (2.4) is in the opposite direction [JB07].

The symmetry condition in Lemma 1 limits its applicability to only symmetric functions. Hence, there have been several works to deal with this restriction. Hwang in [Hwa79] generalized the Schur condition in Lemma 1 for partially ordered sets. He introduced a corresponding notion for the Schur-Ostrowski condition, where  $\frac{\partial f}{\partial x_i} \geq \frac{\partial f}{\partial x_j}$  for all  $x \in \mathbb{R}^n$  and  $i, j = 1, \dots, n$  where  $j$  dominates  $i$  in the partially order points and the resulting inequalities ( $j > i$ ).

*Theorem 1.* [Hwa79] Let  $f(x_1, \dots, x_n)$  be a function defined over the domain  $\mathcal{D}$ , such that  $\mathbf{x} = [x_1, x_2, \dots, x_n]^T$ . Let  $\mathbf{P} = [p_1, p_2, \dots, p_n]^T$  be a set of points partially ordered by ' $\geq$ ', and  $\mathbf{a} = [a_1, a_2, \dots, a_n]^T$ ,  $\mathbf{b} = [b_1, b_2, \dots, b_n]^T$  be two set of weights where  $a_i$  and  $b_i$  are associated with  $p_i$  for  $i = 1, \dots, n$ , then

$$f(a_1, \dots, a_n) \geq f(b_1, \dots, b_n),$$

for all  $\mathbf{a}$  majorizing  $\mathbf{b}$  on  $\mathbf{P}$  if and only if  $f$  for every  $i$  and  $j$ ,  $p_i \geq p_j$  fulfills

$$\frac{\partial f}{\partial x_i} \geq \frac{\partial f}{\partial x_j} \quad \forall \mathbf{x} \in \mathcal{D}.$$

Simply the Schur convexity of the function demonstrates whether  $f$  is an order-preserving function or not as per Definition 2. This concept is most commonly used in a wireless communication context, specifically in resource allocation problems for multi-user or MIMO systems. Section 3.4 further discusses the application of those functions within the waveform design problem for MIMO radar system.

---

<sup>1</sup>A function is symmetric if the argument vector can be arbitrarily permuted without changing the value of the function

## 2.4 Cognitive Radar (CR)

The waveform diversity offered by MIMO radars as explained in 2.1 has opened new frontiers for adapting the transmitted waveform based on the feedback the radar gets from the environment. This type of cognition employing adaptive Tx and Rx is called *cognitive radar*.

CR paradigm has been first introduced by Haykin taking inspiration from the echolocation of some mammals like bats or dolphins [Hay06], and cognition in human brains [HXS12]. CR is described as a radar system that senses the environment, learns from it, and makes decisions based on what it has learned to accomplish certain assigned tasks through a perception-action cycle of cognition. As a matter of fact, this cycle starts with the illumination of the environment by transmitting a waveform, then from the reflected radar echoes, it learns the dominant information about the target and the surroundings (perception). Finally, it adapts the optimal transmit waveform accordingly to accomplish a desired goal (action) [Hay06]. In a non-stationary environment, this cycle is repeated continuously, where the non-stationarity can be caused by statistical weather variations, stochastic disturbance, or the presence of unknown non-static targets. Whereas, the disturbance in radar is produced by two components, the clutter and white Gaussian noise. In [HXS12], Haykin clearly distinguishes between traditional feed-forward radar, fully adaptive radar, and a CR. A radar is considered adaptive when it employs global feedback including the environment in this feedback loop, where adaptive filtering at the receiver or adaptive beamforming at the transmitter might be applied [Gue10]. However, CR develops its own behavior rules from the experience gained, stores it in the memory, and extends this knowledge to the transmitter. This is followed by a set of smart decision actions. Thus, to choose those actions, CR should benefit from all the available *degrees of freedom (DoF)*, i.e., polarization, time, frequency, code, and beam patterns. Hence, it can be deduced that CRs would benefit significantly from the waveform diversity at the transmitter offered by MIMO radar systems. Consequently, optimization, machine learning, and deep learning can be considered important leveraging technologies for the future evolution of CR [Gin21]. In chapter 4, we investigate a CR MIMO system that perceives the environment and uses machine learning tools to take its decisions intelligently.

## 2.5 Machine Learning (ML) and Radar

In the last few years, machine learning approaches emerged to provide solutions for problems in various research domains such as signal processing, communications, and economics. In particular, the use of machine learning techniques improved the performance of some traditional signal processing approaches overcoming their limitations. Furthermore, machine learning is most useful when there is no model to describe a certain behavior, or when the existing models fail due to assuming the existence of a priori information. In particular, radar can intelligently be adapted,

whether on Tx or Rx side, according to accurate environmental awareness which can be provided by machine learning.

Motivated by those approaches, in this thesis, we revisit some of the classical radar signal processing problems and we provide novel solutions to traditional challenges using machine learning. In the next subsections, we briefly provide an overview of the methods used.

### 2.5.1 ML: Neural Networks (NN)

An artificial NN, a subset of machine learning, is defined as a network of interconnected nodes called neurons, which are used to train a computing system to solve a certain task by simulating the human brain neurons. This network can recognize the patterns within numerical data (i.e., classification). In addition, it can model the relationship between inputs and outputs similar to a mathematical function (i.e., regression) [Sch15]. It is comprised of some node layers: an input layer, one or more hidden layers, and an output layer as in Fig. 2.1. Each hidden layer has a certain number of nodes, each has certain inputs and outputs. Each input  $a_i$  is multiplied by a weight  $w_i$ , then all those weighted inputs are added together with a predefined bias. The resulting sum is passed through a nonlinear activation function  $f$  turning the unbounded input into a bounded one as shown in Fig. 2.2.

It is important to note that the nonlinearity introduced by the activation function

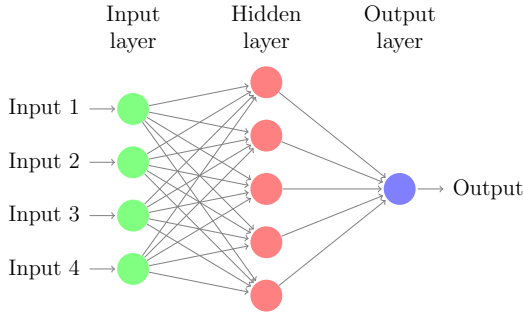


Figure 2.1: Simple Neural Network

is essential to learn the complex functional mapping between the inputs and outputs. Otherwise, the NN would be adding a series of linear weighted combinations. There are several activation functions such as **rectified linear unit (ReLU)**, sigmoid, and Tanh. For instance, in chapter 5 we used the **ReLU** function which is defined as

$$f(x) = \max(0, x). \quad (2.5)$$

In every layer, the nodes are connected to the nodes in other layers in order to send and receive data. In a fully connected NN, each node in every layer is connected to

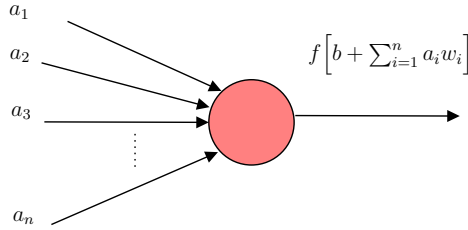


Figure 2.2: Single Neuron

each node in the previous and the next layer.

### Network Training

The training process is performed by successively feeding data through the network, getting output from the **NN**, then comparing the predicted output  $\hat{Y}$  with the actual one  $Y$  using an error function. In this thesis, we used the **mean-squared error (MSE)** which is defined as

$$\text{MSE} = \frac{1}{n} * \sum_{i=1}^n (Y_i - \hat{Y}_i)^2, \quad (2.6)$$

where  $n$  is the number of nodes. The network goal throughout the training is to optimize the weights minimizing this error using backpropagation. The weights are first updated for a single row of data, then this process is repeated for all the available training data set. This entire cycle is called epoch, the network usually takes multiple epochs to train.

### Overfitting vs Underfitting

Typically, increasing the number of hidden layers might be a good idea to enhance the performance. However, this might lead to overfitting (i.e., the network models too well the input training data). Hence, the network won't be able to generalize to different unseen data (i.e., validation or test data).

On contrary, underfitting refers to a network that can not fit certain training data nor be generalized to unseen new data.

Both over and underfitting lead to poor performance. A good fit network is one that can both model the training data and is generalized to other data.

Commonly, the **NN** maps a known labeled input data to a known output under external supervision, which is known as supervised learning. However, if no predefined data is available, then these types of networks will not be of use. Hence, in this case, the computing software must find a solution to the given task on its own. This is done using reinforcement learning algorithms.



## 2.5.2 ML: Reinforcement Learning (RL)

RL is an area of machine learning, where an *agent* learns how to make decisions to achieve a certain goal. This is done by trial and error interactions with the environment [SB18]. Typically an agent performs the course of actions, then it evaluates its goal achievement through two types of information collected from the environment in response to those actions: its current *state* and a *reward*. The reward is defined as a scalar feedback signal, which the agent always seeks to maximize. It is specific to a certain task and a corresponding goal [MRT12]. The interactions with the environment in RL is formally described by Markov decision processes (MDP) [SB18].

*Definition 3.* A Markov decision processes (MDP) is defined by a tuple  $\{\mathcal{S}, \mathcal{A}, \mathcal{P}, r\}$ , where  $\mathcal{S}$  is a finite set of states,  $\mathcal{A}$  is a finite set of actions,  $\mathcal{P}$  is the transition probability from state  $s$  to  $s' \in \mathcal{S}$  after action  $a \in \mathcal{A}$  is performed,  $r$  is the immediate reward evaluated after  $a$  is executed.

A policy  $\pi: \mathcal{S} \rightarrow \mathcal{A}$  is a function that maps a state  $s \in \mathcal{S}$  into an action  $a \in \mathcal{A}$ . Moreover, it defines which action has to be executed at each state. Thus, at time  $k \in [0, K]$ , the agent observes the state  $s_k$ , then based on a specific policy  $\pi$ , it takes action  $a_k = \pi(s_k)$ . Consequently, a new state  $s_{k+1}$  will be reached with probability  $\mathcal{P}(s_{k+1}|s_k, a_k)$  and a reward  $r_{k+1} \in \mathbb{R}$  will be received. The observed information from the environment, the reward  $r_{k+1}$ , and  $s_{k+1}$  are used to improve the policy. This process is repeated till the optimal policy is reached.

To provide a score to a given state, a *state value function*  $\mathcal{V}_\pi: \mathcal{S} \rightarrow \mathbb{R}$  is introduced. This function is defined as the expected cumulative reward received by the agent for starting from state  $s$  and following policy  $\pi$ . More formally, the *state value function* for policy  $\pi$  is defined as

$$\mathcal{V}_\pi(s) = \mathbb{E}_\pi \left[ \sum_{k=0}^{\infty} \gamma^k r_{k+1} | S_k = s \right], \quad (2.7)$$

where  $\mathbb{E}_\pi[\cdot]$  denotes the expected value of a random variable when the agent follows the policy  $\pi$  at any time  $k$ . The scalar  $\gamma \in [0, 1]$  denotes the discount factor which controls the weight given to future rewards. In addition, let us define as *Q-function* the optimal *action value function* for policy  $\pi$ , where  $Q: \mathcal{S} \times \mathcal{A} \rightarrow \mathbb{R}$  is defined as the expected cumulative reward for starting from state  $s$  and taking action  $a$ :

$$Q_\pi(s, a) = \mathbb{E}_\pi \left[ \sum_{k=0}^{\infty} \gamma^k r_{k+1} | s_k = s, a_k = a \right], \quad (2.8)$$

therefore the optimal *state value function* can be written as

$$\mathcal{V}_\pi^*(s) = \arg \max_{a \in \mathcal{A}} Q_\pi(s, a). \quad (2.9)$$

The environment surrounding the agent can be time-variant, and the agent can face new situations. Hence, the RL model must be optimized to be dynamic and navigate through real-time situations. In chapter 4, we address this particular situation, where the agent's task is to track multiple unknown targets in a real-time dynamic environment.

### Exploration vs Exploitation

One challenge in designing RL algorithms is the trade-off between exploration and exploitation. In more detail, the agent must follow the same actions which were tried in the past and proved to maximize the reward. However, the agent is required also to acquire new knowledge through discovering new actions. Hence, the agent remains in a dilemma of whether to exploit the existing experience or explore a new one with the aim of finding better actions. Therefore, the agent must always keep the balance between exploitation and exploration, without favoring one over the other. This can be done using  $\epsilon$  greedy approach, where it selects the action with the highest estimated reward mostly. However, with some probability  $\epsilon$ , it chooses to explore a random action independent from the reward estimates. In chapter 4 we further discuss how this approach is adopted in our system.

## 2.6 Direction of Arrival (DOA)

In the second part of this thesis, discussed in chapters 5 and 6, the problem of DOA estimation is addressed and how the classical approaches can be further improved using concepts from machine learning (ML) previously explained in section 2.5. DOA estimation refers to estimating the direction of several target electromagnetic waves through receive antennas that form a *sensor array*. DOA has a wide range of applications, e.g., radar, sonar, and wireless communications [Tre02]. There are many DOA estimation techniques that can be classified into multiple categories. There are conventional methods that depend on the locations of peaks in the spatial spectrum to determine the DOA, i.e., delay and sum beamforming and MVDR [LWS05]. There are also the subspace methods i.e. which depend on the eigenstructure of the spatial correlation matrix, offering high resolution DOA estimation [TC13]. In addition, there are parametric-based approaches like the maximum likelihood (ML) technique, that use a statistical structure for the process of generating data [Sva99].

### 2.6.1 System Model

Assume that  $L$  targets are impinging on a receive array consisting of  $N$  antennas as in Fig. 2.3, whose DOA is  $\theta_1, \dots, \theta_L$ . Here, we assume the transmit signal is modulated by a carrier frequency  $f_c$ . At the receiver, the radio frequency signals are modulated to the baseband to be further processed. In addition, assume that the signal has a limited bandwidth  $B_s$  with a maximum travel time  $\Delta T$  for a plane wave.

Hence, the narrow band model assumption will be valid if  $B_s \Delta T \ll 1$  [TC13]. The received signal is sampled at  $K_s$  uniquely spaced time instants  $1, \dots, K_s$  to obtain multiple snapshots gathered in matrix  $\mathbf{Z} = [\mathbf{z}(1), \dots, \mathbf{z}(K_s)]$ , with

$$\mathbf{z}(k_s) = \sum_{l=1}^L \mathbf{a}(\theta_k) s_l(k_s) + \tilde{\mathbf{n}}(k_s), \quad \text{for } k_s = 1, \dots, K_s \quad (2.10)$$

$$= \mathbf{A}(\theta) \mathbf{s}(k_s) + \tilde{\mathbf{N}}(k_s). \quad (2.11)$$

$s_l(k_s)$  is the transmit waveform of the  $l$ th source, and  $\tilde{\mathbf{n}}(k_s)$  is the zero-mean Gaussian noise.  $\mathbf{a}(\theta_l)$  denotes the imperfection free steering vector and is defined as

$$\mathbf{a}(\theta_l) = \frac{1}{\sqrt{N}} \left[ 1, e^{-j2\pi \frac{d}{\lambda} \sin \theta_l}, \dots, e^{-j2\pi \frac{d}{\lambda} (N-1) \sin \theta_l} \right]^T, \quad (2.12)$$

while  $\mathbf{A}(\theta) = [\mathbf{a}(\theta_1), \mathbf{a}(\theta_2), \dots, \mathbf{a}(\theta_L)]$  and  $\mathbf{s}(k_s) = [s_1(k_s), s_2(k_s), \dots, s_L(k_s)]$ . The covariance matrix of the received signal  $\mathbf{z}$  is

$$\mathbf{R} = \mathbb{E} [\mathbf{z}(k_s) \mathbf{z}^H(k_s)] \quad (2.13)$$

$$= \mathbf{A}(\theta) \mathbf{R}_s \mathbf{A}^H(\theta) + \mathbf{R}_{\tilde{\mathbf{n}}}, \quad (2.14)$$

where  $\mathbf{R}_s = \mathbb{E} [\mathbf{s}(k_s) \mathbf{s}^H(k_s)]$  and  $\mathbf{R}_{\tilde{\mathbf{n}}} = \mathbb{E} [\tilde{\mathbf{N}}(k_s) \tilde{\mathbf{N}}^H(k_s)]$ . The noise here is assumed to be white Gaussian, i.e.,  $\mathbf{R}_{\tilde{\mathbf{n}}} = \sigma_{\tilde{\mathbf{n}}} \mathbf{I}$ , where  $\sigma_{\tilde{\mathbf{n}}}$  is the noise variance. The estimated covariance matrix from the antenna array observations  $k_s = 1, \dots, K_s$  is

$$\hat{\mathbf{R}} = \frac{1}{K_s} \sum_{k_s=1}^{K_s} \mathbf{z}(k_s) \mathbf{z}^H(k_s). \quad (2.15)$$

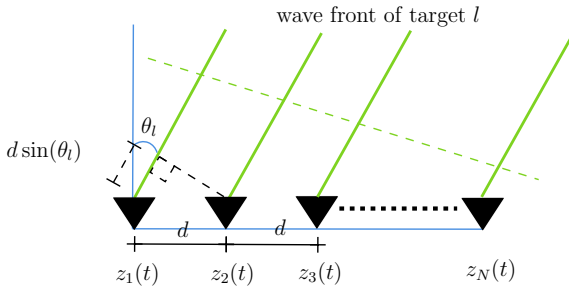


Figure 2.3: DOA

## 2.6.2 Beamforming Methods: Minimum Variance Distortionless Response (MVDR)

Conventional methods such as delay, and sum beamforming view the DOA estimation as a spatial spectrum. The parameters are located within the spectrum, where the power is most concentrated. Hence, it is affected by the resolution limitation due to the finite array aperture. In addition, increasing the SNR or the number of samples will not offer a solution to this problem [Tre02]. The MVDR beamformer formulates the spatial spectrum problem as a constrained optimization problem, overcoming the resolution limitation as

$$\begin{aligned} \min \quad & \mathbf{w}^H \mathbf{R} \mathbf{w} \\ \text{s.t.} \quad & \mathbf{w}^H \mathbf{a}(\theta) = 1 \end{aligned} \quad (2.16)$$

In eq. (2.16), the objective function minimizes the output power from all directions while the beamformer concentrates on the desired direction  $\theta$ . After applying lagrange multipliers, the solution of eq. (2.16) becomes

$$\mathbf{w}_{\text{MVDR}} = \frac{\mathbf{R}^{-1} \mathbf{a}(\theta)}{\mathbf{a}^H(\theta) \mathbf{R}^{-1} \mathbf{a}(\theta)}. \quad (2.17)$$

The MVDR power spectrum is expressed by

$$P_{\text{MVDR}}(\theta) = \frac{1}{\mathbf{a}^H(\theta) \mathbf{R}^{-1} \mathbf{a}(\theta)}. \quad (2.18)$$

The MVDR beamformer's performance depends on the array aperture, SNR, and the number of snapshots. Furthermore, the performance degrades significantly in the presence of coherent or correlated interference. In addition, this kind of beamformer is sensitive to imperfections in the antenna array [Tre02].

## 2.6.3 Subspace Methods: Multiple-Signal Classification (MUSIC)

Subspace methods are known to offer superior performance compared to conventional beamforming. They exploit the eigenstructure of the covariance matrix in eq. (2.13), where the eigenvalue decomposition of  $\mathbf{R}$  is denoted by

$$\mathbf{R} = \mathbf{U}_s \mathbf{\Lambda}_s \mathbf{U}_s^H + \mathbf{U}_{\bar{n}} \mathbf{\Lambda}_{\bar{n}} \mathbf{U}_{\bar{n}}^H, \quad (2.19)$$

where  $\mathbb{E}[\cdot]$  denotes the expected value,  $\mathbf{U}_s$  and  $\mathbf{U}_{\bar{n}}$  are matrices containing the eigenvectors, which represent the signal and noise subspaces, respectively.  $\mathbf{\Lambda}_s = \text{diag}(\lambda_1, \dots, \lambda_L)$  and  $\mathbf{\Lambda}_{\bar{n}} = \text{diag}(\lambda_{L+1}, \dots, \lambda_N)$  contain the corresponding eigenvalues of the target and the noise, respectively. If the signal covariance matrix  $\mathbf{R}_s$  is a full rank matrix, i.e.,  $\text{rank}(\mathbf{R}_s) = L$ , then the matrix  $\mathbf{a}^H(\theta) \mathbf{R}_s \mathbf{a}(\theta)$  would have a rank of  $L$ . In addition, the eigenvalues satisfy the property  $\lambda_1 \geq \lambda_2 \geq \dots, \lambda_L = \lambda_{L+1} \dots = \lambda_N = \sigma_{\bar{n}}$ . In this case, the steering matrix and the signal eigenvectors span the same subspace, which corresponds to the largest  $L$  eigenvalues. Meanwhile,

they are orthogonal to the noise eigenvectors, which corresponds to the remaining  $M - L$  eigenvalues. Exploiting the orthogonality between the noise and steering vector subspaces where

$$\mathbf{a}(\theta) \perp \mathbf{U}_n, \quad (2.20)$$

the expression of the **MUSIC** spectrum which provides the received signal energy distribution for all receive directions is given by

$$P_{MU}(\theta) = \frac{1}{\mathbf{a}^H(\theta) \mathbf{U}_n \mathbf{U}_n^H \mathbf{a}(\theta)}. \quad (2.21)$$

In order to separate the noise and signal subspaces, the number of targets  $L$  is assumed to be known in **MUSIC**. **MUSIC** is known to provide sharp peaks in the desired directions, providing high resolution and improving the estimation accuracy. However, it highly depends on the **SNR**, the number of antennas, and the number of samples. In chapter 5, we prove that **MUSIC** performance can be improved without the dependency on increasing either the **SNR** or the number of antennas. Further limitations occur in multipath scenarios since the rank of  $\mathbf{R}_s$  becomes deficient. This is due to the correlation between the signals arriving at the receiver, hence the orthogonality assumption in eq. (2.20) will not be satisfied. This leads to significant performance degradation for subspace methods as **MUSIC**. Further pre-processing would be required in this case to mitigate the coherence among the signals. and restore the rank of  $\mathbf{R}_s$ . Hence, spatial smoothing techniques can be applied in this case to remove the signal coherence as in [QR11a], however in some cases this is done at the expense of the resolution capability [PK89]. In chapter 6, we present an alternative to **spatial smoothing MUSIC (SS-MUSIC)** using deep learning without the need to compromise resolution.



# 3 Mutual Information (MI) based MIMO Radar Beamforming

This chapter investigates the role of information theory in radar waveform design. We first provide an overview of the main ideas behind the use of information theory in radar waveform design in sections 3.1 and 3.2. Afterward, this chapter is mainly divided into two parts. First, in 3.3, we propose a joint design for the transmit-receive beamformers to maximize the MI in colocated MIMO radars. The colocated MIMO radar system model is presented in 3.3.1, then the optimization problem is formulated and solved in 3.3.2, the simulation results are shown in 3.3.3. second, in 3.4, we further investigate how spatial correlation can affect MI and what are the contributing factors. This is done through utilizing a statistical MIMO radar model in 3.1, where the conditions for spatial de-correlation of a MIMO radar channel are discussed as well. Furthermore, 3.4.3 presents a measure of spatial correlation and revisits the optimum waveform design. Afterwards, the Schur-convexity of the MI function in high and low SNR is examined, then numerical results are provided in section 3.4.4. Finally, 3.5 draws conclusions.

## 3.1 Why MI is a good metric for waveform design ?

MI for waveform design was introduced as a possible metric by Bell [Bel93] in 1993. In his paper, the design of radar waveform was proposed by maximizing the MI between target impulse response and the received signal as previously explained in section 2.2. Bell called such waveforms *information extraction waveforms* or *estimation waveforms*. This is due to the relationship between MI and the lower bound on the parameter estimation error. In his paper, Bell used an extended target model, where the reflected signal is the convolution of the transmitted waveform with the target impulse response, which represents the target's scattering characteristics. He further showed that the optimum waveform design is to distribute the available energy among the various scattering modes of the extended target, which is the same mechanism as the classic water-filling algorithm. In his paper, the target response was modelled as a realization of a Gaussian random process with a known spectral variance. Yang and Blum in [YB07] extended this approach by formulating the same problem using statistical MIMO radars. They provided a comparison between the waveform design from two perspectives. First, minimizing **minimum-mean squared error (MMSE)** in estimating the target impulse response, and second, maximizing the MI between the impulse response and the received signal. It was shown that if the

transmitter has knowledge of the target's second-order statistics, both optimization problems yield the same waveform design. Those findings depict that superior **MI** improves the target parameter estimation. Furthermore, in [RBG11] the authors provided a comprehensive comparison between **SNR**-based and **MI**-based waveforms. Therein, the authors showed that both waveforms have different transmit spectra, where the **SNR**-based waveform concentrate most of the transmitted energy towards one dominant frequency band. However, the **MI**-based waveform tend to spread its energy across a few dominant frequency bands. This is due to the logarithmic relationship between both metrics. Generally the **MI** spectral density at frequency  $f$  is given by  $\text{MI}(f) = \ln(1 + \text{SNR}(f))$ , where  $\text{SNR}(f)$  is the **SNR** spectral density at frequency  $f$ . Hence, via Taylor series approximation, the **MI** spectral density is nearly equivalent to the **SNR** spectral density for frequency components with small coefficients. However, the **MI** spectral density is nearly equivalent to the logarithm of the **SNR** spectral density for frequencies with large components. Consequently, the values of those large components are lowered through the logarithm function. This in turn enables less dominant frequency components in the **MI** spectral density to be rather significant. Hence, those components are allocated energy when **MI** waveforms are optimized through the water-filling algorithm. Intuitively, this explains why **MI**-based waveforms are most suitable for estimation and classification purposes since it conveys information from the less dominant frequency components in the target response. Those findings further justify the operational use of using **MI** as a metric in the radar waveform design problem. In the next section, we will discuss the relevant state-of-the-art and the contribution of this chapter.

## 3.2 Related Work

The work in [YB07] modeled the channel similar to the point-to-point **MIMO** channel model in communications, where all the targets are included in one spatio-temporal channel matrix. Hence, the optimal solution leads to water-filling over the eigenmodes of this matrix. However, this might always lead to allocating low power to targets observed through weak modes of the channel matrix. Hence for multiple targets, such an approach might not be desirable.

Leshem et. al in [LNN07] tackled this problem, where they reformulated the system model to include the effect of each target in the presence of another target as interference. The optimization problem is cast similar to sum-rate maximization. However, this complicated the optimization problem as it became highly nonlinear in all the variables. Therefore, the authors in [LNN07] fixed the transmit beamformers to conventional beamformers to relax the problem, where the beamforming vectors are chosen to be in the direction of the steering vector. This transformed the optimization problem into a power allocation over multiple targets.

Though using conventional beamformers offers a high gain in the target direction, that does not apply in an environment where interference exists from other sources [LLH14a]. The challenge in such environments is to modify the transmit and



receive beamformers jointly to match the target and null interference. Liu et. al. in [LLH14b] addressed this problem from a **signal-to-interference-and-noise ratio (SINR)** perspective, where they proposed an iterative optimization algorithm to solve for the transmit and receive beamforming vector for only point targets. However, since extended targets have many scattering centers, they overlap over the frequency spectrum. Therefore, in some frequency bins, the total **SINR** might be high because of dominating targets with higher reflection centers, therefore, the information retrieved about weak targets can be lost. To the best of our knowledge, no one tackled this problem from **MI** perspective due to its complexity, since the optimization variables for each target now become vectors scaled with the number of antennas.

In the first part of this chapter, we jointly design information-theoretic transmit and receive radar beamformers for spatially near multiple extended targets with colocated radar. We propose an optimization algorithm to solve this problem utilizing the concept of alternating minimization. Interestingly for two extended near targets with the overlapping spectrum, the waveform is well separated across the frequency range, unlike the case for conventional beamformers.

In the second part of this chapter, we further extend our investigations to include statistical **MIMO** radar. In addition to the advantages shown of using **MI** to design radar waveform for colocated **MIMO**, several works in the literature investigated the same information theoretic approach for statistical **MIMO** radar. For instance, the authors in [TTP10] addressed statistical **MIMO** radar waveform design based on **MI** in the presence of colored noise. They show that the optimum waveform in this case should match the target and noise eigendirections. However, in [TTP10] they ignored the effect of spatial correlation and assumed the channel matrix to be independent and identically distributed.

In general, there is a trade-off between coherent processing gain in correlated **MIMO** radar and spatial diversity gain of target scatterers in uncorrelated **MIMO** radar. The authors in [HBC08] show that by utilizing spatial diversity in statistical **MIMO** radars, it can overcome bandwidth limitations and offer high-resolution target localization. In addition, they derive conditions for spatial de-correlation of the reflected paths to achieve diversity gain. Those conditions are influenced by the antenna spacing, operating frequency, and the target location and dimensions. In this chapter, we induce spatial correlation to the target matrix elements by violating those conditions, in order to study the effect of correlation on the performance of statistical **MIMO** radar waveform design based on **MI**. In more detail, we investigate how the **MI** between the received signal and target channel matrix is affected by spatial correlation in the presence of colored noise.

The contribution of this chapter is:

1. We jointly optimize the transmit and receive beamformers to maximize the **MI** between the target signatures and the received signal for colocated **MIMO** radar. The optimization problem becomes nontractable as the objective function is non-convex in terms of the two variables. We examine herein this problem, by utilizing the concept of alternating minimization, where we fix one variable

and solve for the other, and vice versa. If we solve only for the receiver beamformers and fix the transmit ones, the problem becomes similar to minimizing the interference on each target, which is similar to the **MVDR** beamformers. However, if we fix the receiver beamformers and optimize the transmit ones jointly for all the targets, the problem will still be non-convex. Here, we use the **BCD** methodology, which divides the problem into multiple blocks and successively solves it with respect to each block. we show the effect of our algorithm on the **MI** performance.

2. We apply the resulting beamformers to the waveform design problem as described in [LNN07]. Interestingly for two extended near targets with the overlapping spectrum, the waveform is separated across the frequency range, unlike the case for conventional beamformers. In addition, using the generated waveforms along with the optimized beamformers shows significant enhancement in the **MI** performance especially at higher transmit powers.
3. We investigate the effect of spatial correlation in statistical **MIMO** radar from **MI** perspective. Using majorization theory and the notion of Schur-convexity, we prove that **MI** has a changing behavior with respect to spatial correlation, where at low **SNR**, the **MI** is Schur-convex, i.e. showing increasing performance as correlation increases. However, this behavior changes at high **SNR**, since **MI** is Schur-concave at high **SNR**, hence it decreases as the spatial correlation increases. Moreover, we investigate the conditions for spatially uncorrelated **MIMO** radar. According to these conditions, as the operating frequency increases with respect to the target location and dimensions, the received paths become more uncorrelated. Hence, the setup with a lower operating frequency (more correlated) performs better compared to the higher frequency setup at low **SNR**. However, at high **SNR**, this behavior is reversed.

### 3.3 Transmit - Receive Beamforming

We consider a collocated **MIMO** radar that uses transmit and receive beamforming. It consists of an **uniform linear array (ULA)** with  $M$  transmit and  $N$  receive elements. Assume that those elements transmit  $K$  waveforms simultaneously to detect  $L$  targets each at  $\theta_l$ . In this model, the transmit and receive beamforming vectors are designed jointly to detect spatially near multiple extended targets. Those targets are characterized by multiple scattering centers and large areas compared to the resolution cell. Thus, one target can extend the bounds of a single range cell. We assume that the radar bandwidth is sufficiently large to resolve the target's scatterers. Hence, the target impulse response is modeled as a collection of idealized

nondispersive point targets as

$$\psi_l(t) = \sum_{r=1}^Q \alpha_{l,q} \delta(t - \tau_r) \quad (3.1)$$

where  $Q$  is the number of scatterers and  $\alpha_{l,q}$  is the complex amplitude of each reflection center with a corresponding delay of  $\tau_r$ . A stochastic target model is assumed in this section, whose **power spectral density (PSD)** is in turn a stochastic process. This process modeled as a Gaussian random variable whose second-order statistics are known [Bel93]. The Fourier transform of  $\psi_l(t)$  can be expressed as

$$h_l(f_d) = \int_0^{\tau_{h_l}} \psi(\tau) e^{-j2\pi f\tau} d\tau, \quad (3.2)$$

where  $h_l(f_d)$  is the target frequency response which is considered to be equally spaced sampled such that  $f_d \in \mathcal{W} \triangleq \{f_1, f_1 + \Delta_f, \dots, f_D\}$ , where  $\Delta_f$  is the spacing between frequency samples. In addition,  $\tau_{h_l}$  is the finite duration of  $\psi_l(t)$ . Thus, assuming a zero mean Gaussian process, the spectral variance of  $h_l(f_d)$  can be defined as

$$\sigma_{h_l}^2(f_d) = \mathbb{E} [|h_l(f_d)|^2] \quad (3.3)$$

Throughout this chapter, we assume the target spectral variance is known, this can be gathered through measurements or using a feedback system, such as **CR** (for more details about **CR**, please refer to 2.4). Furthermore, we assume that the radar has prior estimate about their locations [LNN07]. Those assumptions can be justified if the radar is in tracking or classification mode, this means that the targets have been already detected in the search mode as previously explained in 2.1. In those applications, the waveform is adaptively modified in each transmission to recognize a known target in a closed loop radar or **CR** framework. As a result, the radar in this case can classify the target after gaining a thorough understanding of the channel [GVN07]. In this chapter, we only focus on the design of the waveform. In the upcoming chapters, we will discuss in detail how to detect targets and estimate their corresponding location in the search mode.

### 3.3.1 Colocated MIMO Radar System Model

The radar transmits simultaneous beams, where each beam is dedicated to each target to detect it in the presence of others as interference (i.e.,  $K = L$ ). In more detail, the radar focuses the energy of  $L$  transmitted orthogonal waveforms towards the spatial directions of those targets using transmit beamformers. The transmitted wideband signal in the frequency domain at  $f_d$  is given by<sup>1</sup>

$$\mathbf{S}(f_d) = \sum_{l=1}^L \mathbf{v}_l(f_d) s_l(f_d), \quad (3.4)$$

<sup>1</sup>A wide band signal is assumed here to capture the details of the extended targets' response, since the radar is assumed to be in classification mode.

where  $s_l(f_d)$  is the transmitted waveform normalized to unit energy, directed towards target  $l$  using transmitting beamforming vector  $\mathbf{v}_l(f_d) \in \mathbb{C}^{M \times 1}$  at frequency  $f_d$ , where  $l \in \mathcal{L} \triangleq \{1, \dots, L\}$ . A total power constraint is assumed such that  $P_{\max} = \sum_{l=1}^L P_l$ , where  $P_l$  is the transmit power dedicated for target  $l$  across all frequencies such that  $P_l = \sum_{f_d=f_1}^{f_D} \|\mathbf{v}_l(f_d)\|^2$ . It is assumed that target waveforms  $\mathbf{s}_l$ , where  $\mathbf{s}_l = [s_l(f_1), \dots, s_l(f_D)]$ , are orthogonal to each other. The received signal at target  $l$  would be given by<sup>2</sup>

$$x_l(f_d) = \mathbf{a}^T(\theta_l, f_d) \mathbf{v}_l(f_d) h_l(f_d) s_l(f_d) + \sum_{i \neq l}^L \mathbf{a}^T(\theta_i, f_d) \mathbf{v}_i(f_d) h_i(f_d) s_i(f_d), \quad (3.5)$$

where  $\mathbf{a}^T(\theta_l, f_d)$  is the steering vector of the target  $l$ , which is a result of the propagation phase delay between the transmit antennas as

$$\mathbf{a}(\theta_l, f_d) = [1, e^{-jr \sin(\theta_l)}, \dots, e^{-jr(M-1) \sin(\theta_l)}]^T \quad (3.6)$$

where  $r = \frac{2\pi d}{\lambda}$ . Here channel reciprocity is assumed, and if the receive steering vector is  $\mathbf{a}(\theta_l, f_d)$ , then the transmit one is  $\mathbf{a}^T(\theta_l, f_d)$ . At the receiver array, the received signal for target  $l$  becomes

$$\mathbf{y}_l(f_d) = \mathbf{a}(\theta_l, f_d) x_l(f_d) + \tilde{\mathbf{n}}(f_d), \quad (3.7)$$

where  $\tilde{\mathbf{n}}(f_d)$  a white Gaussian noise vector with zero mean and variance  $\sigma_n^2$ . Afterward, the signal received is processed by a bank of matched filters matched to each waveform. So the output would be

$$\mathbf{y}(f_d) = \sum_{l=1}^L \mathbf{a}(\theta_l, f_d) \mathbf{x}_l(f_d) s_l^*(f_d) + \sum_{l=1}^L \tilde{\mathbf{n}}(f_d) s_l^*(f_d), \quad (3.8)$$

where  $s_l^*(f_d)$  is the matched filter response of target  $l$  at frequency  $f_d$  such that  $|s_l(f_d)|^2 = 1$ . Moreover, the noise and the matched filter are statistically independent, hence the variance of the noise will remain  $\sigma_n^2$ . Eventually, the received signal  $\mathbf{y}(f_d)$  is processed by  $N$  receiving antenna array whose beamforming vector is given by  $\mathbf{w}_l(f_d)$  to produce scalar signal  $z(f_d) = \mathbf{w}_l^H(f_d) \mathbf{y}(f_d)$ . The signal  $z(f_d)$  can be rewritten as the sum of desired signal for  $l_{th}$  target and interference as following

$$z(f_d) = z_l(f_d) + z_i(f_d), \quad i \neq l, \quad (3.9)$$

where the desired signal component is defined as

$$z_l(f_d) = \mathbf{w}_l^H(f_d) \mathbf{A}(\theta_l, f_d) \mathbf{v}_l(f_d) h_l(f_d),$$

---

<sup>2</sup>It is worth noting that we assume the radar observes a certain orientation of the extended target, if this changes then  $h_l(f_d)$  and  $\sigma_n^2(f_d)$  will change accordingly.

with rank one matrix  $\mathbf{A}(\theta_l, f_d) = \mathbf{a}(\theta_l, f_d) \mathbf{a}^T(\theta_l, f_d)$ . Further, the interference and noise signal for target  $l$  is defined as

$$z_l(f_d) = \mathbf{w}_l^H(f_d) \sum_{j \neq l}^L \mathbf{A}(\theta_j, f_d) \mathbf{v}_j(f_d) h_l(f_d) + \mathbf{w}_l^H(f_d) \bar{\mathbf{n}}(f_d).$$

In section 2.2, the MI between two random variables was explained and the corresponding definitions were given. In this work, as a metric for the waveform design, we use the conditional MI of the received signal and the target impulse response, given that the transmitted signal is known, which is denoted by  $I(h_l(f_d), z(f_d)|s_l(f_d))$ . This is due to the fact that conditional MI takes into account the knowledge of  $s_l(f_d)$  at the receiver unlike  $I(h_l(f_d), z(f_d))$ , which only maximizes the mutual information between the received signal and the target response, regardless of the signal used. Thus, using only  $I(h_l(f_d), z(f_d))$  might lead that the resulting waveform might not be optimal given the design constraints of the transmitted signal. Therefore, for a certain  $f_d$ , the conditional MI<sup>3</sup> can be written in terms of the differential entropy as

$$I(h_l, z|s_l) = H(z|s_l) - H(z|h_l, s_l). \quad (3.10)$$

Since the target responses are modeled as Gaussian distributed random variables, then the MI between target  $l$  and the received signal  $z(f_d)$ , given that  $s_l(f_d)$  is transmitted, is

$$I(h_l(f_d), z(f_d)|s_l(f_d)) = \Delta_f \log \left( 1 + \frac{|\mathbf{u}_{l,l}(f_d) \mathbf{v}_l(f_d)|^2 \sigma_{h_l}^2(f_d)}{\left| \sum_{j \neq l}^L \mathbf{u}_{l,j}(f_d) \mathbf{v}_j(f_d) \right|^2 \sigma_{h_j}^2 + |\mathbf{w}_l^H(f_d)|^2 \sigma_{\bar{n}}^2} \right), \quad (3.11)$$

where  $\mathbf{u}_{l,j}(f_d) = \mathbf{w}_l^H(f_d) \mathbf{A}(\theta_j, f_d)$ . It is worth noting the second term in the logarithm in eq. (3.11) denotes the  $\mathbb{E}(\text{SINR}_l) = \mathbb{E}(|z_l(f_d)|^2 / |z_i(f_d)|^2)$ , where  $\text{SINR}_l$  is the signal-to-interference-plus-noise ratio for target  $l$ . We refer the reader to [Bel88] for detailed derivation of eq. (3.11).

The total MI across all frequencies between the received signal and target  $l$  can be depicted as

$$\mathbf{I}(\mathbf{h}_l; \mathbf{z} | \mathbf{s}_l) = \sum_{f_d=f_1}^{f_D} I(h_l(f_d), z(f_d)|s_l(f_d)), \quad (3.12)$$

where  $\mathbf{h}_l = [h_l(f_1), \dots, h_l(f_D)]$ ,  $\mathbf{z} = [z(f_1), \dots, z(f_D)]$ , and  $\mathbf{s}_l = [s_l(f_1), \dots, s_l(f_D)]$ .

Next, we will formulate a joint optimization problem to design not only the transmitted waveform spectrum but also the transmit and receive beamformers. The main

<sup>3</sup>for simplicity, we will refer to the conditional MI as MI for the rest of the chapter.

objective function  $\mathcal{P}_0$  can now be written as

$$\begin{aligned} \mathcal{P}_0 : \quad & \max_{\mathcal{V}} \sum_{l=1}^L \mathbf{I}(\mathbf{h}_l; \mathbf{z} | \mathbf{s}_l) \\ \text{s.t.} \quad & \sum_{l=1}^L \sum_{f_d=f_1}^{f_D} \|\mathbf{v}_l(f_d)\|^2 < P_{\max}, \end{aligned} \quad (3.13)$$

where  $\mathcal{V}$  is the set of optimization variables such that  $\mathcal{V} \triangleq \{\mathbf{v}_l, \mathbf{w}_l | \forall f_d \in \mathcal{W}, \forall l \in \mathcal{L}\}$ . For simplicity, we refer to  $\mathbf{v}_l(f_d)$  and  $\mathbf{w}_l(f_d)$  as  $\mathbf{v}_l$  and  $\mathbf{w}_l$  respectively. Here, we consider  $\|\cdot\|^2$  as the Frobenius norm.

### 3.3.2 Optimization Problem

In this section, the objective function given in eq. (3.13) is further discussed. First, note that solving such a problem is very challenging as the beamforming vectors and transmitted powers need to be jointly optimized across different frequencies for each target. This is since the problem is non-convex due to the fractional term in the log function. In contrast, minimizing with respect to one variable and keeping the other fixed is relatively easier [NSW09]. This concept is utilized here, where the main problem is solved iteratively, rather than through a joint optimization over the beamformers and powers. To this end, the problem defined in eq. (3.13) is divided into three problems (i.e.,  $\mathcal{P}_1$ ,  $\mathcal{P}_2$  and  $\mathcal{P}_3$ ) solved alternatively. Our approach is to initially optimize the power spectrum in  $\mathcal{P}_1$ , while fixing the beamformers, then in  $\mathcal{P}_2$  and  $\mathcal{P}_3$ , solve for the receive and transmit beamformers respectively while fixing the power spectrum till convergence. Initially, the problem in eq. (3.13) is solved for the power spectrum assuming that the beamformers  $\mathbf{v}_l$  and  $\mathbf{w}_l$  are fixed  $\forall l$  as follows

$$\begin{aligned} \mathcal{P}_1 : \quad & \max_{P_l(f_d)} \sum_{l=1}^L \sum_{f_d=f_1}^{f_D} I(h_l(f_d), z(f_d) | s_l(f_d)) \\ \text{s.t.} \quad & \sum_{l=1}^L \sum_{f_d=f_1}^{f_D} P_l(f_d) \leq P_{\max}, \quad \forall l \in \mathcal{L}, \forall f_d \in \mathcal{W}, \end{aligned} \quad (3.14)$$

such that  $P_l(f_d) = \|\mathbf{v}_l\|^2$ . Since the beamformers are fixed,  $\mathcal{P}_1$  can be considered as a power spectrum allocation problem for each target under a total power constraint  $P_{\max}$ . This problem can be solved using the Lagrangian method, where the multipliers are solved using bisection as in [LNN07]. The next step is to solve for the beamformers using the output  $P_l(f_d)$  from eq. (3.14)  $\forall f_d$  and  $\forall l$  as discussed in the following.

#### Alternating Minimization of $\mathbf{v}_l$ and $\mathbf{w}_l$

It is noticed that the objective function  $\mathcal{P}_1$  and its constraint consist of a large number of individual functions, that corresponds to  $f_D$  frequency bins. The proposed

approach to this problem is to solve for each frequency bin using the power  $P_l(f_d)$  from eq. (3.14), specified to each frequency  $f_d$ . So eq. (3.13) can be reformulated as

$$\begin{aligned} \min_{\mathbf{v}_l, \mathbf{w}_l} \quad & - \sum_{l=1}^L I(h_l(f_d), z(f_d) | s_l(f_d)) \\ \text{s.t.} \quad & \|\mathbf{v}_l\|^2 \leq P_l(f_d), \quad \forall l \in \mathcal{L}. \end{aligned} \quad (3.15)$$

However, the problem is still non-convex in terms of two vector variables. Hence, the concept of alternating minimization is utilized here, where eq. (3.15) is solved through alternating between both variables, i.e., optimizing  $\mathbf{v}_l$  for a fixed  $\mathbf{w}_l$  and vice versa at each frequency  $f_d$ .

### Receive Beamforming

The algorithm starts by fixing the transmit beamformers and solves for the receive ones. If  $\mathbb{E}(|z_i(f_d)|^2) = \mathbb{E}(z_i(f_d)z_i(f_d)^H)$ , then we can mathematically re-arrange eq. (3.11) as

$$I(h_l(f_d), z(f_d) | s_l(f_d)) = \Delta_f \log \left( 1 + \frac{|\mathbf{u}_{l,l} \mathbf{v}_l|^2 \sigma_{h_l}^2}{\sum_{j \neq l} \mathbf{w}_l^H \mathbf{A}(\theta_j) \mathbf{v}_j \mathbf{v}_j^H \mathbf{A}^H(\theta_j) \mathbf{w}_l \sigma_{h_j}^2 + \sigma_n^2 \mathbf{w}_l^H \mathbf{w}_l} \right), \quad (3.16)$$

where for simplicity, we refer to  $\mathbf{u}_{l,l}(f_d)$ ,  $\mathbf{A}(\theta_j)(f_d)$ ,  $\sigma_{h_l}^2(f_d)$  as  $\mathbf{u}_{l,l}$ ,  $\mathbf{A}(\theta_j)$ , and  $\sigma_{h_l}^2$  respectively. Furthermore, define the interference plus noise covariance matrix

$$\mathbf{R}_{i+n} = \sum_{j \neq l} \mathbf{A}(\theta_j) \mathbf{v}_j \mathbf{v}_j^H \mathbf{A}^H(\theta_j) \sigma_{h_j}^2 + \sigma_n^2 \quad (3.17)$$

Thus, then for fixed  $\mathbf{v}_l$  and  $P_l(f_d)$ , the problem in eq. (3.13) can be re-casted as

$$\mathcal{P}_2 : \min_{\mathbf{w}_l} - \sum_{l=1}^L \log \left( 1 + \frac{|\mathbf{w}_l^H \mathbf{A}(\theta_l, f_d) \mathbf{v}_l|^2 \sigma_{h_l}^2(f_d)}{\mathbf{w}_l^H \mathbf{R}_{i+n} \mathbf{w}_l} \right), \quad (3.18)$$

As the optimization here is over the logarithmic sum with independent variables, each term in the summation can be solved independently. In fact, to minimize the interference caused by other targets, one can use the standard **MVDR** previously explained in subsection 2.6.2 where the receive beamformers for target  $l$  would be given as [LWS05]

$$\mathbf{w}_l = \frac{\mathbf{R}_{i+n}^{-1} \mathbf{a}(\theta_l)}{\mathbf{a}^H(\theta_l) \mathbf{R}_{i+n}^{-1} \mathbf{a}(\theta_l)}. \quad (3.19)$$

### Transmit Beamforming

After solving for the receive beamformers, the algorithm would now solve for the optimal  $\mathbf{v}_l$  by solving the following problem

$$\begin{aligned} \mathcal{P}_3 : \min_{\mathbf{v}_l} & - \sum_{l=1}^L I(h_l(f_d), z(f_d) | s_l(f_d)) \\ \text{s.t.} & \|\mathbf{v}_l\|^2 \leq P_l(f_d), \quad \forall l \in \mathcal{L}. \end{aligned} \quad (3.20)$$

The optimization problem  $\mathcal{P}_3$  is still non-convex and NP-hard [LDL11], since we still need to jointly optimize over  $\mathbf{v}_l$  and  $\mathbf{v}_j$  in eq. (3.11) inside the fraction term. Eq. (3.20) is rewritten as

$$\begin{aligned} \mathcal{P}_3 : \min_{\mathbf{v}_l} & \mathcal{F}(\mathbf{v}_1, \mathbf{v}_2, \dots, \mathbf{v}_L) \\ \text{s.t.} & \|\mathbf{v}_l\|^2 \leq P_l(f_d), \quad \forall l \in \mathcal{L}. \end{aligned} \quad (3.21)$$

Due to the separability of the constraints of eq. (3.21), and assuming that  $\mathcal{F}$  is twice differentiable, then this problem can be efficiently solved using coordinate descent algorithms obtaining the **Karush-Kuhn-Tucker (KKT)** solution of  $\mathcal{P}_3$ , specifically using **BCD** [WZY+18, LDL11]. The algorithm solves eq. (3.21) cyclically by optimizing one block at a time, i.e.,  $\mathbf{v}_k$ , while fixing all other blocks of variables (i.e.,  $\mathbf{v}_{j \neq k}$ ). The algorithm first initializes all beamformers randomly such that  $\mathbf{v}^1 = [\mathbf{v}_1, \mathbf{v}_2, \dots, \mathbf{v}_L]$ . Afterward, the following update rule at iteration  $i + 1$  is accomplished

$$\mathbf{v}_l^{i+1} = \min_{\mathbf{v}_l} \mathcal{F}(\mathbf{v}_1^{i+1}, \mathbf{v}_2^{i+1}, \dots, \mathbf{v}_{l-1}^{i+1}, \mathbf{v}_l, \mathbf{v}_{l+1}^i, \dots, \mathbf{v}_L^i) \quad (3.22)$$

This procedure is applied till the objective function is not decreasing anymore at each coordinate direction. For further proof of the convergence, the reader is recommended to refer to [Ber08]. **BCD** is most useful in solving large-scale optimization problems, hence such an algorithm is suitable for our problem if there are large numbers of extended targets present and consequently a large number of transmit beamformers. Under the power constraint:  $\|\mathbf{v}_l\|^2 \leq P_l(f_d)$ , the proposed algorithm would try to allocate  $\mathbf{v}_l$  that would increase the information known about all targets, then use this beamformer to solve for others, till it reaches an iteration stage where all transmit beamformers are optimal for all the targets, and the mutual information is not increasing anymore. Algorithm 1 describes how to utilize **BCD** to solve for radar transmit beamformers. The variable  $\nabla_{\mathbf{v}_l} \mathcal{F}(\gamma_l)$  in eq. (3.23) denotes the gradient of the function defined in eq. (3.15). If the fractional term in the **MI** expression in (3.11) is redefined as  $\text{SINR}_l = \tilde{P}_l / \tilde{I}_l$ , then the gradient can be written



---

**Algorithm 1** Transmit Beamforming
 

---

**Input**  $\mathbf{v}^1$ ,  $\mathbf{a}(\theta_l, f_d)$ ,  $\sigma_{h_l}^2(f_d)$ ,  $\sigma_h^2$ ,  $\mathbf{w}_l(f_d)$ ,  $P_l(f_d) \forall l = 1, \dots, L$ .

**Output** optimal  $\mathbf{v}_l^*$  at  $f_d$

**Initialization**  $i = 1$

**repeat**

$$\gamma_1^{i+1} = \mathbf{v}^1$$

**for**  $l = 1, 2, \dots, L$  **do**

$$\gamma_l^{i+1} = [\mathbf{v}_1^{i+1}, \mathbf{v}_2^{i+1}, \dots, \mathbf{v}_{l-1}^{i+1}, \mathbf{v}_l, \mathbf{v}_{l+1}^i, \dots, \mathbf{v}_L^i]$$

$$\mathbf{d}_l^{i+1} = P_{V_l}(\mathbf{v}_l^i - \nabla_{\mathbf{v}_l} \mathcal{F}(\gamma_l^{i+1})) \quad (3.23)$$

▷  $\mathbf{d}_l^{i+1}$  is the gradient projection direction for  $\mathbf{v}_l$

$$P_{V_l} = \begin{cases} \mathbf{v}_l, & \|\mathbf{v}_l\| \leq \sqrt{P_l(f_d)} \\ \frac{\sqrt{P_l(f_d)} \mathbf{v}_l}{\|\mathbf{v}_l\|}, & \|\mathbf{v}_l\| > \sqrt{P_l(f_d)} \end{cases} \quad (3.24)$$

▷  $P_{V_l}[\cdot]$  is the orthogonal projection to  $V_l$

$$\mathbf{v}_l^{i+1} = \mathbf{v}_l^i + \xi_l^{i+1} \mathbf{d}_l^{i+1} \quad (3.25)$$

**end for**

$$i = i + 1$$

**until**  $\|\mathbf{v}^{i+1} - \mathbf{v}^i\| > \varepsilon$

---

as  $\nabla_{\mathbf{v}_l} \mathcal{F}(\mathbf{v}_1, \mathbf{v}_2, \dots, \mathbf{v}_L) = -\sum_{j=1}^L \mathbf{D}_l(j)$ , and

$$\mathbf{D}_l(j) = \begin{cases} \frac{2\sigma_{h_l}^2 \mathbf{u}_{l,l}^H \mathbf{v}_l \mathbf{u}_{l,l}}{\tilde{I}_l (1 + \text{SINR}_l)}, & j = l \\ -2\sigma_{h_j}^2 \tilde{P}_j \mathbf{u}_{j,l}^H \mathbf{v}_l \mathbf{u}_{j,l} / \tilde{I}_j^2 (1 + \text{SINR}_l)^2, & j \neq l. \end{cases}$$

Algorithm 1 applies projected gradient descent [LDL11], where the function moves in the direction of the negative gradient in each coordinate, afterwards it is projected onto the feasible set. Hence, eq. (3.23) finds the search direction  $\mathbf{d}_l$  of the gradient to solve for eq. (3.21). Furthermore, eq. (3.24) ensures the satisfaction of the power budget through projection onto a ball constraint  $V_l = \{\mathbf{v}_l \mid \|\mathbf{v}_l\| \leq \sqrt{P_l(f_d)}\}$ .

### Amrijo Rule

In this algorithm, the step size  $\xi_l$  in the gradient direction introduced in eq. (3.25) is very important. A small step size would lead to a huge number of iterations, and a large step size could make the algorithm unstable. So, backtracking- Amrijo line

search is used to find the optimal step size [Ber08], where  $\xi_l^{i+1} > 0$  is the smallest step size satisfying :

$$\mathcal{F}(\mathbf{v}_l^i + \xi_l^{i+1} \mathbf{d}_l^{i+1}) \leq \mathcal{F}(\mathbf{v}_l^i) + \xi_l^{i+1} \beta \nabla_{\mathbf{v}_l} \mathcal{F}(\gamma_l^{i+1})^T \mathbf{d}_l^{i+1}.$$

The constant  $\beta$  is chosen to be 0.1. Afterward, using the output transmit beamformers from algorithm 1, the overall iterative algorithm 2 solves eq. (3.13) as follows

---

**Algorithm 2** Joint Transmit Receive Beamforming
 

---

**Input**  $\mathbf{a}(\theta_l, f_d)$ ,  $\sigma_{n_l}^2(f_d) \forall l = 1, \dots, L$ .  
**Output** optimal  $\mathbf{v}_l^*$ ,  $\mathbf{w}_l^*$  for target at each  $f_d$   
**Initialization** randomly select  $\mathbf{v}^1 = [\mathbf{v}_1, \mathbf{v}_2, \dots, \mathbf{v}_L]$ .  
**repeat**  
     Compute  $P_l(f_d)$  from eq. (3.14)  $\forall f_d = f_1, \dots, f_D$ .  
     **for**  $f_d = f_1, f_2, \dots, f_D$  **do**  
         Compute  $\mathbf{w}_l(f_d)$  from (3.19) using  $\mathbf{v}^1$   
         **repeat**  
             Compute  $\mathbf{v}_l(f_d)$  with algorithm 1 using  $P_l(f_d)$ .  
             Compute  $\mathbf{w}_l(f_d)$  from (3.19) using  $\mathbf{v}_l(f_d)$ .  
         **until** convergence  
     **end for**  
**until** convergence

---

### 3.3.3 Numerical Analysis

In this section, numerical results are presented to verify the performance of the algorithm proposed. In the following simulations, a collocated **ULA** is used with  $\lambda/2$  spacing, with 10 elements at the **Tx** and **Rx**, respectively. The array aperture is small that all antennas can view the same aspect of the target, and the noise is white Gaussian with  $\sigma_n^2 = 1$ . It is assumed that the power spectral densities of the targets and their angles are known similar to [LNN07]. The radar signals have a bandwidth of 80 MHz with central frequency of 8 GHz, and the total number of frequency bins are chosen to be 100. It should be noted that as the frequency spacing  $\Delta_f$  decreases, the total number of frequency bins would subsequently increase. This would affect the complexity of Algorithm 2, since the optimization problems  $\mathcal{P}_2$  and  $\mathcal{P}_3$  are solved iteratively per frequency bin. Thus, the choice of a suitable  $\Delta_f$  is important such that captures the variation in the target spectral variance without increasing the complexity of the algorithm. In the simulation results, each point in the figures is acquired by averaging over 500 realizations.

The effectiveness of the presented algorithm is compared to the performance of the same radar but with a conventional beamformer at the transmitter and **MVDR** at the receiver, where the conventional beamformer is defined as

$$\mathbf{v}_l(f_d) = \frac{1}{\sqrt{M}} \mathbf{a}(\theta_l, f_d).$$

### 3.3.4 Beamforming design only

In this set of simulations, the effect of optimizing the beamformers only is examined. This means that the beamformers are optimized without optimizing the waveform, (i.e., without solving problem  $\mathcal{P}_1$ ). Thus, the power allocation and corresponding frequencies are not optimized, and fixed equal power allocation is applied across all frequencies. In more detail, it is assumed that the power is uniformly distributed across the frequency bins without the need of computing  $\mathcal{P}_1$  in eq. (3.14). Thus, in Algorithm 2,  $P_i(f_d) = P_i/100$ ,  $\forall f_d \in \mathcal{W}$ . The spectral variance of the targets ( $\sigma_h^2(f_d)$ ) is chosen similar to various Gaussian shapes.

In the first set of simulations, it is assumed that there are 4 static targets close in the angle at  $60^\circ, 64^\circ, 69^\circ, 70^\circ$ , and the radar system acquires information about them all. The results are shown in terms of **MI** defined in eq. (3.13)) using optimal beamformers  $\mathbf{v}_l^*$  and  $\mathbf{w}_l^*$  for every target, versus the total **SNR** for all targets across the frequency range. The stopping criterion of the algorithm is met when  $\varepsilon = 10^{-4}$ , by which it usually converges after 20-25 iterations on average. It is noticed from Fig. 3.1 that the proposed algorithm outperforms the conventional **MVDR** beamformers in terms of **MI** at close angles, and both curves have different slopes, this means that the information extracted about those targets is higher although their angles are very near.

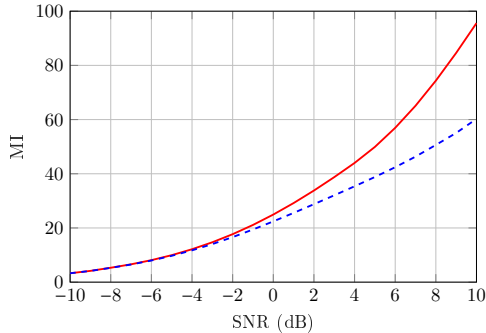


Figure 3.1: Performance comparison of the proposed algorithm(—) and conventional with MVDR beamformers (- - -) for close targets.

In the second set of simulations, the extreme case is simulated, where the targets are very far from each other in angle at  $0^\circ, 45^\circ, 90^\circ, 135^\circ$ , the proposed algorithm gave the same **MI** as the conventional beamformers in Fig. 3.2. Since the interference, in this case, is very low, and target 1, 3, and 2, 4 respectively are orthogonal to each other, so it is optimal to direct the beamformers in the steering vector direction.

In the next set of simulations, we jointly design the beamformers and the waveform using Algorithm 2. The effect of this joint design is shown and compared to only

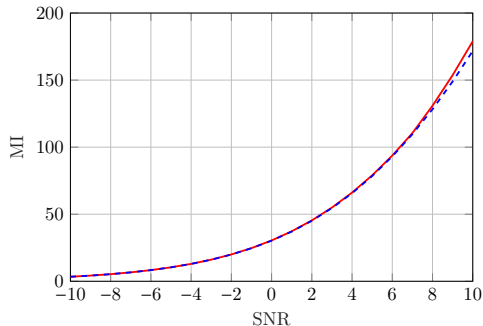


Figure 3.2: Performance comparison of the proposed algorithm (—) and conventional with MVDR beamformers (---) when target 1 & 3 are orthogonal as well as 2 & 4.

designing the waveform as introduced in [LNN07].

### Joint Beamforming and Waveform Design

The authors in [LNN07] used MI to design multiple waveforms for extended targets, using fixed beamformers. In this set of simulations, the joint design proposed in Algorithm 2 is compared to the approach described in [LNN07], where the authors only optimize the power spectrum of the waveforms. Here, we used different spectral variances, to show the effect of interference of multiple targets across the spectrum, as shown in Fig. 3.4a.

Fig. 3.3 first compares both approaches across SNR. It is shown that the MI of the approach in [LNN07] saturate at higher powers where the interference is very high, meanwhile, the optimized beamformers show very good performance at the same powers, since the interference is nulled. This behavior is further explained in Fig. 3.4 showing the spectrum of the transmitted waveforms. On one hand, Fig. 3.4b shows the waveform transmitted for both targets at  $73^\circ$ ,  $70^\circ$  using fixed conventional beamformers as proposed in [LNN07] with total input SNR of 18 dB for the two targets. It is noticed that the two waveforms overlap in many frequencies, although they are spatially near which is not optimal from MI perspective as it may cause interference and information loss. On the other hand, Fig. 3.4c shows the same waveform problem but using the optimized beamformers generated from Algorithm 2, interestingly, the waveforms of the two targets are almost separated across all frequencies, with higher power allocation for some bins, which decreases the interference between both targets and increasing the MI retrieved.

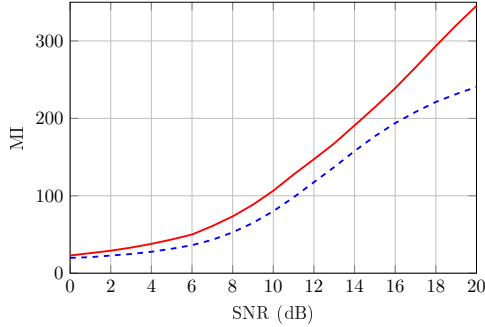


Figure 3.3: Performance comparison of the proposed algorithm in (—) and conventional with MVDR beamformers in (---) when optimal power allocation is used with two targets at  $70^\circ$ ,  $73^\circ$ .

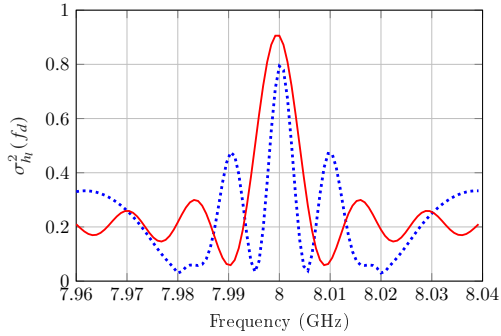
## 3.4 Impact of Spatial Correlation

Comparing Fig. 3.2 and Fig. 3.3, it can be noticed that MI can be greatly affected by correlated targets. Motivated by those results, in this section, we further analyze this behavior on a larger scale. Generally, the spatial correlation among the signals received at the receiver has a great impact on the performance of the MIMO radar. Since highly correlated signals would possibly increase the coherent processing gain, uncorrelated signals would emphasize more the spatial diversity of the target scatterers [FHB<sup>+</sup>06]. Therefore, we need to analyze and model the spatial correlation observed from the different paths between the transmitter and receiver. In [HBC08], the authors provide conditions for correlated and uncorrelated statistical MIMO radars. In this section, those conditions are manipulated and their effect on the MI is analyzed.

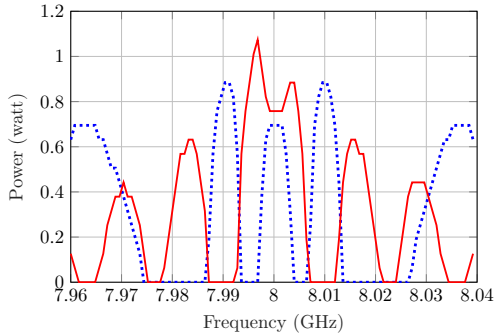
### 3.4.1 Statistical MIMO Radar System Model

Assume an extended target consisting of  $Q$  scatterers, each scatterer is considered independent, and isotropic. The target is illuminated by statistical MIMO radar with widely separated antennas with  $M$  transmitters and  $N$  receivers as in Figure 3.5, with transmitter  $m$  at position  $\rho_m = (x_{tm}, y_{tm})$ , and receiver  $n$  at position  $\rho_n = (x_{rn}, y_{rn})$ . The scattered signal from one scatterer  $q$  located at position  $\rho_q = (x_q, y_q)$ , received at  $\rho_n$  at time instant  $t$  is given by

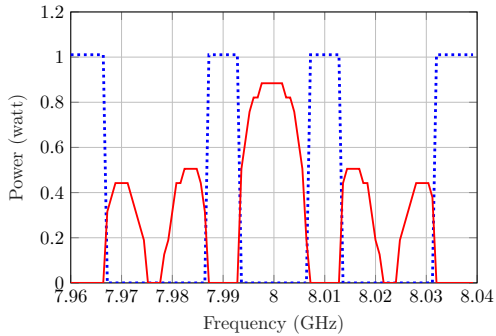
$$y_n^q(t) = \sum_{m=1}^M h_{mn}^q s_m(t - \tau_{tm}(\rho_q) + \tau_{rn}(\rho_q)) + \tilde{n}_n(t), \quad (3.26)$$



(a) Target spectral variance of two targets at  $73^\circ, 70^\circ$  used for waveform design.



(b) Waveform using conventional beamformers



(c) Waveform produced using the jointly optimized beamformers.

Figure 3.4: Effect of beamforming on the waveform design for target 1 (.....) and target 2 (—).

where  $s_m(t)$  is the waveform transmitted by transmitter  $m$ ,  $\tilde{\mathbf{n}}_n(t)$  is the noise at receiver  $n$ . Defining  $h_{mn}$  as the channel from  $m$  to receiver  $n$  for all  $Q$  scatterers, which is given by

$$h_{mn} = \sum_{q=1}^Q \alpha_q \exp(-j2\pi f_c [\tau_{tm}(\rho_q) + \tau_{rn}(\rho_q)]) \quad (3.27)$$

defining  $\alpha_q$  as the reflectivity of the scatterer, which is a zero mean, i.i.d complex Gaussian random variable with the variance of  $1/Q$  [LS08]. In addition, if  $Q$  is large enough, then  $h_{mn}$  will be Gaussian as well. The time delay  $\tau_{tm}(\rho_q) = d(\rho_m, \rho_q)/c$  is the propagation delay between transmitter  $m$  located at position  $\rho_m$  and scatterer  $q$ , where  $d(\rho_m, \rho_q)$  is the distance between  $m$  and  $q$ , and  $c$  is the speed of light. Accordingly  $\exp(-j2\pi f_c \tau_{tm}(\rho_q))$  is the phase shift due to the propagation from  $m$  to  $q$ , and similarly  $\exp(-j2\pi f_c \tau_{rn}(\rho_q))$  is the phase shift due to propagation from scatterer  $q$  till receiver  $n$ , where  $\tau_{rn}(\rho_q)$  is the propagation time delay between  $q$  and  $n$ . Similar to [HBC08], we assume that the bandwidth of the waveform transmitted is not wide enough to resolve individual scatterers. Therefore, we assume that  $s_m(t - \tau_{tm}(\rho_q) + \tau_{rn}(\rho_q)) \approx s_m(t - \tau_{tm}(\rho_0) + \tau_{rn}(\rho_0))$ , where we assume that the radar cross-section of the target (RCS) has a center of gravity located at  $\rho_0 = (x_0, y_0)$ . Furthermore, the path gains  $h_{mn}$  is organized in a  $N \times M$  matrix  $\mathbf{H}$ , as shown in [HBC08], the structure of this matrix is

$$\mathbf{H} = \mathbf{K}\mathbf{\Sigma}\mathbf{G}. \quad (3.28)$$

If  $Q$  is large enough, then the elements of  $\mathbf{H}$  are jointly Gaussian, since  $\alpha_q$  is a complex Gaussian random variable. The transmit paths are organized in a  $Q \times M$  matrix  $\mathbf{G}$ , where  $\mathbf{G} = [\mathbf{g}_1^T; \dots; \mathbf{g}_Q^T]$ , where

$$\mathbf{g}_q^T = [\exp(-j2\pi f_c \tau_{t1}(\rho_q)), \dots, \exp(-j2\pi f_c \tau_{tM}(\rho_q))]. \quad (3.29)$$

The receive paths are in a  $N \times Q$  matrix  $\mathbf{K}$ , where  $\mathbf{K} = [\mathbf{k}_1, \dots, \mathbf{k}_Q]$ , and

$$\mathbf{k}_q^T = [\exp(-j2\pi f_c \tau_{r1}(\rho_q)), \dots, \exp(-j2\pi f_c \tau_{rN}(\rho_q))]. \quad (3.30)$$

The reflectivity of all scatterers is organized in a diagonal  $Q \times Q$  matrix  $\mathbf{\Sigma}$ , where  $\mathbf{\Sigma} = \text{diag}([\alpha_1, \dots, \alpha_Q])$ , and  $\mathbf{\Sigma} \sim \mathcal{CN}(0, \mathbf{R}_\alpha)$ .

If the number of samples in the duration of the transmitted waveform is denoted by  $K_s$ , then we can obtain the total received signal across all  $K_s$  time samples as

$$\mathbf{y}_n = \mathbf{h}_n^T \mathbf{S}^T + \tilde{\mathbf{n}}_n, \quad (3.31)$$

where  $\mathbf{y}_n = [y_n(1) y_n(2) \dots y_n(K_s)]$ ,  $\mathbf{h}_n = [h_{1n} h_{2n} \dots h_{Mn}]^T$ ,  $\mathbf{S} = [\mathbf{s}(1) \mathbf{s}(2) \dots \mathbf{s}(K_s)]^T$ , where  $\mathbf{s}(k_s) = [s_1(k_s) s_2(k_s) \dots s_M(k_s)]$ . We assume that  $K_s \geq \max(M, N)$ . From eq. (3.31), we define the received signal from all the antennas as

$$\mathbf{Y} = \mathbf{S}\mathbf{H} + \tilde{\mathbf{N}}, \quad (3.32)$$

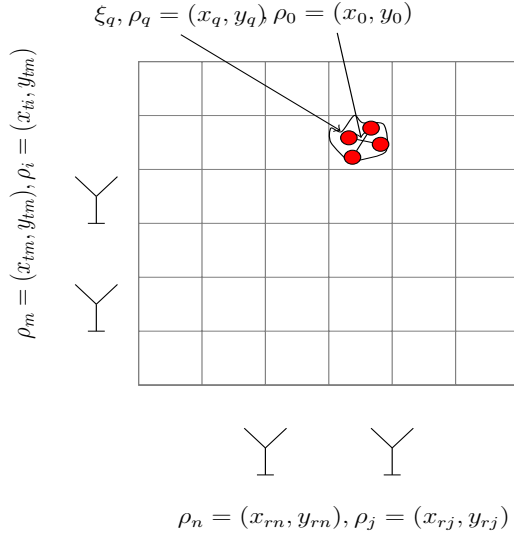


Figure 3.5: MIMO radar with an extended target, containing of four point targets.

in which  $\mathbf{Y} \in \mathbb{C}^{K_s \times N}$ ,  $\mathbf{Y} = [\mathbf{y}_1 \mathbf{y}_2 \dots \mathbf{y}_N]$ ,  $\mathbf{H} \in \mathbb{C}^{N \times M}$  is the target scattering matrix containing all the path gains  $h_{mn}$  from transmit to receive antennas,  $\tilde{\mathbf{N}} \in \mathbb{C}^{K_s \times N}$  is a colored noise matrix with independent and identically (i.i.d) distributed columns, where  $\tilde{\mathbf{N}} = [\tilde{\mathbf{n}}_1 \tilde{\mathbf{n}}_2 \dots \tilde{\mathbf{n}}_N]$ . Moreover we define  $\tilde{\mathbf{y}} = \text{vec}(\mathbf{Y})$ ,  $\tilde{\mathbf{h}} = \text{vec}(\mathbf{H})$ , and  $\tilde{\mathbf{n}} = \text{vec}(\tilde{\mathbf{N}})$ , where  $\text{vec}(\mathbf{X})$  is obtained by column wise staking of the matrix  $\mathbf{X}$ . Consequently, eq. (3.32) can be rewritten as

$$\tilde{\mathbf{y}} = \tilde{\mathbf{S}}\tilde{\mathbf{h}} + \tilde{\mathbf{n}}, \quad (3.33)$$

where  $\tilde{\mathbf{S}} = \mathbf{I}_N \otimes \mathbf{S}$ . We assume that  $\mathbf{H}$  and  $\tilde{\mathbf{N}}$  are independent, with distributions

$$\tilde{\mathbf{h}} \sim \mathcal{CN}(0, \mathbf{R}_{\tilde{\mathbf{h}}}),$$

$$\tilde{\mathbf{n}} \sim \mathcal{CN}(0, \mathbf{R}_{\tilde{\mathbf{n}}}),$$

where  $\mathbf{R}_{\tilde{\mathbf{h}}} \in \mathbb{C}^{MN \times MN}$  is the positive semidefinite correlation matrix of the target, defined as  $\mathbf{R}_{\tilde{\mathbf{h}}} = \mathbb{E}[\tilde{\mathbf{h}}\tilde{\mathbf{h}}^H]$ , and  $\mathbf{R}_{\tilde{\mathbf{n}}} \in \mathbb{C}^{NK_s \times NK_s}$  is a positive semidefinite correlation matrix of the noise.

The target channel vector  $\tilde{\mathbf{h}}$  can be defined as <sup>4</sup>

$$\begin{aligned} \tilde{\mathbf{h}} &= \text{vec}(\mathbf{H}) = \text{vec}(\mathbf{K}\mathbf{\Sigma}\mathbf{G}) \\ &= (\mathbf{G}^T \otimes \mathbf{K}) \text{vec}(\mathbf{\Sigma}) \end{aligned} \quad (3.34)$$

<sup>4</sup> $\text{vec}(\mathbf{ABC}) = (\mathbf{C}^T \otimes \mathbf{A}) \text{vec}(\mathbf{B})$



Therefore,  $\mathbf{R}_{\bar{\mathbf{h}}}$  can be rewritten in terms of  $\mathbf{R}_{\alpha}$  as

$$\mathbf{R}_{\bar{\mathbf{h}}} = (\mathbf{G}^T \otimes \mathbf{K}) (\mathbf{I} \otimes \mathbf{R}_{\alpha}) (\mathbf{G}^T \otimes \mathbf{K})^H. \quad (3.35)$$

Let the eigendecomposition of  $\mathbf{R}_{\bar{\mathbf{h}}}$  and  $\mathbf{R}_{\bar{\mathbf{n}}}$  be

$$\mathbf{R}_{\bar{\mathbf{h}}} = \mathbf{U}_h \boldsymbol{\Sigma}_h \mathbf{U}_h^H,$$

$$\mathbf{R}_{\bar{\mathbf{n}}} = \mathbf{U}_{\bar{\mathbf{n}}} \boldsymbol{\Sigma}_{\bar{\mathbf{n}}} \mathbf{U}_{\bar{\mathbf{n}}}^H,$$

where  $\mathbf{U}_h$ ,  $\mathbf{U}_{\bar{\mathbf{n}}}$  are unitary matrices, while  $\boldsymbol{\Sigma}_h$ , and  $\boldsymbol{\Sigma}_{\bar{\mathbf{n}}}$  are diagonal matrices, with vectors  $\boldsymbol{\sigma}_h$ ,  $\boldsymbol{\sigma}_{\bar{\mathbf{n}}}$  on the diagonals respectively, such that  $\boldsymbol{\sigma}_h = ([\sigma_{h,1}, \sigma_{h,2}, \dots, \sigma_{h,MN}])$ ,  $\boldsymbol{\sigma}_{\bar{\mathbf{n}}} = ([\sigma_{\bar{\mathbf{n}},1}, \sigma_{\bar{\mathbf{n}},2}, \dots, \sigma_{\bar{\mathbf{n}},NK}])$  are diagonal matrices whose elements are arranged in descending order. It should be noted that  $\mathbf{R}_{\bar{\mathbf{h}}}$  has MN singular values, and we always assume that  $Q$  is large enough, such that  $MN \leq Q$ .

### 3.4.2 Measure of Spatial correlation of MIMO Radar

In the previous section, the system model for a widely separated MIMO radar was introduced, where a stochastic model was presented for the channel  $\mathbf{H}$  whose elements are the path gains from the  $\mathbf{T}\mathbf{x}$  to the  $\mathbf{R}\mathbf{x}$ . Based on this model, multiple questions might rise: what makes different path gains correlated or de-correlated? Furthermore, if a correlation exists, would the MI be affected in this case as previously noticed in Fig. 3.2 and Fig. 3.3? Most importantly, what is a proper metric to compare the correlation between two channels? Is the statistical definition of correlation enough in this case? This section and the next one, address those questions. Initially, we answer the first question by providing specific conditions that control the correlation relationship between the channel elements.

Suppose that there are two transmit antennas at locations  $\rho_m = (x_{tm}, y_{tm})$  and  $\rho_i = (x_{ti}, y_{ti})$  respectively, while the receive ones are at  $\rho_n = (x_{rn}, y_{rn})$  and  $\rho_j = (x_{rj}, y_{rj})$  respectively as shown in Figure 3.5. Furthermore, the target is located at  $\rho_0$  whose dimensions are defined as  $d_x$  along the x-axis and  $d_y$  along the y-axis. Are the path gains  $h_{mn}$  (i.e., path from  $\mathbf{T}\mathbf{x}$  antenna at  $\rho_m$  to  $\mathbf{R}\mathbf{x}$  antenna at  $\rho_n$ ) and  $h_{ij}$  correlated or not?

According to the derivation provided in [FHB<sup>+</sup>06], if at least one of the following conditions is met, then the channel is considered as uncorrelated.

$$\begin{aligned} \frac{x_{tm}}{d(\rho_m, \rho_0)} - \frac{x_{ti}}{d(\rho_i, \rho_0)} &> \frac{\lambda_c}{d_x} \\ \frac{y_{tm}}{d(\rho_m, \rho_0)} - \frac{y_{ti}}{d(\rho_i, \rho_0)} &> \frac{\lambda_c}{d_y} \\ \frac{x_{rn}}{d(\rho_n, \rho_0)} - \frac{x_{rj}}{d(\rho_j, \rho_0)} &> \frac{\lambda_c}{d_x} \\ \frac{y_{rn}}{d(\rho_n, \rho_0)} - \frac{y_{rj}}{d(\rho_j, \rho_0)} &> \frac{\lambda_c}{d_y}, \end{aligned} \quad (3.36)$$

where  $\lambda_c$  is the operating wavelength.

Using the example provided in [FHB<sup>+</sup>06] for clarification if the target is at a distance  $d = 10^4\lambda_c$  and with dimension,  $d_x$  or  $d_y = 10\lambda_c$ , then the separation between the antennas  $\rho_m$  and  $\rho_i$  must be of order  $10^3\lambda_c$  to have a spatially de-correlated paths. In this context, the target can be viewed as an antenna with aperture  $d_x$  illuminating the two transmit antennas. Then, the channel elements de-correlate if the spacing between both antennas is large enough such that they do not fall in the same beamwidth illuminated by the target. This example illustrates how one factor (i.e., the spacing between the antennas) can affect the spatial de-/correlation. However, as noticed from the previous conditions, other factors contribute to the correlation of the channel. Those factors are:

1. Spacing between transmit/receive antennas
2. Operating frequency
3. Target Dimensions
4. Distance between the target and the antennas.

Next, we further explore how correlation can be mathematically described and how to measure whether one channel matrix is more correlated than the other.

Normally in statistics, a diagonal covariance matrix demonstrates that the random variables are uncorrelated, independent from the values of auto-covariances on its diagonal. This measure will not be enough to compare two channels if their paths are uncorrelated but have different powers. Hence, in the next definition, a new measure is introduced to compare different covariance matrices in addition to their statistical independence. This definition is derived using Majorization theory previously explained in 2.3.

*Definition 4* ([JB07, Definition 4.2]). If we have two arbitrary target covariance matrices,  $\mathbf{R}_h^1$  and  $\mathbf{R}_h^2$ , with eigenvalues  $\sigma_{h_1}$ , and  $\sigma_{h_2}$  respectively, arranged in descending order such that  $\sigma_{h_{1,1}} \geq \sigma_{h_{1,2}} \geq \dots \geq \sigma_{h_{1,T}} \geq 0$  and  $\sigma_{h_{2,1}} \geq \sigma_{h_{2,2}} \geq \dots \geq \sigma_{h_{2,T}} \geq 0$ , where  $T = MN$ , with constraint that  $\text{tr}(\mathbf{R}_h^1) = \text{tr}(\mathbf{R}_h^2)$ . we say that  $\mathbf{R}_h^1$  is more correlated than  $\mathbf{R}_h^2$ , if  $\sigma_{h_1} \succcurlyeq \sigma_{h_2}$  such that

$$\sum_{l=1}^L \sigma_{h_{1,l}} \geq \sum_{l=1}^L \sigma_{h_{2,l}} \quad \text{for } 1 \leq L \leq T - 1. \quad (3.37)$$

This definition can be intuitively described as the larger the first  $L$  eigenvalues of the channel covariance matrix, the more correlated the channel is. Thus, according to Definition 4, the random variables are considered uncorrelated, if the covariance matrix is diagonal, in addition to having equal auto-covariances values on the diagonal [JB07, Remark 4.1].

*Example 1.* If  $\mathbf{R}_{\mathbf{h}}^1$  and  $\mathbf{R}_{\mathbf{h}}^2$  are both diagonal matrices, with eigenvalues  $\boldsymbol{\sigma}_{h_1} = [4, 0, 0, 0]$ , and  $\boldsymbol{\sigma}_{h_2} = [1, 1, 1, 1]$  respectively, then  $\mathbf{R}_{\mathbf{h}}^1$  is extremely correlated, while  $\mathbf{R}_{\mathbf{h}}^2$  is totally uncorrelated.<sup>5</sup>

### 3.4.3 The Effect of Spatial Correlation on MI-based waveform

The measure of correlation defined in Definition 4 allows us to analyze the impact of spatial correlation on performance measures for different channels. In this section, we will revisit the MI-based waveform design problem but for widely separated MIMO radars (unlike colocated MIMO radar model in 3.3.1). We will investigate how the waveform design for maximizing the MI between  $\tilde{\mathbf{y}}$  and  $\tilde{\mathbf{h}}$  can be affected by the spatial correlation of  $\tilde{\mathbf{h}}$ . First, we derive the optimal waveform for the widely separated MIMO system model in the following.

The expression of mutual information between  $\tilde{\mathbf{y}}$ , and  $\tilde{\mathbf{h}}$ , if the transmitted waveform is known, in a matrix form is given by [TTP10]

$$I(\tilde{\mathbf{y}}; \tilde{\mathbf{h}}|\tilde{\mathbf{S}}) = N[\log[\det(\tilde{\mathbf{S}}\mathbf{R}_{\tilde{\mathbf{h}}}\tilde{\mathbf{S}}^H + \mathbf{R}_{\tilde{\mathbf{h}}}) - \log \det(\mathbf{R}_{\tilde{\mathbf{h}}})]]. \quad (3.38)$$

Then, the optimization problem of waveform design to maximize the MI with a total power constraint of  $P_T$  can be formulated as

$$\begin{aligned} \max_{\tilde{\mathbf{S}}} \quad & \log[\det(\tilde{\mathbf{S}}\mathbf{R}_{\tilde{\mathbf{h}}}\tilde{\mathbf{S}}^H\mathbf{R}_{\tilde{\mathbf{h}}}^{-1} + \mathbf{I}_{\text{NK}})] \\ \text{s.t.} \quad & \text{tr}(\tilde{\mathbf{S}}\tilde{\mathbf{S}}^H) \leq P_T. \end{aligned} \quad (3.39)$$

*Lemma 2.* [Fie71] The optimal structure of  $\tilde{\mathbf{S}}$  to satisfy (3.39) is the following

$$\tilde{\mathbf{S}}_{\text{opt}} = \mathbf{U}_{\tilde{\mathbf{h}}} \left[ \mathbf{0}_{\text{MN} \times (\text{NK} - \text{MN})} \quad \boldsymbol{\Sigma}_{\mathbf{s}}^{1/2} \right]^T \mathbf{U}_{\mathbf{H}}^H. \quad (3.40)$$

$\boldsymbol{\Sigma}_{\mathbf{s}}$  is a square diagonal matrix,  $\boldsymbol{\Sigma}_{\mathbf{s}} \in \mathbb{C}^{\text{MN} \times \text{MN}}$  with elements  $\sigma_{s,i}$  on its diagonal. This means that the left and right singular vectors of the optimal waveform must be equal to the eigenvectors of the noise and the Hermitian of the channel matrices respectively [TTP10].

In more details, in eq. (3.40), the left singular vector of the optimum waveform refers to the eigenvector of the noise covariance matrix in increasing order, while the right singular values refer to the eigenvector of the covariance matrix which should be in decreasing order, i.e. the eigenvalues of the noise and the target are sorted in oppositional order according to the following theorem.

*Theorem 2.* [Fie71] For positive semidefinite matrices  $\mathbf{A}$  and  $\mathbf{B}$ , with eigenvalues  $\alpha_1 \geq \alpha_2 \dots \geq \alpha_n$ ,  $\beta_1 \geq \beta_2 \dots \geq \beta_n$ .

$$\prod_{i=1}^n (\alpha_i + \beta_i) \leq \det(\mathbf{A} + \mathbf{B}) \leq \prod_{i=1}^n (\alpha_i + \beta_{n+1-i}). \quad (3.41)$$

<sup>5</sup>In this chapter, the correlation as per Definition 4 will be referred as *spatial correlation*, while through out the thesis, the usual statistical correlation will be referred only as *correlation*.

Hence, if the eigenvalue decomposition of  $\mathbf{A} = \mathbf{U}_A \mathbf{\Lambda}_A \mathbf{U}_A^H$  and  $\mathbf{B} = \mathbf{U}_B \mathbf{\Lambda}_B \mathbf{U}_B^H$ , then the upper bound is achieved for  $\mathbf{U}_A = \mathbf{P} \mathbf{U}_B$ , where  $\mathbf{P}$  is a permutation matrix with ones on the anti-diagonal such that

$$\mathbf{P} = \begin{bmatrix} 0 & 0 & \dots & 1 \\ 0 & \dots & 1 & 0 \\ \vdots & \vdots & \vdots & \vdots \\ 1 & 0 & \dots & 0 \end{bmatrix},$$

and the lower bound is achieved for  $\mathbf{U}_A = \mathbf{U}_B$ . Eq. (3.40) only provides the optimal structure of the matrix to satisfy problem (3.39), however, the optimal power allocation must yet be found. Hence, to solve for the optimal transmit power allocation, we must solve for the singular values  $\sigma_{s,i}$  in matrix  $\mathbf{\Sigma}_s$  of the optimal waveform  $\tilde{\mathbf{S}}_{\text{opt}}$  in eq. (3.40). Thus, rewriting eq. (3.39) as

$$\begin{aligned} \max_{\sigma_{s,i}} \quad & \sum_{i=1}^{\text{MN}} \log \left( \frac{\sigma_{s,i} \sigma_{h,i}}{\sigma_{\bar{n}, \text{MN}-i+1}} + 1 \right) \\ \text{s.t.} \quad & \sum_{i=1}^{\text{MN}} \sigma_{s,i} \leq P_T, \end{aligned} \tag{3.42}$$

then we can obtain the optimal solution using the celebrated water filling algorithm [TTP10], such that

$$\sigma_{s,i} = \left( \frac{1}{\lambda} - \frac{\sigma_{\bar{n}, \text{MN}-i+1}}{\sigma_{h,i}} \right)^+,$$

where  $\lambda$  is the water-level and is determined based on the total power, by solving the following equation

$$\sum_{i=1}^{\text{MN}} \left( \frac{1}{\lambda} - \frac{\sigma_{\bar{n}, \text{MN}-i+1}}{\sigma_{h,k}} \right)^+ = P_T.$$

### Schur Convexity Analysis of MI Expression

In this subsection, we analyze how the MI of the proposed optimal waveform described previously can be affected by spatial correlation. Since, according to Definition 4, the eigenvalues of two different covariance matrices can be compared using Majorization theory as defined in section 2.3, eq. (2.3). Thus, since the MI is a function of the eigenvalues of the target covariance matrix, then subsequently the MI can be defined as a Schur-convex or Schur-concave function with respect to those eigenvalues (see Definition 2). Recall that those functions are order-preserving functions. Accordingly, this can give further explanation of how the function behaves with respect to the correlation of signals reflected from the target scatterers. In what next, the Schur convexity/concavity of the MI will be proven.

As per Lemma 2, the eigenvalues of the noise and the target are assumed to be

in oppositional order to obtain the optimum solution, as explained in Theorem 2. Therefore, we rewrite the MI in eq. (3.42) as

$$f(\sigma_{h,i}) = \sum_{i=1}^{MN} \log \left( \frac{\sigma_{s,i} \sigma_{h,i}}{\sigma_{\bar{n},MN-i+1}} + 1 \right). \quad (3.43)$$

Hence, to prove the Schur convexity or concavity of the function, we use Theorem 1 to check for the Schur condition defined in Lemma 1 with respect to the eigenvalue of  $\sigma_h$ . Recall from Lemma 1, we need to calculate the following

$$(\sigma_{h,i} - \sigma_{h,j}) \left( \frac{\partial f}{\partial \sigma_{h,i}} - \frac{\partial f}{\partial \sigma_{h,j}} \right) \geq 0 \quad \forall 1 \leq i, j \leq n, \quad (3.44)$$

To do this, we take the partial derivative of eq. (3.43) such that <sup>6</sup>

$$\frac{\partial f}{\partial \sigma_{h,i}} = \frac{\sigma_{s,i}}{\sigma_{h,i} \sigma_{s,i} + \sigma_{\bar{n},MN-i+1}}. \quad (3.45)$$

Since elements of  $\sigma_h$  are arranged in descending order,  $(\sigma_{h,i} - \sigma_{h,j}) \geq 0$ . Hence, the Schur convexity of MI is dependent on the sign of

$$\frac{\partial f}{\partial \sigma_{h,i}} - \frac{\partial f}{\partial \sigma_{h,j}},$$

which is defined as

$$\frac{\sigma_{s,i}}{\sigma_{h,i} \sigma_{s,i} + \sigma_{\bar{n},MN-i+1}} - \frac{\sigma_{s,j}}{\sigma_{h,j} \sigma_{s,j} + \sigma_{\bar{n},MN-j+1}}, \quad (3.46)$$

is totally dependent on the optimum power allocation values and the noise eigenvalues. Since, the water-filling solution in eq. (3.42) is dependent on the SNR, therefore, the behavior of the function will be analyzed in four cases: at high and low SNR for colored and non-colored noise.

*Lemma 3.* In case of non-colored, independent, identically distributed (i.i.d) noise, in high SNR regimes, the water-filling solution to eq. (3.42) is given by  $\sigma_s = \frac{P_T}{MN} \mathbf{1}^T$  (equal power allocation  $p$ ), hence, eq. (3.46) would be always smaller than zero, hence Schur-concave. However, in low SNR regimes, the solution of eq. (3.42) would be  $\sigma_s = [P_T, 0, \dots, 0]$ , where the power is only given for the strongest eigenmode of the target. Consequently, eq. (3.46) would be always positive, since the second term in (3.46) would be 0, and the first term is positive, then according to Lemma 1, the function is Schur-convex.

*Theorem 3.* In case of colored-noise, in high SNR regimes, eq. (3.46) is Schur-convex if

$$\max_{1 \leq i < j \leq MN} \frac{\sigma_{h,i} - \sigma_{h,j}}{\sigma_{\bar{n},MN-j+1} - \sigma_{\bar{n},MN-i+1}} \leq \frac{1}{p}, \quad (3.47)$$

and Schur-concave otherwise, where  $p = \frac{P_T}{MN}$ .

<sup>6</sup>To use Theorem 1, we assume that  $\sigma_h$  is a partially ordered vector,  $\sigma_{h,i} > \sigma_{h,j}$ .

instance	i	j	(3.47)
1	1	2	3
2	1	3	2
3	1	4	0.75
4	2	3	1
5	2	4	0.3
6	3	4	0.125

Table 3.1: Evaluation of eq. (3.47) using values in example 2

*Proof.* We can further simplify eq. (3.46) to be the following

$$\left( \sigma_{h,i} + \frac{\sigma_{\bar{n},MN-i+1}}{\sigma_{s,i}} \right)^{-1} - \left( \sigma_{h,j} + \frac{\sigma_{\bar{n},MN-j+1}}{\sigma_{s,j}} \right)^{-1}. \quad (3.48)$$

Hence, in order for eq. (3.48) to be greater than 0, then the following must apply

$$\sigma_{h,i} + \frac{\sigma_{\bar{n},MN-i+1}}{\sigma_{s,i}} \leq \sigma_{h,j} + \frac{\sigma_{\bar{n},MN-j+1}}{\sigma_{s,j}}, \quad (3.49)$$

since in high SNR regimes, the optimal water-filling solution is nearly equal to power allocation  $\sigma_{s,i} = \sigma_{s,j} = p$ . Therefore, after some mathematical reordering in eq. (3.49), we can get the result in eq. (3.47).  $\square$

*Example 2.* If we assumed  $MN = 4$ ,  $\sigma_h = [5, 2, 1, 0.5]$  and  $\sigma_{\bar{n}} = [8, 4, 3, 2]$ . Then we have 6 cases demonstrated in Tab. 3.1 with their corresponding values of the left-hand side (L.H.S) of eq. (3.47). The maximum value of eq. (3.47) here occurs when  $i = 1$ , and  $j = 2$ , therefore in order to apply Theorem 3, then  $p = \frac{1}{3}$ .

In low SNR, the effect of colored noise will not be significant, as only the first eigenmode of the target would be triggered, hence lemma 3 will hold as well in case of low SNR with colored noise.

This changing behavior of the MI in low and high SNR, gives an indication that according to Definitions 3 and 4, spatially correlated channels behave better in low SNR, however in high SNR, it is better to have an uncorrelated channel.

In the following section, we simulate this changing behavior by controlling the spatial correlation. Moreover, for further insights, we manipulate the spatial correlation conditions for MIMO radar which were previously discussed in section 3.4.1, by changing the operating frequency and analyzing its effect in low and high SNR.

### 3.4.4 Numerical Analysis

In the first set of simulations, the performance of the MI function is analyzed across different spatial correlations. In theorem 3, it is proven that MI has a changing

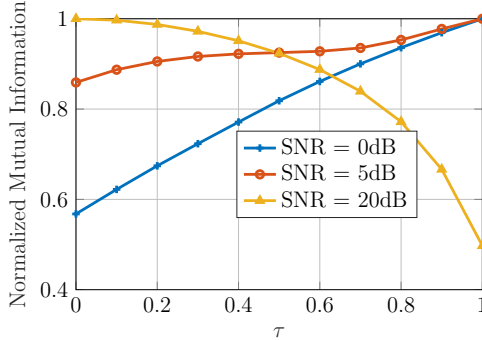


Figure 3.6: Normalized Mutual Information (MI) (with respect to the maximum value) as a function of  $\tau$  which represents the degree of correlation ( $\tau = 0$  totally uncorrelated,  $\tau = 1$  totally correlated channel) for different total SNR values (0 dB, 5 dB, and 20 dB) assuming colored noise.

behavior in high and low SNR regimes. Here, we illustrate this behavior through numerical evaluation. We assume that  $M = N = 2$  and  $K_s = 2$ . The eigenvalues of  $\mathbf{R}_n$  for colored noise case are  $[8, 4, 3, 2]$ . We keep the eigenvalues of the noise fixed, and change the total power value to vary the SNR. In order to simulate the effect of correlation, the eigenvalues of  $\mathbf{R}_h$  are defined as  $\sigma_h = \tau * [1, 0, 0, 0] + (1 - \tau)[0.25, 0.25, 0.25, 0.25]$ , hence, the eigenvalues will vary from uncorrelated when  $\tau = 0$  to highly correlated when  $\tau = 1$ .

In figure 3.6, the MI is plotted across different SNR values, and the MI is normalized at each SNR, where at SNR 0, it can be seen that the MI is increasing as the correlation increases. Since the MI is Schur-convex at low SNR, it increases with increasing the correlation. However, when the SNR is increased to be 20 dB, the function has a decreasing behavior since it is Schur-concave at high SNR, where the maximum of MI is achieved when  $\tau=0$ , and then decreases with increasing the correlation. Yet, at intermediate SNR at 5 dB, the function is behaving neither Schur-convex nor concave.

### 3.4.5 Spatially Correlated MIMO Radar Setup

In the second set of simulations, we simulate the scenario in Figure 3.5 using the model of a widely separated MIMO radar with  $M = 2$  and  $N = 2$ . Here, we want to check the effect of the operating frequency on the spatial correlation conditions in eq. (3.36). Hence, we carefully chose the other factors defined in eq. (3.36) such that they will not affect the correlation, to verify the effect of frequency. Hence, the coordinates of the transmitter are (2,4.8) and (2,2.4) meters, while the receivers are located at (0,2) and (0,4). We assume that there is a distributed target with

$Q = 1000$ , its center is located at  $(2,2)$  meters, and  $d_x = d_y = 2\text{m}$ . The parameters are chosen such that we have two different channels  $\mathbf{H}$ , one spatially correlated by violating the rules in eq. (3.36), and the other matrix spatially de-correlated. From the four factors stated, we changed the first working frequency to be  $f_c = 0.1\text{ GHz}$ , which makes the channel correlated, while in the second case  $f_c = 8\text{ GHz}$ , decreasing  $\lambda_c$  and therefore obeying the mentioned conditions. Figure 3.7 shows the performance of MI at both frequencies, which agrees with the behavior explained before since the low-frequency curve performs better at low SNR, where the spatial correlation is high. This agrees with corollary 3 where at low SNR the function is Schur-convex. However, as the SNR increases, the high-frequency curve achieves higher MI, since the spatial correlation decreases. Accordingly, to achieve maximum MI at high SNR, the channel elements must be de-correlated. It is worth noting that those results are derived based on using MI as a reference for the radar performance. However, the effect of correlation in low SNR on DOA estimation requires further investigation. It is known that correlation among different paths coming from different targets might degrade the estimation performance as discussed later in chapter 6. Since the Rx can not differentiate between them and estimate their individual DOA. Meanwhile, if those paths are coming from the same target, the correlation might overcome the low SNR, improving the performance. This investigation is however left to future work.

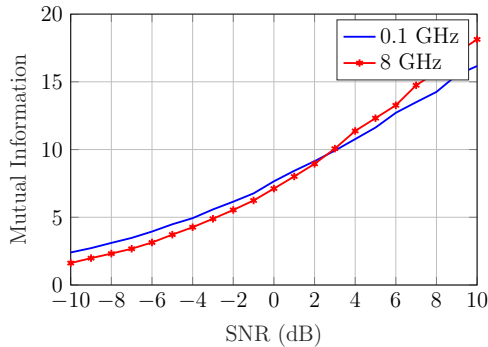


Figure 3.7: Mutual Information as a function of SNR for two different operating frequencies at 0.1 GHz (highly correlated channel) and 8 GHz (less correlated channel) showing the change in behavior of MI function in high and low SNR .

### 3.5 Summary

In the first part of this chapter, a novel joint transmit-receive beamforming algorithm was proposed under a multiple extended targets interference scenario. The beamform-



ers were obtained to maximize the **MI** through two-step optimization. Significantly, the optimized beamformers enhance the **MI** in high interference cases, where the targets overlap in frequency range compared to the conventional method. As the targets become sufficiently far from each other, it is optimal to direct the transmit beamformers in the steering vector direction, as the interference is low in this case. Moreover, the effect of the jointly optimized beamformers was investigated on the waveform design. The newly generated waveforms were separated across the frequency range, offering better **MI**, unlike conventional beamformers which fail to avoid interference at high powers. In the second part, we further investigated the effect of spatial correlation in a statistical MIMO radar. We used **MI** between the target random response and the reflected signal as a metric in presence of colored noise. We proved that **MI** is a Schur-convex function with respect to spatial correlation at low **SNR**, i.e. monotonically increasing function. Contrarily, this behavior changes at high **SNR**, and the function is Schur-concave. Moreover, we applied those findings to statistical MIMO radar setup, by changing the operating frequency to control the spatial correlation of the reflected paths. The simulations show that at low **SNR**, the performance of the radar is better at low frequencies, which is surpassed by the high-frequency operating radar at high **SNR** conditions.



## 4 RL based cognitive Beamforming

In chapter 3, we studied the optimal beamforming design for MIMO radar from information theoretic perspective. We assumed that the radar has prior information about the surrounding environment (i.e., number, location of the targets and interference). This can be justified in a target identification mode, when the targets are already detected. However, in this chapter, we assume a target acquisition mode, where the radar has no information about the surrounding. We further assume the existence of disturbance (i.e., clutter plus noise) of unknown statistics. In addition, the radar scene is dynamic, which may be due to the fact that the targets are changing their directions or fading. Here, we utilize the benefits of RL to solve such problem. Furthermore, we investigate the application of MMIMO radar to provide an asymptotic bound on the performance. In section 4.1, we provide a literature overview of MMIMO radars along with the use of ML for radar signal processing. In addition, we summarize the main contributions of this chapter. Afterwards, in 4.2 we discuss the system model and the detection problem. In 4.3, we propose a novel algorithm for multi-targets detection with the aid of RL. We propose a new approach to solve the beamforming optimization problem, reducing the computational complexity of such problem in 4.4. The performance of the algorithm against various static and dynamic environments is examined through extensive simulations in 4.5. Finally, the chapter is concluded in section 4.6.

### 4.1 Related Work

Recently, MMIMO has transformed from just an idea [Mar10] to reality, where commercial solutions with up to 64 fully digital transceivers are adopted for 5G [Hua] Specifically, in this chapter, we focus on colocated MMIMO. The MMIMO radar has been recently shown to be able to provide robustness against the unknown disturbance distribution [FSG<sup>+</sup>20]. Moreover, as foreseen in [BSW<sup>+</sup>19, OMBK17], thanks to its higher DoF, a MMIMO can detect small unmanned vehicles (UAV) whose RCS can be up to three orders of magnitude smaller than manned vehicles. However, together with these benefits, the MMIMO paradigm brings with it new challenging issues. One of the main open problems of MMIMO radar is the design of robust algorithms for detection and estimation with scalable complexity as the number of deployed antennas increases. Moreover, cognitive MMIMO radar, requires optimizable waveforms [GGSB18]. Hence, the design of scalable and fast accurate optimization algorithms is necessary. The current existing work relying on semi-definite programming (SDP) to solve the beampattern optimization problem would

impose further computational complexity and processing overhead on the **MMIMO** problem. This is due to the fact that in those papers, the beamforming is done over two computationally demanding steps. In the first step, the covariance matrix is optimized. In the second step, this matrix is used to synthesize the beamformers. Complementary and equally essential to the waveform diversity at the transmitter, is the receiver cognition, which guides the radar decisions and controls the choice of the waveforms. In [Hay06, BBS<sup>+</sup>15, HXS12], the authors utilized Bayesian filtering for the perception-action cycle, where the receiver makes probabilistic predictions on the next environmental state given the current state. This approach however may lead to model mismatches as it depends on prior information on the environment's statistics. To avoid this dependence, **RL** is adopted for cognitive radars in [LLH<sup>+</sup>19, ZZY08].

**RL** is a learning approach addressing model-free problems by using software-defined agents, which learn from the observations collected from the environment, and take the best possible actions according to a reward function [SB18]. Those interactions with the environment are formally described as a **Markov decision process (MDP)** as previously explained in section 2.5.2. The use of machine learning with CR has been recently explored in the literature. In [LLH<sup>+</sup>19, ZZY08] **RL-CR** is used for dynamic spectrum allocation, while in [JHS19] the authors use CR for target detection in an end-to-end learning approach. They propose an alternating procedure to jointly design the transmit waveform and the detector. A neural network is used to approximate the *generalized likelihood ratio test (GLRT)* while the transmit waveform is fixed. Consequently, for a fixed detector, they train the transmitted waveform using deep **RL**. However, there is no statistical guarantee on the resulting detection performance that may seriously degrade in the presence of a mismatch between the actual disturbance model and the one used for training. Moreover, they don't address multi-target detection.

In [MBH15], the authors use machine learning approaches to estimate the optimal detection threshold, based on a non-linear transformation of the order statistics. They use an offline library for the disturbance distributions, where they assume a priori known covariance matrix to build this library.

In [GGDD20], **RL** has been used in indoor mapping for **UAV** applications. Mechanical beamforming using the **UAV** rotation is used for target detection. However, only Gaussian noise is considered in the detection algorithm.

In the context of **MMIMO**, the work in [JLY16] exploits random matrix theory to analyze the detection performance. However, the approach proposed in [JLY16] requires the cumbersome requirement of many observations.

Unlike the previous approaches, we propose a fully data-driven algorithm that does not require any offline knowledge of possible disturbance distributions nor their covariance matrix and thus avoids issues with model mismatches.

Compared to the previous references, the contribution of this chapter can be summarized as the following :

1. We derive an original **RL-based MMIMO CR** detection algorithm in the presence

of disturbance that does not rely on any prior information about the statistical model of the disturbance, or the number of targets, while maintaining the **constant false alarm rate (CFAR)** property.

2. By exploiting the specific feature of a **MMIMO** system described in [FSG<sup>+</sup>20, Corollary 1], we propose a reward function calculated in terms of the probability of detection ( $P_D$ ) regardless of the disturbance distribution.
3. We propose a beamforming optimization approach that can scale up with a large number of antennas, where we optimize directly for the beamforming matrix without the need to optimize for the covariance matrix first.
4. As suggested by the numerical results, the algorithm is able to detect low **SNR** targets with a radar operating under a constraint on the probability of false alarm  $P_{FA} = 10^{-5}$ . Moreover, it is robust to environmental changes, e.g., it can detect fading targets and targets changing their angular positions.
5. We analyze the overall robustness of the detector across different (unknown) disturbance distributions.

## 4.2 Problem Formulation

We consider a colocated **MIMO** radar system with  $M$  transmit antennas and  $N$  receiver antennas. Both are **ULA** with  $d = \frac{\lambda_c}{2}$  spacing between the antennas, where  $\lambda_c$  is the operating wavelength.

### 4.2.1 System Model

The complex baseband version of the received signal at continuous time  $t$  reflected from one point-like target is defined as [Fri12b, LS07]

$$\hat{\mathbf{y}}(t) = \alpha \mathbf{a}_r(\theta) \mathbf{a}_t(\theta)^T \mathbf{s}(t - \tau) + \mathbf{c}(t) \quad (4.1)$$

where  $\hat{\mathbf{y}}(t) \in \mathbb{C}^N$ . The transmit and receive arrays are characterized by the array manifolds:  $\mathbf{a}_t(\theta)$  and  $\mathbf{a}_r(\theta)$ , respectively, where  $\theta$  is the target direction. Hence,  $\mathbf{a}_r(\theta) = [1, e^{-jr \sin \theta}, \dots, e^{-jr(N-1) \sin \theta}]^T$  and  $\mathbf{a}_t(\theta)$  is defined similarly, where  $r = \frac{2\pi d}{\lambda_c}$ .  $\alpha \in \mathbb{C}$  is a deterministic unknown variable that accounts for the radar **RCS** and the two-way path loss following Swerling 0, while  $\tau$  is the time delay due to the target position with respect to the radar.  $\mathbf{c}(t) \in \mathbb{C}^N$  is the random disturbance vector, which is produced by clutter and white Gaussian noise.  $\mathbf{s}(t) \in \mathbb{C}^M$  is the narrowband transmit signal from all  $M$  antennas, generated as linear combination of independent orthonormal signals  $\mathbf{s}_{\text{orth}}(t) \in \mathbb{C}^M$ , where<sup>1</sup>

$$\mathbf{s}(t) = \mathbf{V} \mathbf{s}_{\text{orth}}(t), \quad (4.2)$$

<sup>1</sup>A narrow band model is assumed here, since the radar is in the search mode detecting point targets.

and  $\mathbf{V} = [\mathbf{v}_1, \dots, \mathbf{v}_M]^T \in \mathbb{C}^{M \times M}$ ,  $\mathbf{v}_m \in \mathbb{C}^M$  describe the beamforming weight matrix. Thus, the number of beamformers are equal to the number of transmit antennas. Moreover,  $\mathbf{V}$  is a square matrix which must obey the trace constraint  $\text{tr}\{\mathbf{V}\mathbf{V}^H\} = P_T$ , where  $P_T$  is the total transmit power. Furthermore, the beam pattern produced by the transmitted waveforms can be expressed as  $B(\theta) = \mathbf{a}_t^T(\theta)\mathbf{R}_V\mathbf{a}_t^*(\theta)$ , where  $\mathbf{R}_V = \mathbf{V}\mathbf{V}^H$  [LS07, Fri12b].

At the receiver, the received signal is processed by a linear matched filter  $\mathbf{s}_{\text{orth}}(t)$  tuned at delay  $\hat{\tau}$  considering a single transmitted pulse such that

$$\mathbf{Y}(\hat{\tau}) = \int_0^T \hat{\mathbf{y}}(t)\mathbf{s}_{\text{orth}}^H(t - \hat{\tau})dt. \quad (4.3)$$

Hence,

$$\mathbf{Y} = \alpha\mathbf{a}_r(\theta)\mathbf{a}_t^T(\theta)\mathbf{V} \int_0^T \mathbf{s}_{\text{orth}}(t - \tau)\mathbf{s}_{\text{orth}}^H(t - \hat{\tau})dt + \mathbf{C}, \quad (4.4)$$

where  $\mathbf{Y} \in \mathbb{C}^{N \times M}$  and  $\mathbf{C} = \int_0^T \mathbf{c}(t)\mathbf{s}_{\text{orth}}^H(t - \hat{\tau})dt$ . We assume that the matched filter is perfectly tuned to the target delay [Fri12b], hence  $\hat{\tau} = \tau$  and  $\int_0^T \mathbf{s}_{\text{orth}}(t - \tau)\mathbf{s}_{\text{orth}}^H(t - \hat{\tau})dt = \mathbf{I}$ . Rewriting eq. (4.1) to be in a vector form as

$$\mathbb{C}^{NM} \ni \mathbf{y} = \text{vec}(\mathbf{Y}) = \alpha\mathbf{h}(\theta) + \mathbf{c}, \quad (4.5)$$

where  $\text{vec}(\cdot)$  denotes the vectorization operator.

Moreover  $\mathbf{c} = \text{vec}(\mathbf{C})$  denotes the spatially colored disturbance vector. Then, utilizing the properties of the Kronecker product, the vector  $\mathbf{h}$  is defined as:

$$\mathbf{h}(\theta) = (\mathbf{V}^T\mathbf{a}_t(\theta)) \otimes \mathbf{a}_r(\theta). \quad (4.6)$$

It is worth mentioning that the sampling procedure (in fast-time, i.e. in range) is assumed to be done correctly respecting Nyquist theorem after the matched filter [Fri12b].

## 4.2.2 Disturbance Model

The statistical characterization of disturbance is a difficult task [BSW<sup>+</sup>19], generally, it is usually unknown. Despite the fact that various disturbance models have been adopted in radar literature, the dynamic nature of the clutter may limit their validity [FGGR17]. To avoid any model misspecification, robust approaches should be used.

Here, building upon the results obtained in [FSG<sup>+</sup>20], we adopt the following, very general, disturbance model:

*Assumption 1.* [FSG<sup>+</sup>20] *Let  $\{c_n: \forall n\}$  be the true and thus unknown disturbance process, which is a stationary discrete and circular complex valued process. It is only assumed that its autocorrelation function  $r_C[m] \triangleq \mathbb{E}\{c_n c_{n-m}^*\}$  has a polynomial decay.*

It should be noted that such an assumption is weak enough to encompass all the most practical disturbance models such as **auto-regressive (AR)**, **Auto regressive-moving average (ARMA)** or general correlated non-Gaussian models [FSG<sup>+</sup>20]. In order to detect the presence of targets embedded in unknown disturbance, the detection problem is formulated as a binary hypothesis testing problem described in the next subsection.

### 4.2.3 Detection Problem

It is assumed that the received signal in eq. (4.5) is processed by a bank of spatial filters, each tuned to a specific angle range. Such filter divides the radar field of view into separate  $B$  discrete angle bins, such that  $\{\theta_b; b = 1, \dots, B\}$ , and in total the system transmits  $K$  pulse waveforms,  $k \in \{1, \dots, K\}$ . Hence, after spatial filtering, for angle bin  $b$ , at pulse  $k$ , eq. (4.5) can be redefined as

$$\mathbf{y}_b^k = \alpha_b^k \mathbf{1}_b^k + \mathbf{c}_b^k. \quad (4.7)$$

The hypothesis testing problem for each angle bin  $b$  is cast as

$$\begin{aligned} H_0 : \mathbf{y}_b^k &= \mathbf{c}_b^k & k = 1, \dots, K \\ H_1 : \mathbf{y}_b^k &= \alpha_b^k \mathbf{1}_b^k + \mathbf{c}_b^k & k = 1, \dots, K. \end{aligned} \quad (4.8)$$

The null hypothesis  $H_0$  indicates that the cell under test contains only disturbance, i.e., clutter and noise, while the alternative  $H_1$  denotes single target detection. The entries of disturbance  $\mathbf{c}_b^k$  are sampled from a complex random process, satisfying the general Assumption 1, having unknown covariance matrix  $\Gamma_{b,k} = \mathbb{E}\{(\mathbf{c}_b^k)(\mathbf{c}_b^k)^H\}$ . The detection is performed per pulse, as the targets number, corresponding spatial angles and **SNR** can change from pulse  $k$  to another<sup>2</sup>. This also applies to the disturbance statistics, it can change in time and space. Hence, we assume a single snapshot scenario. In order to differentiate between  $H_0$  and  $H_1$  in eq. (4.8), a test statistic is required, where

$$\Lambda(\mathbf{y}_b^k) \underset{H_0}{\overset{H_1}{\geq}} \lambda. \quad (4.9)$$

Since in radar applications, it is of fundamental importance to control the  $P_{FA}$ , the threshold  $\lambda$  has to be chosen to satisfy the following

$$\Pr\{\Lambda(\mathbf{y}_b^k) > \lambda | H_0\} = \int_{\lambda}^{\infty} p_{\Lambda|H_0}(a|H_0) da = P_{FA}, \quad (4.10)$$

where  $p_{\Lambda|H_0}$  is the probability density function (pdf) of  $\Lambda(\mathbf{y}_b^k)$  under  $H_0$ . Usually, conventional model-based test statistics as **GLRT**, or *Wald test* are used to solve for eq. (4.9), yet they can not be directly applied here. This is due to the fact

<sup>2</sup>For simplicity, in the rest of the chapter, we will refer to  $k$  as time index related to pulse  $k$ .

that the functional form of the pdf of  $\mathbf{c}_b^k$  is unknown. Instead, we apply a robust Wald-type detector derived in [FSG+20], which requires the disturbance model only to satisfy Assumption 1. This detector is asymptotically distributed, (i.e.,  $N_v \rightarrow \infty$ ) as chi-squared  $\chi_2^2$  random variable under both  $H_0$  and  $H_1$  (see Appendix A.1).

This Wald-type test requires the availability of an asymptotically Normal estimator of  $\alpha_b^k$  which is  $\sqrt{N_v}$  consistent. As shown in [FSG+20], the following estimator satisfies the above-mentioned requirements:

$$\hat{\alpha}_b^k = \frac{(\mathbf{h}_b^k)^H \mathbf{y}_b^k}{\|\mathbf{h}_b^k\|^2}. \quad (4.11)$$

Consequently, a robust Wald-type test for each angle bin  $b$ , is given by

$$\Lambda_{b,\text{RW}}^k = \frac{2|(\mathbf{h}_b^k)^H \mathbf{y}_b^k|^2}{(\mathbf{h}_b^k)^H \hat{\Gamma}_{b,k} \mathbf{h}_b^k}, \quad (4.12)$$

where  $\hat{\Gamma}_{b,k}$  is the estimate of the unknown  $\Gamma_{b,k}$ . Further details about the calculation of  $\hat{\Gamma}_{b,k}$  and the asymptotic distribution of  $\Lambda_{b,\text{RW}}^k$  are provided in Appendix A.

The threshold  $\lambda$  which satisfies eq. (4.10) regardless the disturbance distribution, can be expressed as [FSG+20]:

$$\lambda = H_{\chi_2^2}^{-1}(1 - P_{\text{FA}}), \quad (4.13)$$

in which  $H_{\chi_2^2}^{-1}(\lambda)$  is the inverse of the CDF function  $H_{\chi_2^2}(\lambda) = \int_{-\infty}^{\lambda} p_{\Lambda_{b,\text{RW}}^k}(a|H_0) da$ .

Eq. (4.13) guarantees the CFAR property for the robust Wald-type detector in eq. (4.12). However, the CFARness is only one aspect of a radar detection scheme. The second primary goal is to have good detection performance in terms of  $P_D$ . In the next section, we propose a RL based algorithm that is able to enhance the detection while maintaining the CFAR property.

## 4.3 RL-Based Massive MIMO CR

In this section, a detailed description of the proposed RL-based multi-target detection algorithm is provided. For this, a MMIMO CR is adopted in our system, where a CR continuously senses the environment and takes decisions by adjusting its transmitted waveform as previously explained in 2.4. In this section, we propose an intelligent methodology for the CR to take its decisions, using RL. In more detail, we will map the aforementioned RL tools defined previously in section 2.5.2 into our MMIMO CR setup.

### 4.3.1 SARSA Algorithm and Target Detection

The acronym *state-action-reward-state-action* (SARSA) is derived from the *state-action-reward-state-action* sequence to update the values of the  $Q$ -function [PM17].



**SARSA** is an on-policy RL algorithm, which evaluates and improves the same policy that is being used for action selection. In contrast, off-policy algorithms, evaluate and improve a policy different from the one used for action selection. **SARSA** falls under the category of model-free reinforcement learning algorithms because it does not require a model of the environment.

In our **MIMO** radar problem, the agent has to maintain a state-action matrix where  $\mathbf{Q} \in \mathbb{R}^{(L_{\max}+1) \times (L_{\max}+1)}$  of elements  $Q(s_k, a_k)$ <sup>3</sup>, where  $L_{\max}$  is the maximum number of targets that any **MIMO** radar can identify. This matrix is initialized with 0, afterwards based on the execution of a certain action, the agent shifts from one state to another then updates the  $Q$ -function according to the following update rule [SB18]

$$Q(s_k, a_k) \leftarrow Q(s_k, a_k) + \xi (r_{k+1} + \gamma Q(s_{k+1}, a_{k+1}) - Q(s_k, a_k)) \quad (4.14)$$

The learning rate  $\xi \in [0, 1]$  is used to control how much the recent experiences override the old ones. For instance, as  $\xi$  increases, the influence of the recent experiences on the  $Q$  function increases. Meanwhile, the discount factor  $\gamma$  determines the impact of the future rewards. For example,  $\gamma = 0$  forces the agent to exploit only current rewards, while when  $\gamma = 1$ , this makes the agent takes into account future long-term high rewards. In the following subsections, the **SARSA** terms are explained according to the radar definitions.

### 4.3.2 The set of States

To define the state space  $\mathcal{S}$ , the statistic  $\Lambda_{b, \text{RW}}^k$  from eq. (4.12) is utilized. If  $\Lambda_{b, \text{RW}}^k$  is greater than the defined threshold  $\lambda$  from eq. (4.13) for the angle bin  $b$  at pulse  $k$ , a new statistic  $\bar{\Lambda}_b^k$  is set to 1, otherwise it is 0:

$$\bar{\Lambda}_b^k = \begin{cases} 1 & \Lambda_{b, \text{RW}}^k > \lambda \\ 0 & \text{otherwise.} \end{cases} \quad (4.15)$$

Hence,  $\bar{\Lambda}_b^k$  indicates whether or not it is likely for the angle bin  $b$  to contain a target. Hence state  $s_k$  is then defined as the total number of angle bins where the targets could be located at pulse  $k$ :

$$s_k = \sum_{b=1}^B \bar{\Lambda}_b^k. \quad (4.16)$$

Hence, the set of possible states can be written as  $\mathcal{S} = \{0, \dots, L_{\max}\}$ .

### 4.3.3 The Set of Actions

The **MMIMO** radar, i.e., the agent, starts by initially transmitting an orthonormal waveform at  $k = 0$ , by setting the beamforming matrix  $\mathbf{V}_k$  given in eq. (4.6) to be

<sup>3</sup>Here  $k$  represents time index, so  $s_k$  is the state at time index  $k$ .

equal to the identity matrix, i.e.,  $\mathbf{V}_k = \mathbf{I}$ . We assume a discrete radar field of view divided into  $b$  angle cells. Hence,  $\mathbf{y}_b^k$  is the received signal of single snapshot at angle bin  $b$ .

The number of targets  $s_{k+1}$  is calculated based on eq. (4.16) which gives an indication of the status of the environment. Based on this observation, the agent takes a certain action. An action can be defined as two tasks. The first task is the process of selecting the candidate angle bins which most likely contain the targets based on the current environmental state. The second task is the optimization of the beamforming matrix,  $\mathbf{V}$ , to focus the transmit power towards those angle bins. Hence, the cardinality of the set of actions  $\mathcal{A}$  can be set as  $L_{\max}$ , which is the maximum number of targets that the radar can detect. Consequently, an action can be defined as  $a_k \in \mathcal{A} = \{\Theta_i | i \in \{0, 1, \dots, L_{\max}\}\}$ . Specifically, the agent has to identify  $\Theta_i = \{\hat{\theta}_1, \dots, \hat{\theta}_i\}$  which are the  $i$  angle bins that most likely contain targets. Here  $\hat{\theta}$  is the estimated angle bin which contains a target, while  $\mathcal{A} = \{\Theta_0, \Theta_1, \dots, \Theta_{L_{\max}}\}$  is the set of all possible angle bins.

In order to build the set  $\Theta_i$ , the highest  $i$  values of  $\Lambda_{b,\text{RW}}^k$ , defined in eq. (4.12), are chosen. In other words, we rank all the angle bins based on their  $\Lambda_{b,\text{RW}}^k$ , and the best  $i$  angles are chosen. With the completion of the last step, the agent is now ready to optimize the beamformers towards the chosen angles.

The weighting matrix  $\mathbf{V}$  has to be optimized, in order to synthesize the corresponding beam pattern. Therefore, the transmitted power is concentrated towards those angle bins in  $\Theta_i$ , which may contain targets as shown in Fig 4.1.

This is done by maximizing the minimum of the beam pattern  $B(\hat{\theta}_j) = \mathbf{a}_r^T(\hat{\theta}_j)\mathbf{R}_V\mathbf{a}_r^*(\hat{\theta}_j)$ , with  $\mathbf{R}_V = \mathbf{V}\mathbf{V}^H$ ,  $\hat{\theta}_j \in \Theta_i$  and under the power constraint  $\text{tr}(\mathbf{R}_V) = P_T$ . The resulting optimization problem is stated as follows:

$$\begin{aligned} \max_{\mathbf{V}} \min_{j \in \mathcal{T}_i} \{ \mathbf{a}_r^T(\hat{\theta}_j)\mathbf{V}\mathbf{V}^H\mathbf{a}_r^*(\hat{\theta}_j) \} \\ \text{s.t. } \text{tr}(\mathbf{V}\mathbf{V}^H) = P_T, \end{aligned} \quad (4.17)$$

where  $\mathcal{T}_i = \{1, \dots, i\}$ . Details of the optimization problem and its solution are provided in section 4.4.

### 4.3.4 The Reward

The reward defines the goal of the RL problem, hence the radar agent's sole objective is to maximize the total cumulative reward function in the long run [SB18]. Consequently, it defines how the agent should behave, as the agent learns what are the good and bad actions. In our case, the goal is to detect all the targets even those masked within the disturbance. This is achieved through specific actions, i.e., optimizing the beampattern. Therefore, the reward is expressed in terms of the estimated  $\hat{P}_{D_b}^k$  as

$$\hat{P}_{D_b}^k = Q_1 \left( \sqrt{\hat{\zeta}_b^k}, \sqrt{\lambda} \right), \quad (4.18)$$

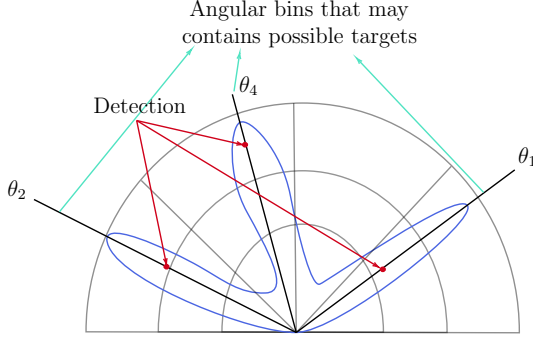


Figure 4.1: Focusing the beampattern towards possible detections

$$\hat{\zeta}_b^k = 2|\hat{\alpha}_b^k|^2 \frac{\|\mathbf{h}_b^k\|^4}{(\mathbf{h}_b^k)^H \hat{\mathbf{T}}_{b,k} \mathbf{h}_b^k}, \quad (4.19)$$

where  $Q_1(\cdot, \cdot)$  is the first order *Marcum Q function* [Nut74],  $\hat{\alpha}_b^k$  is defined in eq. (4.11) and  $\hat{\mathbf{T}}_{b,k}$  is defined as in eq. (A.1). The theoretical derivation of eq. (4.18) and eq. (4.19) can be found in [FSG<sup>+</sup>20]. In fact, the reward is chosen to be a function of eq. (4.18) as it provides accurate detection in an asymptotic regime when the number of spatial virtual antenna channels  $N_v$  grows unbounded, i.e.,  $N_v \rightarrow \infty$ . Furthermore, the robust Wald-type detection in eq. (4.15) satisfies the **CFAR** requirement even in a single-snapshot scenario.

The reward function is composed of two parts: negative and positive rewards. The negative reward can be considered as a penalty for the agent in case of false detections. Hence, the positive reward is the summation of  $\hat{P}_{D_b}^k$  for the angle cells defined in  $i$ , while the negative reward is the summation of  $\hat{P}_{D_b}^k$  for the rest of the cells, which is likely not to contain any target. The best case scenario occurs when there is a target in every bin such that  $s_k = B$ , as this means that the decision statistic  $\Lambda_{b,\text{RW}}^k > \lambda, \forall b$  (i.e.,  $b$  targets are detected).

The reward for each time step  $k$  will be defined as:

$$r_{k+1} = \sum_{b=1}^{s_k} \hat{P}_{D_b}^k - \sum_{j=1}^{B-s_k} \hat{P}_{D_j}^k, \quad (4.20)$$

where  $\hat{P}_{D_b}^k$  is the probability of detection as in eq. (4.18) calculated for target  $b$  at  $\theta_b^k$  after taking observing state  $s_k$  and taking action  $a_k$ . The reward does not require any ground truth data for training, it is updated in every time step using only the feedback it gets from the environment. In this case, this feedback is the estimated detection probabilities in eq. (4.18), which is calculated online from the environment for every angle bin. Thus, the algorithm proposed depends completely on an online learning mechanism.

### 4.3.5 Policy

In order to determine which action the agent has to take at each step  $k$ , an action policy must be defined. This policy controls the size of  $\Theta_i$  (i.e.,  $i$ ) which defines the action  $a_k$ . In our algorithm,  $i$  is defined based on the  $\epsilon$  greedy policy, which is a simple policy balancing exploration and exploitation as previously mentioned in section 2.5.2. In fact, the agent could follow the same actions which were tried in the past and proved to maximize the reward (i.e., exploitation). However, the agent is required also to acquire new knowledge through discovering new actions (i.e., exploration). In the  $\epsilon$  greedy policy, the variable  $\epsilon$  refers to the probability of exploring new actions randomly. In more details, the optimal action  $a_{\text{opt}} \triangleq \arg \max_{a \in \mathcal{A}} \mathbf{Q}(s_{k+1}, a)$  is taken with a probability of  $1 - \epsilon$ , while another random action  $a_{\text{rnd}}$  (excluding  $a_{\text{opt}}$ ) is chosen with a probability of  $\epsilon$  such that

$$a_{k+1} = \begin{cases} a_{\text{opt}} & \text{with prob. } 1 - \epsilon \\ a_{\text{rnd}} & \text{with prob. } \epsilon. \end{cases} \quad (4.21)$$

This implies that, if we set  $\epsilon = 0$ , the agent will not explore anything and would always choose  $a_{\text{opt}}$ . Whereas, if we set  $\epsilon = 1$ , the action is selected randomly, and the agent would not exploit the information previously learned and saved in the state-action matrix  $\mathbf{Q}$ . In the following example, we further clarify how the matrix  $\mathbf{Q}$  is filled and how an action is defined.

*Example 3.* Suppose that the maximum number of targets that the radar can detect is set to  $L_{\text{max}} = 3$ , thus  $\mathbf{Q} \in \mathbb{R}^{4 \times 4}$ . Here, there are 4 possible discrete states and actions values, where<sup>4</sup>  $\mathcal{A} = \{a^0, a^1, a^2, a^3\}$  and  $\mathcal{S} = \{s^0, s^1, s^2, s^3\}$ . Therefore, according to the state and actions definitions explained in 4.3.2 and 4.3.3, then  $\mathcal{S} = \{0, 1, 2, 3\}$  and  $\mathcal{A} = \{\Theta_0, \Theta_1, \Theta_2, \Theta_3\}$  respectively. Initially, at  $k = 0$ , the matrix is initialized with zeros. Then, the agent would start filling its entries  $Q(s_k, a_k)$  using eq. (4.14) in every time step  $k$ . In the first iteration, the following update is rule is used

$$Q(s_0, a_0) \leftarrow Q(s_0, a_0) + \xi(r_1 + \gamma Q(s_1, a_1) - Q(s_0, a_0)) \quad (4.22)$$

where  $Q(s_1, a_1)$  would be initially zero and  $r_1$  is calculated as in eq. (4.20). Thus, at  $k = 0$ , if  $s_0 = s^0 = 0$  and  $a_0 = a^0 = \Theta_0$ , the value in  $Q(s^0, a^0)$  would be updated. This also means that there are no targets in the radar scene. Then, this matrix would keep updating its entries for every  $k$ . To understand how the action is taken, let us observe the matrix at  $k = 17$  for instance, the state  $s_{k+1} = s^2 = 2$ , which indicates that there are only two angle bins that most likely contain the target based on (4.16). In addition, the  $\epsilon$  greedy algorithm chose  $a_{k+1} = a_{\text{opt}}$  as per eq. (4.21) and the  $\mathbf{Q}$  matrix at  $k = 17$  is given by Tab. 4.1.

<sup>4</sup>Please note that  $s^l$  with superscript denotes the value of the state, while  $s_k$  with subscript denotes the state at time  $k$  (i.e.,  $s_0 = s^0$  means the state at  $k = 0$  has the value of  $s^0$ ),  $a^l$  and  $a_k$  are denoted similarly.

States \ Actions	$a^0$	$a^1$	$a^2$	$a^3$
$s^0$	0.4508	0	0	0
$s^1$	1.4376	2.2586	1.5617	2.4848
$s^2$	0.5118	1.5951	2.5540	1.4495
$s^3$	0	0	1.5345	0

Table 4.1:  $\mathbf{Q}$  matrix at  $k = 17$ 

In the first few time steps,  $a_{\text{opt}}$  might cause miss-detection. This can be seen in the case of  $k = 17$ , where if  $s_{k+1} = 3$ , then the next action  $a_{k+1} = a_{\text{opt}} = a^2$  will be chosen with probability  $1 - \epsilon$ . However, as the  $\mathbf{Q}$  matrix is updated every time step based on the new evaluated reward, the probability of miss detection decreases over time. Hence, in the final time step  $k = 50$  as shown in Tab. 4.2, if  $s_{k+1} = 3$ , then the next action  $a_{k+1} = a_{\text{opt}} = a^3$ . It is worth mentioning that the  $\mathbf{Q}$  matrix does not require any training since it learns by experience from the environment in every time step.

States \ Actions	$a^0$	$a^1$	$a^2$	$a^3$
$s^0$	0.4508	0	0	0
$s^1$	4.2332	2.0142	4.3149	5.2843
$s^2$	0.5118	3.4302	4.4225	4.7489
$s^3$	1.8499	0	1.5345	2.3170

Table 4.2:  $\mathbf{Q}$  matrix at time  $k = 50$ 

In the following algorithm, the steps of our **MMIMO** radar **SARSA** are summarized.

## 4.4 Optimization Problem

In this section, a solution for the beamforming optimization problem in eq. (4.17) is discussed. As a matter of fact, **SDP** relaxation is a widely used method to solve this problem [WZLT18, WFGG18, LMS<sup>+</sup>10], however, **SDP** complexity increases with the size of  $\mathbf{V}$ , hence using **SDP** for the **MMIMO** application previously described would not be realistic. Moreover, **SDP** involves a relaxation of the original problem, and getting a feasible solution requires a heuristic randomization process. The high

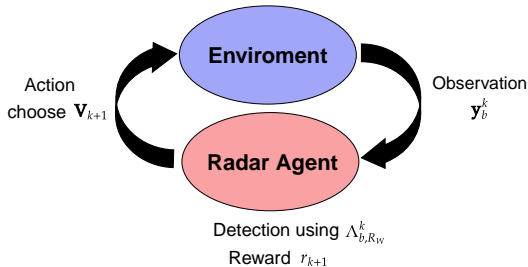


Figure 4.2: RL-CR cycle

complexity of the solution described in [LAA14, FS08, WZLT18] to the optimization problem is due to its two-steps structure: in the first step,  $\mathbf{R}_V$  is synthesized; then in the second step, the beamformer matrix  $\mathbf{V}$  is generated from  $\mathbf{R}_V$ .

To reduce the computational complexity, we propose another approach based on **inner convex approximations (ICA)** [SFL<sup>+</sup>16]. This allows finding  $\mathbf{V}$ , in an iterative fashion. Our approach, as opposed to **SDP**, guarantees to obtain a **KKT** point of the original problem and avoids rank relaxation issues of the **SDP** approach. The authors in [SFL<sup>+</sup>16] used **ICA** to solve for the rate capacity expression in a wireless communication context, however, we adapt and modify their optimization approach to fit our radar problem. To this end, we write the optimization problem, eq. (4.17) as follows

$$\max_{\mathbf{V}, \zeta} \zeta \quad (4.23)$$

$$\text{s. t.} \quad \zeta \geq 0, \quad \text{tr}(\mathbf{V}^H \mathbf{V}) = P_T \quad (4.24)$$

$$\zeta - f_j(\mathbf{V}) \leq 0 \quad \forall j \in \mathcal{T}_i. \quad (4.25)$$

Here the function  $f_j(\mathbf{V})$  is defined as  $f_j(\mathbf{V}) \triangleq \mathbf{a}_r^T(\hat{\theta}_j) \mathbf{V} \mathbf{V}^H \mathbf{a}_r^*(\hat{\theta}_j)$ . Problem eq. (4.23) is non-convex and difficult to solve due to constraints in eq. (4.25) which are not convex. To overcome this difficulty, we propose to iteratively approximate the non-convex feasible set from inside with a convex feasible set by approximating the function  $f_j(\mathbf{V})$ . The approximation of the function  $f_j(\mathbf{V})$  writes

$$\tilde{f}_j(\mathbf{V}; \tilde{\mathbf{V}}) = f_j(\tilde{\mathbf{V}}) + \langle \nabla_{\mathbf{V}} f_j(\tilde{\mathbf{V}}), \mathbf{V} - \tilde{\mathbf{V}} \rangle, \quad (4.26)$$

where  $\nabla_{\mathbf{V}} f_j(\tilde{\mathbf{V}})$  is the gradient of function  $f_j(\mathbf{V})$  with respect to  $\mathbf{V}$  computed at the fixed point  $\tilde{\mathbf{V}}$  and  $\langle \mathbf{A}, \mathbf{B} \rangle = \Re\{\text{tr}(\mathbf{A}^H \mathbf{B})\}$ . Obviously, using this approach we get an inner convex approximation of the original non-convex feasible set. To see this, note that the function  $f_j(\mathbf{V})$  is a quadratic convex function in  $\mathbf{V}$  which results in its approximation being its under-estimator. Hence, we have the following relation

$$\zeta - f_j(\mathbf{V}) \leq \zeta - \tilde{f}_j(\mathbf{V}; \tilde{\mathbf{V}}) \leq 0 \quad \forall j \in \mathcal{T}_i \quad (4.27)$$

**Algorithm 3 SARSA**


---

Initialize  $\mathbf{Q} = \mathbf{0}_{L_{\max}}$ 

Initialize state  $s_0 = 1$ , action  $a_0 = 1$ ,  $K = 50$  and  $\mathbf{V}_k = \mathbf{I}$ 
**repeat** for each time step  $k$ :

Take action  $a_k$  by transmitting waveform eq. (4.2) using  $\mathbf{V}_k$ 

Acquire the received signal  $\mathbf{y}_b^k, \forall b = 1, \dots, B$ 

Calculate  $s_{k+1}$  from eq. (4.16)

Evaluate the reward  $r_{k+1}$  as in eq. (4.20)

Choose action  $a_{k+1}$  as eq. (4.21), identify  $\Theta_i$  and  $\mathcal{T}_i$ 

$$Q(s_k, a_k) \leftarrow Q(s_k, a_k) + \xi(r_{k+1} + \gamma Q(s_{k+1}, a_{k+1}) - Q(s_k, a_k))$$

 $s_k \leftarrow s_{k+1}; a_k \leftarrow a_{k+1}$ 
**if**  $s_{k+1} \neq 0$  **then**

Solve for  $\mathbf{V}_{k+1}$  in eq. (4.17) using algorithm eq. (4)

**else**
 $\mathbf{V}_k = \mathbf{I}$ 
**end if**
**until** Observation time ends

---

This inner convex approximation approach iteratively enhances the lower-bound on the convex function  $f_j(\mathbf{V})$  and eventually converges to a **KKT** point of problem eq. (4.23). Let  $m$  be the iteration index and  $\tilde{\mathbf{V}}^m$  be the beamforming matrix at iteration  $m$ . The successive inner convex approximation approach is based on solving the following problem iteratively until convergence.

$$\max_{\mathbf{V}, \zeta} \zeta \tag{4.28}$$

$$s. t. \quad \zeta \geq 0, \quad \text{tr}(\mathbf{V}^H \mathbf{V}) = P_T \tag{4.29}$$

$$\zeta - \tilde{f}_j(\mathbf{V}; \tilde{\mathbf{V}}^m) \leq 0, \forall j \in \mathcal{T}_i, \tag{4.30}$$

Problem eq. (4.28) is convex and the optimal solution can be found efficiently with an interior-point solver such as in [GB14]. The algorithm for finding the **KKT** point of problem eq. (4.23) is listed in algorithm 4.

*Proposition 1.* Algorithm 4 guarantees convergence to a **KKT** point of the non-convex problem eq. (4.17).

*Proof.* Please refer to Appendix A.2.

## 4.5 Numerical Analysis

In this section, the cognitive **MMIMO** radar using the **SARSA** algorithm is simulated, where the agent is in a continuous learning mode of the surrounding environment,

**Algorithm 4** Iterative Inner Convex Approximation Algorithm

---

Set  $m = 0$  and initialize  $\tilde{\mathbf{V}}^0$  such that  $\text{tr}((\tilde{\mathbf{V}}^0)^H \tilde{\mathbf{V}}^0) = P_T$ .

**repeat**

Solve problem eq. (4.28) approximated around point  $\tilde{\mathbf{V}}^m$ .

Set  $\tilde{\mathbf{V}}^{m+1}$  as the optimal solution of problem eq. (4.28)

$m \leftarrow m + 1$

**until** convergence

---

taking decisions while learning. The performance is averaged over  $10^4$  Monte Carlo runs. Tab. 4.3 summarizes the values of the parameters for the SARSA algorithm.

Parameter	Value
Learning rate $\alpha$	0.8
Exploration rate $\epsilon_0$	0.5
Discount factor $\gamma$	0.8
Number of States $\mathcal{S}$	11
Number of actions $\mathcal{A}$	11
Time steps $K$	50
Initial state $s_0$	1

Table 4.3: Reinforcement learning parameters

**4.5.1 Simulation Setup**

In our simulations, the angle grid is divided into  $B = 20$  angle bins. The angular locations would be represented in terms of the spatial frequency  $\nu$ , which is defined as

$$\nu \triangleq \frac{df_c}{c} \sin(\theta) \quad (4.31)$$

where  $f_c$  is the carrier frequency and  $c$  is the speed of light. Hence, the steering vector for the transmit or receive can be redefined in terms of  $\nu$

$$\mathbf{a}_r(\theta) = [1, e^{j2\pi\nu}, \dots, e^{j2\pi(N-1)\nu}]^T, \quad (4.32)$$

Furthermore, the angle grid can be expressed as a spatial frequency grid where  $\nu = [-0.5 : 0.45]$ . We further assume the existence of four targets at spatial frequency locations  $\nu = \{-0.2, 0, 0.2, 0.3\} \subset \nu$ , with SNR =  $[-5\text{dB}, -8\text{dB}, -10\text{dB}, -9\text{dB}]$  respectively.



### 4.5.2 Disturbance Model

The disturbance model is chosen to mask the target angles, where the disturbance power is spread all over the spatial frequency range. Hence, the potential of our **RL** cognitive radar algorithm can be analyzed in such a harsh environment. The disturbance entries of  $\mathbf{c}_b^k$  is generated according to the model of circular SOS AR ( $p$ ) [FSG+20] as

$$c_n = \sum_{i=1}^p \rho_i c_{n-i} + w_n, \quad n \in (-\infty, \infty), \quad (4.33)$$

where  $p = 6$ , driven by identically independent (i.i.d.),  $t$ -distributed innovations  $w_n$  whose pdf  $p_w$  is defined as [FGG16, FSG+20] :

$$p_w(w_n) = \frac{\mu}{\sigma_w^2} \left(\frac{\mu}{\mathcal{K}}\right)^\mu \left(\frac{\mu}{\mathcal{K}} + \frac{|w_n|^2}{\sigma_w^2}\right)^{-(\mu+1)}. \quad (4.34)$$

$\mu \in (1, \infty)$  is the shape parameter controlling the non-Gaussianity of  $w_n$ . Specifically, if  $\mu \rightarrow 1$ , then  $p_w$  is a heavy-tailed pdf with highly non-Gaussian behavior. However, the pdf becomes Gaussian if  $\mu \rightarrow \infty$ . The scale parameter is defined by  $\mathcal{K} = \mu / (\sigma_w^2 (\mu - 1))$ . We set in our simulations  $\mu = 2$  and  $\sigma_w^2 = 1$ . Hence, the normalized PSD of the disturbance is given by [FSG+20]

$$S(\nu) \triangleq \sigma_w^2 \left| 1 - \sum_{n=1}^p \rho_n e^{j2\pi\nu} \right|^{-2}, \quad p = 6. \quad (4.35)$$

The coefficient vector  $\boldsymbol{\rho}$  is defined as

$$\boldsymbol{\rho} = [0.5e^{-j2\pi 0.4}, 0.6e^{-j2\pi 0.2}, 0.7e^{-j2\pi 0}, 0.4e^{j2\pi 0.1}, 0.5e^{j2\pi 0.3}, 0.6e^{j2\pi 0.35}]^T.$$

The disturbance PSD is shown in Fig. 4.3, where the target angles are marked in red dashed lines. Note that the disturbance PSD has multiple peaks.

### 4.5.3 Study Case 1 : Stationary Environment

To exploit the benefits of **RL**, we compared the the proposed **RL**-based beamformer against two types of beamforming,

- omnidirectional equal power allocation with no **RL**. Here, the antennas emit orthonormal waveforms and the power is divided equally across all antennas
- adaptive beamforming represented by Alg (2) with no **RL**.

It is assumed that the total power  $P_T = 1$  and for fair comparison the same detector  $\Lambda_{b, \text{RW}}^k$  is used in all cases according to eq. (4.15) in each time step. In this set of simulations, the environment is assumed to be temporally stationary. The difference in behavior of the **MMIMO** radar with/without **RL** is analyzed. The results were averaged over  $10^4$  Monte Carlo runs.

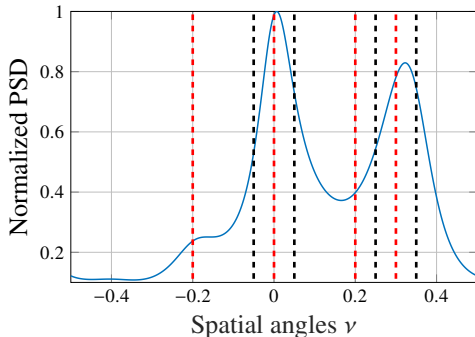


Figure 4.3: Disturbance PSD along with targets angles locations (red dashed lines for study case 1 and black ones for study case 2)

### Scenario 1: $P_D$ across time

In this scenario, the performance of the algorithm is analyzed for a **MMIMO** regime where  $N_v = MN = 10^4$  and  $P_{FA} = 10^{-4}$ . Fig. 4.4 depicts the difference between our proposed algorithm and omnidirectional **MMIMO**. In order to obtain those figures, we calculated the threshold in eq. (4.15) within each time step, then the average is taken across all Monte Carlo runs. Fig. 4.4a demonstrates better detection performance for all targets even the ones with low SNR. It can be shown that the algorithm learns across time: in the first ten time steps, the agent is learning the disturbance, enhancing its experience as time passes. Conversely, in the omnidirectional approach in Fig. 4.4b the targets with lower SNR are mostly masked under the disturbance peaks, as in the case of  $\nu = 0$  and  $\nu = 0.3$ . To measure the convergence of our algorithm, we report the immediate reward function as in eq. (4.20) in Fig. 4.5. In fact, as depicted in the figure, the reward converges after 20 time steps. This result is consistent with Fig. 4.4a, where the agent performance becomes very good after  $k = 20$ . However, it is worth mentioning, that the convergence of the reward depends heavily on the environment and the number of targets in the scene with respect to the size of the  $Q$  matrix. To verify this claim, we further increased the number of targets to 9 while keeping the same size of the  $Q$  matrix. It can be shown from Fig. 4.6, that, in this case, the convergence is reached after 150 time steps  $k = 150$ . This is due to the fact that the  $Q$  matrix becomes less sparse as the number of targets increases w.r.t the matrix size.

### Scenario 2: $P_D$ vs $N_v$

In this scenario, we simulated the  $\hat{P}_D$  estimated from the closed-form expression in eq. (4.18), averaged over time for each target, as a function of the spatial virtual

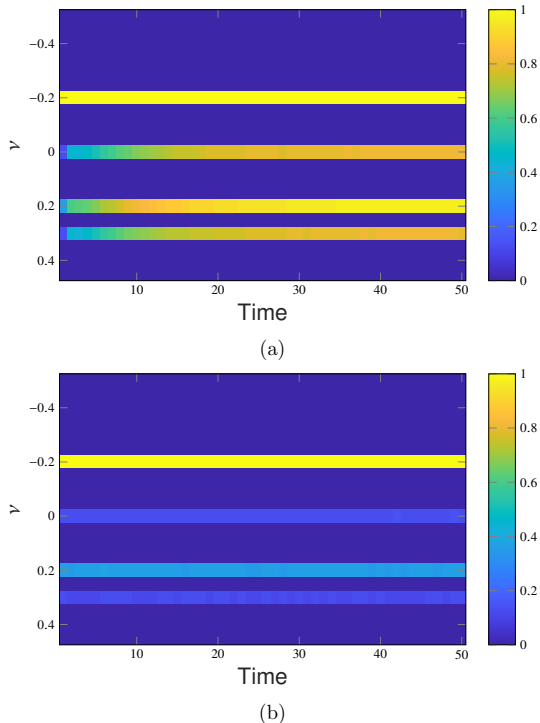


Figure 4.4: Detection performance of (a) proposed RL beamforming vs. (b) omnidirectional with equal power allocation under  $P_{\text{FA}} = 10^{-4}$  and  $N_v = MN = 10^4$ .

antenna channels  $N_v$ . Here, the number of transmit and receive antennas are  $M = N = [10, 12, 16, 21, 27, 35, 46, 59, 77, 100]$ .

The results in Fig. 4.7 show that as  $N_v$  increases, the  $\hat{P}_D$  increases for all the targets. However, the suggested algorithm provides better performance than the omnidirectional and adaptive case for all targets except  $\nu = -0.2$  as in Fig. 4.7a. In this case, the adaptive algorithm shows the best performance. This is due to the high SNR of this target, in addition, it lies within low disturbance. The low  $\hat{P}_D$  as  $N_v \rightarrow 10^3$  shown in Fig. 4.7b, 4.7c and 4.7d, is due to the harsh operating conditions, since  $P_T = 1$  and the nominal  $P_{\text{FA}} = 10^{-4}$ . Furthermore, the corresponding targets are located within heavy disturbance.

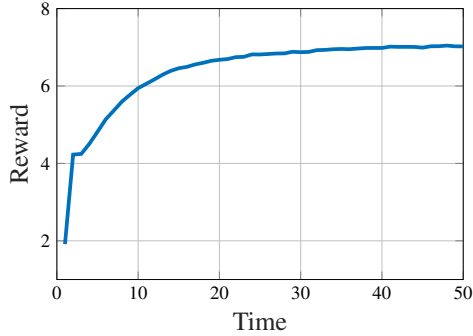


Figure 4.5: Reward calculated as in eq. (4.20) for RL-based beamformer with  $P_{\text{FA}} = 10^{-4}$  and  $N_v = MN = 10^4$ .

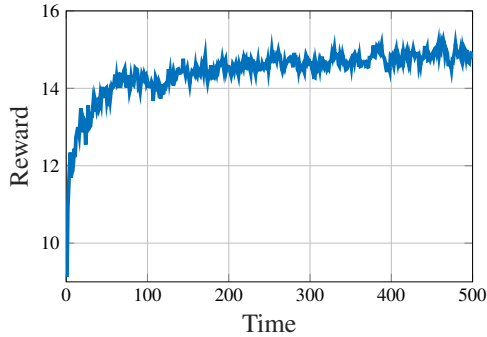


Figure 4.6: Reward behavior in static environment for 9 targets.

### Scenario 3: $P_{\text{D}}$ vs $P_{\text{FA}}$

In this scenario, the receiver operating characteristics (ROC) curve is simulated across a range of  $P_{\text{FA}} = [10^{-5}, 10^{-4}, 10^{-3}, 10^{-2}, 1]$  with  $N_v = 10^4$ . As shown in Fig. 4.8, mainly the potential of the RL-based cognitive MMIMO radar is shown in low  $P_{\text{FA}}$  regimes. As a matter of fact, most practical radar applications have to maintain preassigned low  $P_{\text{FA}}$  values. Hence, we conclude that our proposed algorithm is more suitable for those practical systems in general. Meanwhile, it is notably visible from Fig. 4.8a, that the  $\hat{P}_{\text{D}}$  is 1 across all  $P_{\text{FA}}$ . This is due to the fact that this target has relatively high SNR and is located within relatively low disturbance PSD. This means that omnidirectional and adaptive systems can perform well in those conditions. Meanwhile, the  $\hat{P}_{\text{D}}$  for targets with low SNR is much higher for the

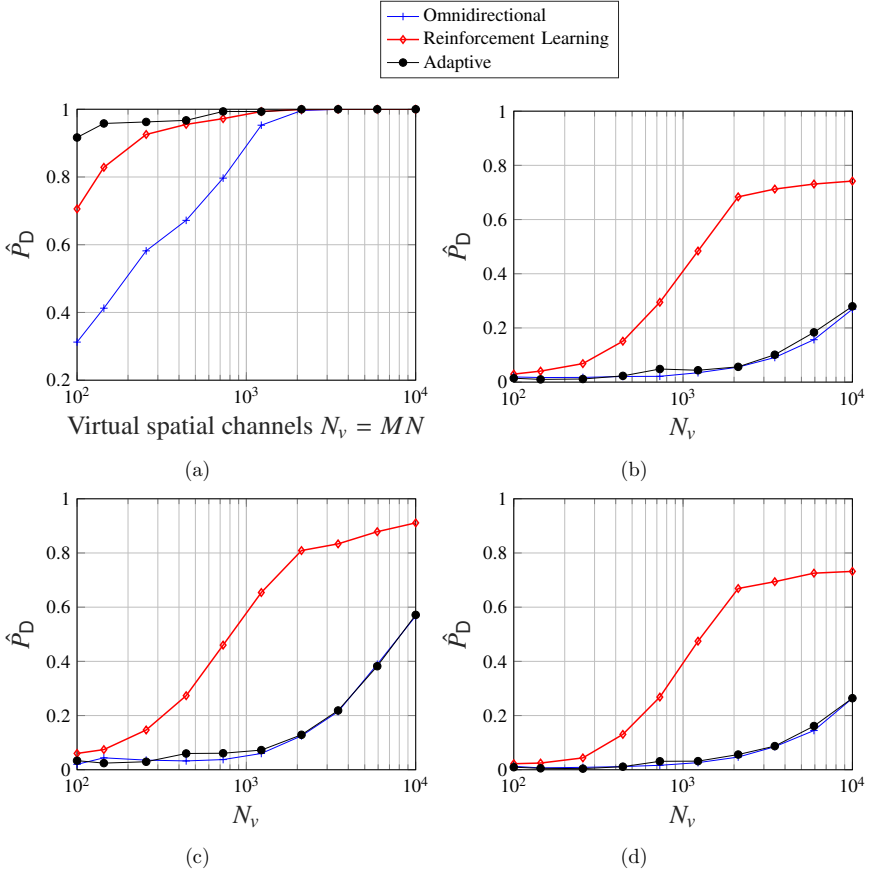


Figure 4.7:  $\hat{P}_D$  using RL and alternative approaches of existing targets across different virtual antenna array size with  $P_{FA} = 10^{-4}$  a)  $\nu = -0.2$  with SNR = -5 dB b)  $\nu = 0$  with SNR = -8 dB c)  $\nu = 0.2$  with SNR = -10 dB d)  $\nu = 0.3$  with SNR = -9 dB.

proposed algorithm compared to the omnidirectional and adaptive solutions, i.e.,  $\nu = 0$  in Fig. 4.8b,  $\nu = 0.2$  in Fig. 4.8c. For both algorithms,  $\hat{P}_D$  approaches 1 for as the  $P_{FA} \rightarrow 1$ .

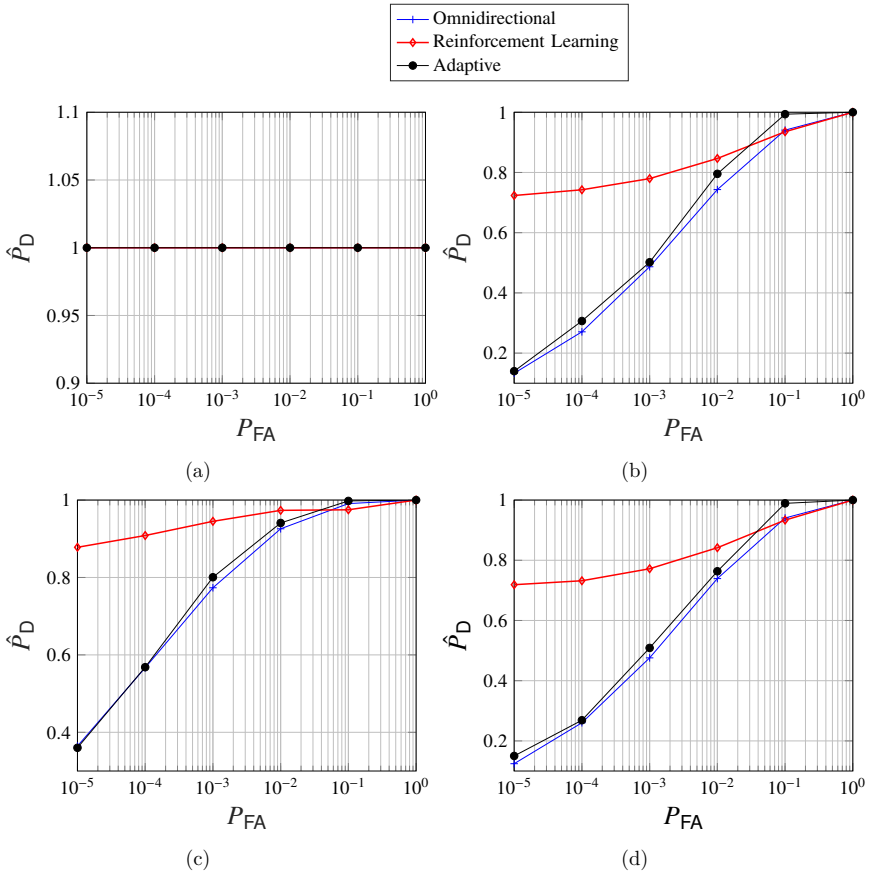


Figure 4.8:  $\hat{P}_D$  using RL and alternative approaches of existing targets across different  $P_{FA}$  with  $N_v = 10^4$  a)  $\nu = -0.2$  with SNR = -5 dB b)  $\nu = 0$  with SNR = -8 dB c)  $\nu = 0.2$  with SNR = -10 dB d)  $\nu = 0.3$  with SNR = -9 dB.

#### Scenario 4: Narrow-band clutter

In this simulation, we consider a narrow-band clutter model with a strong peak at  $\nu = 0$  as in Fig. 4.9. In more detail, for such a scenario, there are two possible cases, the first case is when there is clutter imposing very strong peaks at certain angles, while there are no targets present at those angles. In such a case, both the

omnidirectional and **RL** beamformer would foresee such a problem as the decision statistic  $\Lambda_{b,RW}^k$  can achieve the nominal  $P_{FA}$  of  $10^{-4}$  for  $N_v \geq 10^4$  regardless of the unknown disturbance distribution and the particular choice of the beamformer (please refer to [FSG<sup>+</sup>20] for details).

However, in the second case, in which there is a target hidden within those clutter angles, the omnidirectional approach would fail to detect such a target. Therefore, in order to improve the detection performance, the beamformer has to be chosen accurately. As a matter of fact, indeed the procedure in eq. (4.17) only maximizes the worst beampattern towards certain angles. However, in order for the beamformer to apply strong notches to suppress the impact of interference, the optimization problem must be changed to maximize the **SINR**. However, this is only possible if prior information about the interference spatial angles is available. Such an assumption is rarely practical. Meanwhile, our proposed **RL** approach improves the detection performance and, at the same time, maintains the **CFAR** with respect to the unknown disturbance distribution.

In order to support this claim, four targets are simulated at  $\nu = \{-0.2, 0, 0.2, 0.3\}$ . From Fig. 4.10 a, it is noticed that our algorithm is able to detect the target at  $\nu = 0$  hidden within the strong clutter while the orthogonal waveform could not as shown in Fig. 4.10 b. This shows that our algorithm can detect targets within strong interference. Furthermore, in the presence of clutter with strong peaks at certain angles, our approach would still foresee such a problem. Hence, with the aid of **RL** beamformer and the asymptotically accurate statistic, it can achieve **CFAR** property and remarkably good detection performance.

#### 4.5.4 Dynamic Environment

In these simulations, the environment changes, and the performance of our algorithm is analyzed such that the radar agentâFIXME™s capability to adapt to those changes is tested. The number of total time steps is 100 and the results are averaged over 1000 Monte Carlo runs.

##### Scenario 5 : Changing Spatial frequencies

In this scenario, the targets' spatial frequencies are changed after 50 time steps. In this case,  $\nu$  is changed from  $[-0.2, 0, 0.2, 0.3]$  to  $[-0.05, 0.05, 0.25, 0.35]$  where the new spatial frequencies are depicted in dashed blue in Fig. 4.3. In this case, we aim at simulating a dynamic environment as shown in Fig. 4.11, while their respective SNR remains the same, where  $N_v = 10^4$  and  $P_{FA} = 10^{-4}$ . On one hand, Fig. 4.11b shows the performance of the omnidirectional case, where it can detect only targets whose new spatial frequencies are located where the disturbance **PSD** is low, i.e.,  $\nu = 0.1$ . On the other hand, the **RL** based beamforming algorithm can detect all the targets, even those lying close to the disturbance **PSD** peaks. Since the algorithm is an online learning framework, no training was considered to generate Fig. 4.11. Thus, it can be noticed at  $K = 50$ , there are a few time steps where the detection

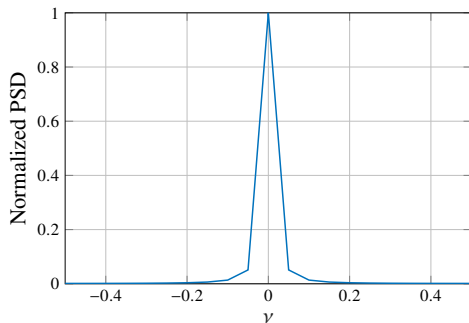


Figure 4.9: Clutter PSD with narrow peak at  $\nu = 0$

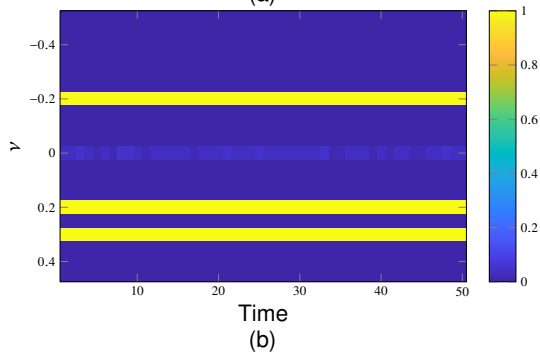
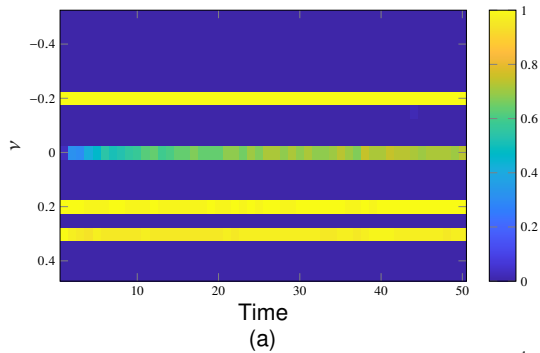


Figure 4.10: Performance of (a) RL based beamforming vs (b) Omnidirectional one in the presence of narrow clutter peak at  $\nu = 0$ .



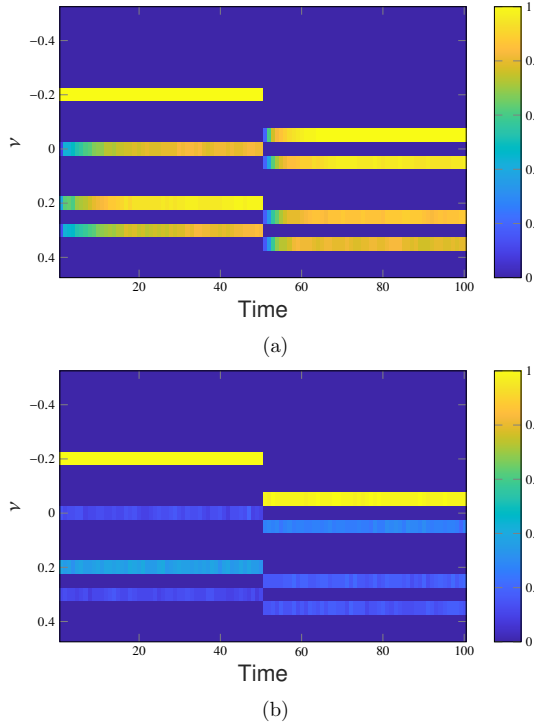


Figure 4.11: Detection performance of (a) RL based beamforming vs (b) omnidirectional with equal power allocation for dynamic environment: changing angles at  $K = 50$ .

values drop, then goes up again. This happens because the agent requires a few time steps to adapt to the new environment, hence updating the  $\mathbf{Q}$  function accordingly. Similar to scenario 1, Fig. 4.12 shows the reward behavior across time as calculated in eq. (4.20) and averaged over the Monte Carlo runs. The reward shows convergence after  $K = 20$  time steps. Then when the environment is changed by changing the angles, the agent senses that change through exploration. Hence, the drop in the reward is seen after  $K = 50$  time steps, where the agent starts re-learning the changes, then after 10 time steps, the reward converges again.

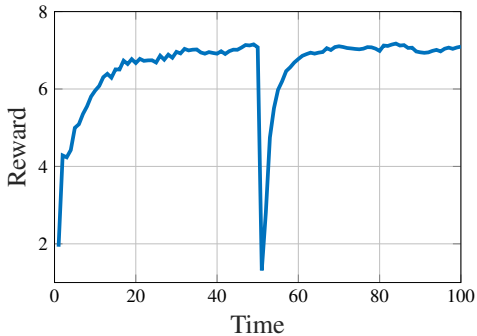


Figure 4.12: RL reward in dynamic environments: changing angles at  $K = 50$ .

### Scenario 6: Fading Targets

Here we simulate a different change in the environment, where we assume that the targets are fading and their SNR is decreasing. In Fig. 4.13, the targets' SNRs are assumed to decrease by 20% every 30 time steps. Hence, by  $K = 90$ , all targets' SNRs would have decreased by 60%. In Fig. 4.13b, the omnidirectional approach could not detect most of the targets after the first 30 time steps. Furthermore, the first target located at  $\nu = -0.2$ , which proved very good performance in the previous simulations due to its good SNR starts fading at  $K = 90$ . This proves that the omnidirectional approach fails in the fading scenarios since the radar here does not learn anything from the environment, unlike in the RL case. Hence, it can not adapt to such changes. However, our proposed RL based beamforming algorithm obviously proves to have a reliable performance across the entire time steps. It can be concluded that RL cognitive MMIMO radar can adapt very well to all environmental changes with very good performance. The corresponding reward behavior is shown in Fig. 4.14, where the algorithm can adapt to those changes in the SNR without any convergence issues.

### Scenario 7: Changing number of targets

In this scenario, we simulated total time of  $K = 60$  pulses, with  $N_v = 10^4$ ,  $P_T = 1$  and  $P_{FA} = 10^{-4}$ . The targets angles and SNR change over five time intervals  $[1, \dots, 10, 11, \dots, 20, 21, \dots, 35, 36, \dots, 50, 51, \dots, 60]$  as below

1.  $k = 1 \rightarrow 10$ , two targets at angles  $\nu = \{-0.2, 0\}$  with respective SNR of -5 and -9 dB.
2.  $k = 11 \rightarrow 20$ , no targets at all

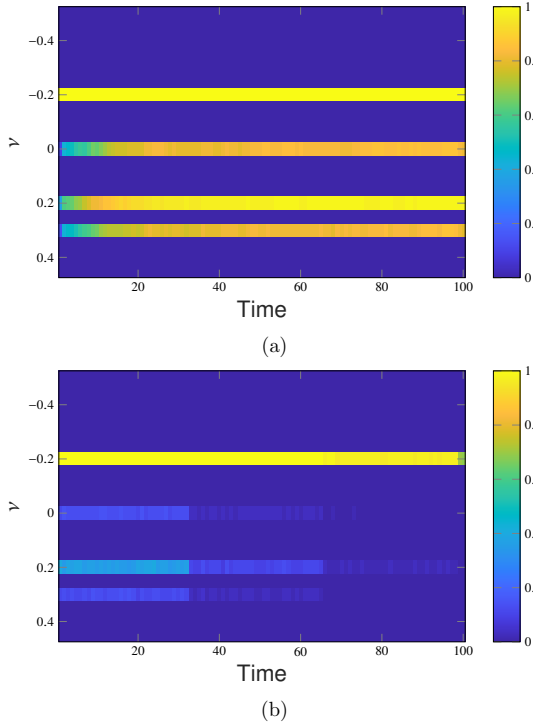


Figure 4.13: Detection performance of (a) RL based beamforming vs (b) omnidirectional with equal power allocation for dynamic environment i.e., target's SNR decreases by 20 % every 30 time steps.

3.  $k = 21 \rightarrow 35$ , five targets at angles  $\nu = \{-0.2, 0, 0.15, 0.25, 0.3\}$  with respective SNR of -6, -8, -10, -11 and -12 dB
4.  $k = 36 \rightarrow 50$ , two targets at angles  $\nu = \{0, 0.2\}$  with respective SNR -9 and -8 dB.
5.  $k = 51 \rightarrow 60$  there exist 4 targets at angles  $\nu = \{-0.05, 0.05, 0.15, 0.25, 0.35\}$  with respective SNR -8,-7,-10 and -13 dB.

As depicted in Fig. 4.15, the RL beamformer is able to track all the targets, while the orthogonal beamformer failed to track most of the targets whose SNR is low or hidden within the clutter. In more detail, in the time interval (1), both approaches can detect  $\nu = 0.2$  as it has high SNR, unlike the case when  $\nu = 0$ , where the RL

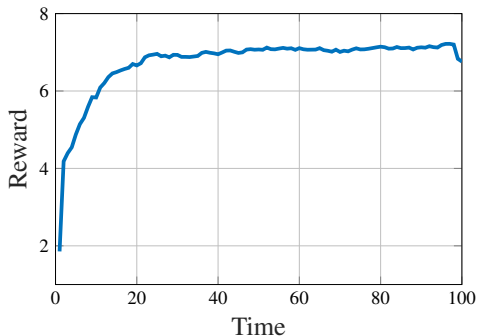


Figure 4.14: RL reward in dynamic environments: fading targets.

approach shows better detection.

In time interval (2) both algorithms don't detect any targets due to the accuracy of the detection statistic used  $\Lambda_{b, \text{RW}}^k$  as  $N_v$  grows asymptotically. In time interval (3), the omnidirectional approach faces difficulties detecting angles  $\nu = \{0, 0.3\}$  as they lie within high clutter PSD. In addition, it also fails to detect angle  $\nu = 0.25$  although it lies within low clutter PSD, due to the fact that this angle has very low  $\text{SNR} = -11$  dB. In time intervals (4) and (5), similar behavior is observed, where the omnidirectional approach fails to detect targets having low SNR or lying within high clutter PSD. However, our RL beamformer can even detect targets suffering from both problems at the same time as the case in time interval (5) with angle  $\nu = 0.35$ .

### Computational complexity

In order to evaluate the complexity of the optimization algorithm proposed in Algorithm (2), the computational time/complexity is measured using the Matlab tic-toc function. This is done for both our algorithm and the conventional SDP solution presented in [LMS<sup>+</sup>10] using the same simulation conditions. Fig. 4.16 shows both solutions achieve similar performance for low  $M$  values. However, as the number of transmit antennas  $M$  increases asymptotically, our proposed algorithm shows much less time complexity compared to the SDP solution. Hence, it can be deduced that Algorithm (2) is highly efficient for MMIMO regimes. In order to test the robustness of our algorithm, we analyze its performance against different disturbance scenarios characterizing harsh environments. We compare the performance of our RL-based waveform matrix selection scheme against omnidirectional transmission with equal power allocation. In the latter case, the orthonormal waveforms are transmitted and the total power is equally divided across all antennas under the constraint  $P_T = 1$ . We analyze three different scenarios.

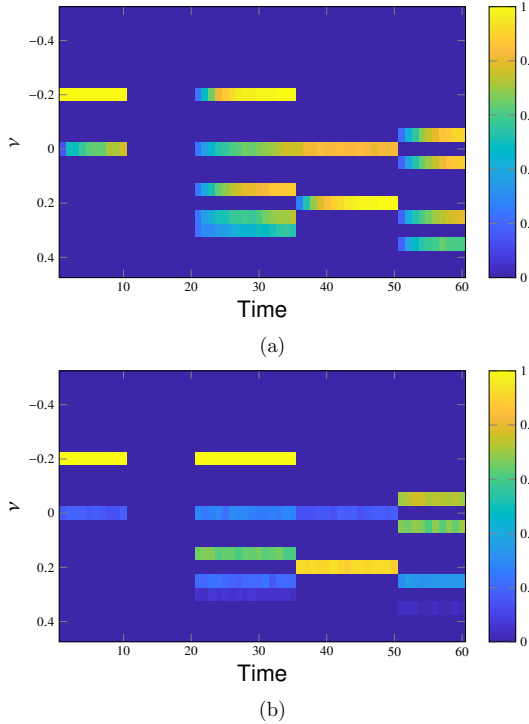


Figure 4.15: Detection performance of (a) **RL** based beamforming vs (b) omnidirectional with equal power allocation for dynamic environment i.e., target's SNR and number changes over five time intervals.

### 4.5.5 Robustness

In this set of simulations, we verify the overall robustness of the joint **RL**/Wald-type detector. To this end, extensive investigations have been performed to check its effectiveness against different (unknown) disturbance distributions by using  $P_{FA}$  and  $P_D$  as performance metrics. More specifically, the **CFAR** property (i.e., the  $P_{FA}$ ) and the power of the test (i.e., the  $P_D$ ) are assessed for *i*) different level of disturbance spikiness and *ii*) for different (autoregressive) model orders.

#### Varying the Spatial Channels

Fig. 4.17 shows the  $\hat{P}_D$  for the target at  $\nu = 0.3$  as function of  $N_v$  for a pre-assigned  $P_{FA} = 10^{-4}$ . It can be shown that the estimated  $\hat{P}_D$  of the **RL** algorithm through

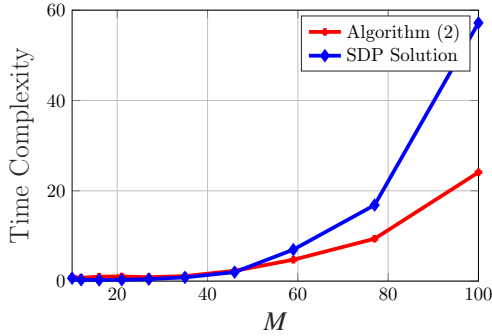


Figure 4.16: Performance evaluation of proposed optimization algorithm (2) and SDP solution as in [LMS<sup>+</sup>10]

multiple Monte Carlo runs agrees perfectly with the theoretical nominal one provided in eq. (A.5). Furthermore, theoretically, the robust Wald-type test used achieves

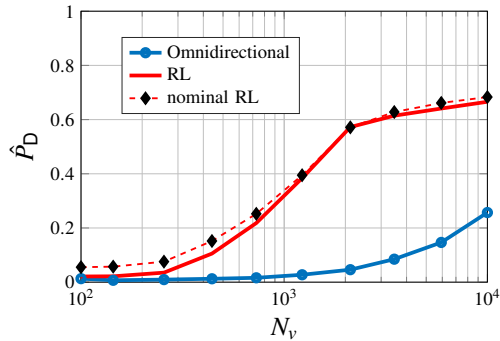


Figure 4.17:  $\hat{P}_D$  at  $P_{FA} = 10^{-4}$  across  $N_v$

the CFAR property w.r.t. all the disturbance distributions satisfying Assumption 1. Hence, when a sufficiently large number of transmitting and receiving antennas is used as proven in [FSG<sup>+</sup>20], a constant  $P_{FA}$  is achieved for  $N_v \geq 10^4$ . This behavior does not depend on the particular beamforming algorithm. Such a case is shown in Fig. 4.18, where we simulate the  $P_{FA}$  of spatial frequency  $\nu = 0$  across  $N_v$ , with the same setup as in study case 1, for both the RL and the omnidirectional approach. It can be seen that both approaches provide a constant false alarm as  $N_v \rightarrow 10^4$ . Hence, this confirms the CFARness of the proposed RL-based scheme.

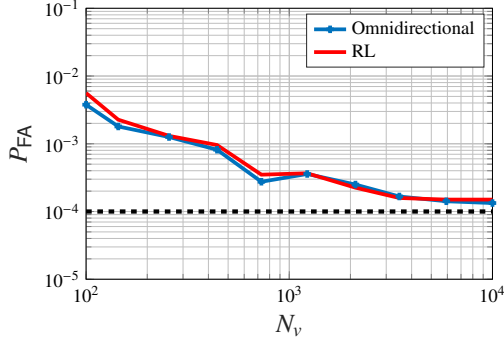


Figure 4.18:  $P_{\text{FA}}$  across different spatial channels  $N_v$  with nominal  $P_{\text{FA}} = 10^{-4}$  represented by dotted black line.

#### 4.5.6 Varying the Disturbance non-Gaussianity Levels

In this scenario, we assess the robustness of our algorithm against a different level of non-Gaussianity of the disturbance. We choose  $N_v = 10^4$  and  $P_{\text{FA}} = 10^{-4}$ . Fig. 4.19 shows the  $\hat{P}_D$  as function of the non-Gaussianity parameter  $\mu$ . The results show a constant  $\hat{P}_D$  for the target at  $\nu = 0.3$  across different values of  $\mu$ . This proves that the algorithm has a robust and constant superior behavior compared to the omnidirectional approach. In addition, as expected, the estimated  $\hat{P}_D$  match perfectly with the nominal theoretical one provided in eq. (A.5). In Fig. 4.20, the CFARness

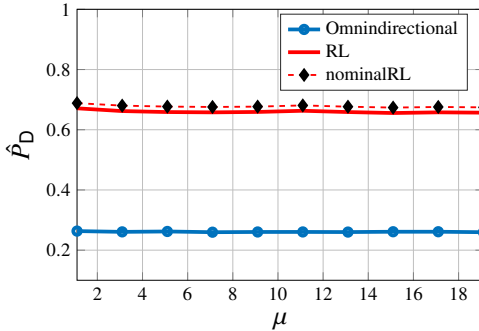


Figure 4.19:  $\hat{P}_D$  at  $P_{\text{FA}} = 10^{-4}$  and  $N = 10^4$ .

of the algorithm is assessed against the disturbance spikiness. Fig. 4.20 shows that our RL algorithm provides a constant  $P_{\text{FA}}$  across  $\mu$ , similar to the omnidirectional

approach. Both algorithms achieves the nominal  $\bar{P}_{\text{FA}} = 10^{-4}$ . This proves the theoretical results in Eq. A.3, which indicates that the **CFAR** property is always (asymptotically) achieved using the Wald-type statistic  $\Lambda_{b,\text{RW}}^k$  irrespective of the specific waveform matrix  $\mathbf{V}$ . This is a consequence of eq. (A.3) that shows that, under  $H_0$ ,  $\Lambda_{b,\text{RW}}^k(\mathbf{y}_{b,g}^k|H_0)$  is distributed as a central  $\chi_2^2$  random variable regardless of  $\mathbf{V}$ .

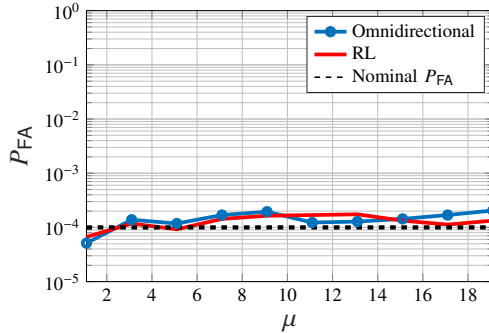


Figure 4.20:  $P_{\text{FA}}$  at  $N_v = 10^4$  across  $\mu$ .

#### 4.5.7 Varying the Order of Auto-Regressive (AR) Process

The robustness of the **RL** algorithm is further validated across more general disturbance models. In this scenario, the  $\hat{P}_D$  is evaluated across many orders of the **AR**. Specifically,  $p$  (i.e. the order of the **AR** process) varies in  $p \in [1, \dots, 10]$ . The magnitude of  $\rho_n$  in eq. (4.35) is chosen such that

$$\rho_n \in [0.8, 0.7, 0.7, 0.6, 0.6, 0.4, 0.4, 0.5, 0.5, 0.3]$$

while the corresponding spatial frequency of  $\rho_n$  is selected from

$$\nu \in [0, 0.1, -0.1, 0.2, -0.2, 0.1, -0.1, 0.4, -0.4, 0.5]$$

For instance, if  $p = 1$ , then  $\boldsymbol{\rho} = 0.8e^{j2\pi 0}$ , while if  $p = 2$ , then

$$\boldsymbol{\rho} = [0.7e^{-j2\pi 0.1}, 0.8e^{j2\pi 0}, 0.7e^{j2\pi 0.1}].$$

Fig. 4.21 shows the probability of detection of the target at  $\nu = 0$ . Note that at  $\nu = 0$  we always have a disturbance peak, regardless of the value of  $p$ . Despite that, the  $\hat{P}_D$  of this target using our algorithm is constantly higher compared to the omnidirectional case, no matter the order of the **AR**. It can be noticed a slight drop in the case of **AR**(1) (i.e.,  $p = 1$ ) as all the disturbance energy, in this case, is focused



on the target at  $\nu = 0$ , while an  $\text{AR}(p > 1)$  will spread it all over multiple spatial frequency points. Again here, the estimated  $\hat{P}_D$  agrees with the theoretical nominal  $\hat{P}_D$  in eq. (A.5).

Finally, Fig. 4.22 shows that the CFAR property with respect to the order  $p$  is satisfied for both the proposed RL-based and the omnidirectional algorithms. Again, this represents a numerical validation of the theoretical result that the CFAR property is satisfied using the Wald statistic  $\Lambda_{b,\text{RW}}^k$  in any disturbance statistics independent on  $\mathbf{V}$ .

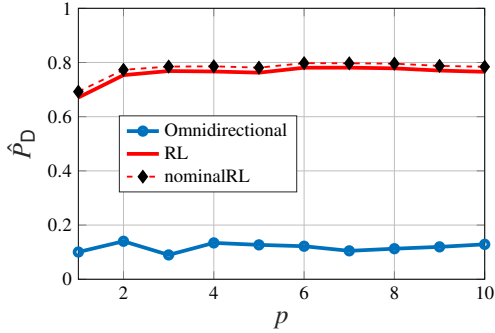


Figure 4.21:  $\hat{P}_D$  at  $P_{\text{FA}} = 10^{-4}$  across several  $p$

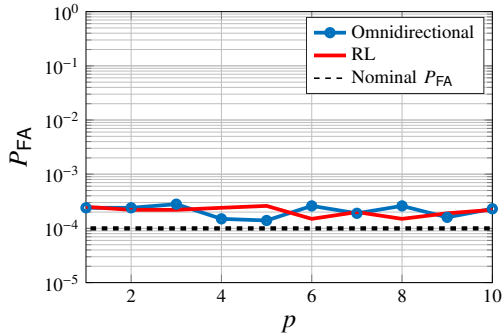


Figure 4.22:  $P_{\text{FA}}$  at  $N_v = MN = 10^4$  across  $p$ .

## 4.6 Summary

In this chapter, we studied the problem of multi-target detection for a **MMIMO CR** in the presence of an unknown disturbance. We proposed a novel **RL** based beamforming algorithm, which could detect the targets with very low SNR even if the environment is dynamic. Specifically, the **CR** acted as an agent sensing the unknown environment (i.e., targets and disturbance) by illuminating it by transmitting a set of waveforms. Afterward, a reward function is calculated from the reflected echoes. This reward has been defined as the closed form asymptotic expression of the  $\hat{P}_D$  as the number of virtual spatial antenna channels  $N_v$  go to infinity that is the **MMIMO** regime [FSG+20]. The agent's goal is to maximize the reward through a course of actions without any a priori knowledge about the disturbance distribution, or the targets' number. In our case, those actions were tailoring the beam pattern by optimizing the beamformer according to the acquired knowledge.

Furthermore, we presented a novel approach for beamforming optimization, which is scalable as the size of  $N_v$  increases and does not increase the complexity. Our numerical results showed a really good  $P_D$  performance for our algorithm as  $N_v \rightarrow 10^4$  compared to the adaptive and omnidirectional approaches. In addition, the **ROC** confirmed the advantages of adopting a **RL**-based approach when the targets are embedded in a spatially correlated heavy-tailed disturbance. The probability of detecting the low- SNR targets improves significantly. Moreover, a dynamic environment has been simulated by changing target angles, number along with target fading. In both cases, the proposed **RL**-based beamformer is able to adapt to the fast-changing environment, without any a priori knowledge, and to provide better performance than the classical (omnidirectional) beamformer. Furthermore, the robustness of the detector proposed is investigated. The performance of the algorithm has been assessed for various unknown disturbance models. Our **RL**-based Wald-type detector is able to achieve the **CFAR** property with respect to a wide range of (unknown) disturbance models. At the same time, the **RL**-based waveform selection scheme will provide the detector with a remarkable increase of its  $P_D$  while keeping the **CFAR** property. Last but not the least, the estimated  $P_D$  obtained by using the **RL**-based scheme agrees with the theoretical closed-form expression provided in [FSG+20].

# 5 Deep Learning based DOA for Small MIMO Antenna Arrays

In the last chapter, we studied the multi-target detection problem from ML perspective. In this chapter, we extend our studies to exploit the DOA problem, where we investigate the current advances of deep learning to enhance the resolution of MUSIC algorithm for MIMO systems. In general, the radar angular resolution is affected by the antenna aperture size. In addition, specifically, the resolution of MUSIC algorithm is affected by multiple factors: the number of antennas, the number of snapshots, and the SNR. In this chapter, we investigate the degradation of MUSIC performance using a small number of antennas specifically in low SNR regimes. Furthermore, we propose an efficient solution to solve this problem, without the need to increase the number of antennas, the aperture size, the number of snapshots, or the spacings between the antennas. This is done with the aid of deep learning. In section 5.1, we provide an overview of the current approaches for enhancing the DOA resolution without increasing the physical number of antennas. In addition, we briefly discuss the contribution of this chapter. Afterward, in section 5.2, we formulate the system model, then we propose to use the received signal of a small number of antennas to extrapolate the received signal of other antennas using a deep neural network (DNN) architecture in 5.3. We compare the performance of our DNN across small and large arrays in different SNR scenarios, furthermore, we perform extensive analysis to select the best training and test SNR in section 5.4. Finally, the chapter is concluded in 5.5.

## 5.1 Related Work

Accurate DOA estimation can be achieved using large antenna arrays at the cost of increased hardware and computational complexity. However, multiple input multiple output (MIMO) radars with co-located antennas can offer virtual enlargement of the aperture at the receiver, using relatively few physical antennas. This in turn significantly increases the maximum number of targets that could be detected and enhances the angular resolution at a compact size, due to the fact that MIMO radars can transmit multiple probing signals, which can be correlated or uncorrelated [LS07, BF03]. As an alternative approach, sparse array radars (also known as thin array radars) have been extensively studied in the literature and found to offer similar advantages as MIMO radars [Mie17]. The idea is to decompose a filled array into two sub-arrays, breaking the uniform spacing rule, hence achieving a larger aperture. By

this means, it can offer similar target detection and angular resolution capabilities as the MIMO radar [UY16] with lower hardware cost. For this purpose, several array configurations were proposed in the literature [Mof68, PV10, QZA15]. However, sparse arrays suffer from the effect of grating lobes due to the non-uniform spacing between the antennas, which leads to large estimation errors [KB10]. Furthermore, existing vector space DOA methods such as the MUSIC algorithm can not be directly applied, due to the rank deficiency of the correlation matrix. Hence, a spatial smoothing variant of MUSIC is proposed in [PV11] for rank enhancement at the cost of increased computational cost. This is due to the fact that spatial smoothing must be performed for every DOA estimation.

A comparison between MIMO and sparse array radars has been conducted in [Mie17], where MIMO radars were found to be preferable when compactness is essential since sparse arrays are characterized by their large aperture size. However, sparse arrays might be preferable when the hardware cost is the driving requirement, yet sparse arrays are not robust to sensor failures unlike ULA [LV18], which could present an added challenge. In this chapter, we attempt to emulate the received signal of a large ULA using only a significantly smaller sub-array, without the need to increase the array aperture size, through training a deep neural network. This is followed by using the trained model for each received pulse to estimate the DOA via employing MUSIC without any further processing, thereby delivering the advantages of sparse arrays without increasing the aperture size, and without compromising accuracy. Also, no additional computational cost due to spatial smoothing is required. Briefly, the contribution of this chapter is the following:

1. DOA resolution enhancement of small antenna arrays using a DNN that learns the mapping between received signals of two differently-sized antenna arrays. Surprisingly, the performance obtained by using actual large antenna arrays is not only tightly approximated, but exceeded at low SNR for high-angle ranges.
2. Analysis of the best training SNR as a function of the test SNR, as well as in presence of test SNR uncertainty. Interestingly, the behavior of this function is observed to vary dramatically for different angle ranges.
3. Analysis of the denoising capabilities of the proposed DNN. We attribute - based on experimental evidence - our approach's superior performance to the large antenna setup at high angle ranges and low SNR, to a denoising DNN functionality that effectively increases input SNR.

## 5.2 System Model

Consider a co-located MIMO radar system with  $M$  Tx antennas and  $N$  Rx antennas. Here, each transmit antenna with index  $m$  transmits a narrow-band signal  $s_m(t)$  with non-dispersive propagation, that is perfectly orthogonal to the rest and consists of a train of  $K$  non-overlapping pulse waveforms; each with duration  $T$ . For simplicity, we

consider **Tx** and **Rx** antennas in a **ULA** configuration with antenna spacing of  $d = \lambda_c/2$ , where  $\lambda_c$  is the wavelength. We further assume that there are  $L$  targets in the scene. The **RCS** - based on pulse  $k$  - and the **DOA** of the  $l$ -th target are given by  $\alpha_{l,k} \in \mathbb{C}$  and  $\theta_l$ , respectively. In this chapter, the target **RCS** is modeled based on the Swerling model II, where it is fixed during the pulse interval  $T$  and changes independently from one pulse interval to another [Swe60]. We define the transmit and receive steering vectors of the  $l$ -th target as  $\mathbf{a}_t(\theta_k) = [1, e^{jrd \sin \theta_k}, \dots, e^{jrd(M-1) \sin \theta_k}]^T$  and  $\mathbf{a}_r(\theta_k) = [1, e^{jrd \sin \theta_k}, \dots, e^{jrd(N-1) \sin \theta_k}]^T$ , respectively. Here,  $(\cdot)^T$  is the transpose, and  $r = \frac{2\pi}{\lambda}$ . Here, we consider all targets as point targets. In that case, the received echo (reflected signal) from the target does not expand beyond the radar resolution cell [BL98]. The received signal  $\mathbf{y}_k(t) \in \mathbb{C}^N$  after transmitting pulse  $k$  is hence [LS07],

$$\mathbf{y}_k(t) = \sum_{l=1}^L \alpha_{l,k} \mathbf{a}_r(\theta_l) \mathbf{a}_t^T(\theta_l) \mathbf{s}(t - \tau_l) + \tilde{\mathbf{n}}(t), \quad (5.1)$$

where  $\tilde{\mathbf{n}}(t) \in \mathbb{C}^N$  is independent and identically distributed (i.i.d) Gaussian noise with variance  $\sigma_{\tilde{\mathbf{n}}}^2$  and  $\mathbf{s}(t) = [s_1(t), \dots, s_M(t)]^T$ .  $\tau_l$  is the time delay due to the target position with respect to the radar. Next, at each receive antenna, the received signal  $\mathbf{y}_k(t)$  is cross-correlated with  $M$  matched filters corresponding to each transmit signal tuned at delay  $\hat{\tau}$  as given below

$$\mathbf{Z}_k(\hat{\tau}) = \int_0^T \mathbf{y}_k(t) \mathbf{s}^H(t - \hat{\tau}) dt. \quad (5.2)$$

We assume that the matched filter is perfectly tuned to the target delay [Fri12b], hence  $\hat{\tau} = \tau_l$ . Due to the perfect orthogonality of the transmit waveforms,  $\mathbf{Z}_k$  in eq. (5.2) is

$$\mathbf{Z}_k = \sum_{l=1}^L \alpha_{l,k} \mathbf{a}_r(\theta_l) \mathbf{a}_t^T(\theta_l) \mathbf{I} + \int_0^T \tilde{\mathbf{n}}(t) \mathbf{s}^H(t - \hat{\tau}) dt. \quad (5.3)$$

Here,  $\mathbf{I}$  is an identity matrix. In this model, we assume perfectly orthogonal waveforms. However, if this is not the case, such that  $\mathbf{R}_s = \int_0^T \mathbf{s}(t - \hat{\tau}) \mathbf{s}^H(t - \hat{\tau}) dt \neq \mathbf{I}$  is not the identity matrix, then two challenges would arise. First, the transmit steering vector would be effectively altered with the correlation matrix  $\mathbf{R}_s$ , where the updated transmit steering vector would be  $\hat{\mathbf{a}}_t^T(\theta_l) = \mathbf{a}_t^T(\theta_l) \mathbf{R}_s$ . Second, the noise would be spatially correlated, and hence conventional **DOA** algorithms can not be directly applied, as further pre-whitening techniques may be needed as in [Zhe17]. Next, we rearrange eq. (5.3) as

$$\mathbf{Y} = \mathbf{A}(\theta) \Phi + \tilde{\mathbf{N}}, \quad (5.4)$$

where  $\mathbf{Y} \in \mathbb{C}^{M \times K}$  is the receive signal and it is given as  $\mathbf{Y} = [\text{vec}(\mathbf{Z}_1), \dots, \text{vec}(\mathbf{Z}_K)]$ . Here,  $\text{vec}(\mathbf{Z}_k)$  denotes the conversion of the matrix  $\mathbf{Z}_k$  of eq. (5.3) into a column vector. The steering vector matrix  $\mathbf{A}(\theta)$  is given by  $[\mathbf{d}(\theta_1), \dots, \mathbf{d}(\theta_L)]$ , where  $\mathbf{d}(\theta_l) = \mathbf{a}_t(\theta_l) \otimes \mathbf{a}_r(\theta_l)$ . Further, the **RCS** matrix  $\Phi \in \mathbb{C}^{L \times K}$  corresponding to all  $L$  targets is given as  $\Phi = [\phi_1, \dots, \phi_K]$ , with  $\phi_k = [\alpha_{1,k}, \dots, \alpha_{L,k}]^T$ .

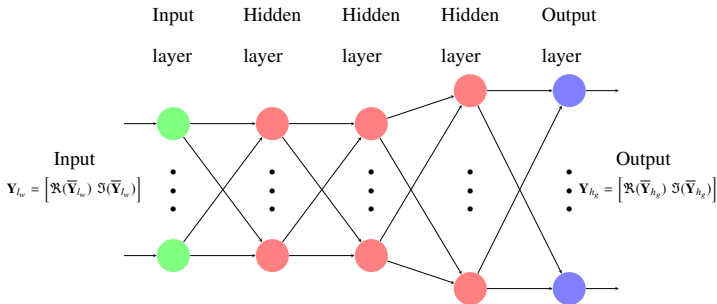


Figure 5.1: Training the Deep Neural Network.



Figure 5.2: Antenna array reconstruction using the DNN.

### 5.3 Deep Learning Architecture

Enlarging the antenna array aperture enhances angular resolution capabilities, which in turn leads to better DOA estimation. Hence, we tackle the problem of mapping the received signal of two antenna setups of different sizes. A feedforward DNN is proposed to learn the mapping between the received signals of small and large antenna setups. The operation of DNN and its relevant definitions were explained in 2.5.1.

Let  $\bar{\mathbf{Y}}_{l_w} \in \mathbb{C}^{L_w \times K}$  and  $\bar{\mathbf{Y}}_{h_g} \in \mathbb{C}^{H_g \times K}$  be the received signals of the small and large antenna setups as defined in eq. (5.4), respectively. Here,  $L_w < H_g$ , where  $L_w = M_{l_w} N_{l_w}$  and  $H_g = M_{h_g} N_{h_g}$ .  $\bar{\mathbf{Y}}_{h_g}$  and  $\bar{\mathbf{Y}}_{l_w}$  are then given as

$$\bar{\mathbf{Y}}_{l_w} = \mathbf{A}_{l_w}(\theta)\Phi + \tilde{\mathbf{N}}_{l_w}, \quad (5.5)$$

$$\bar{\mathbf{Y}}_{h_g} = \mathbf{A}_{h_g}(\theta)\Phi + \tilde{\mathbf{N}}_{h_g}, \quad (5.6)$$

where  $\tilde{\mathbf{N}}_{l_w} \in \mathbb{C}^{M_{l_w} N_{l_w} \times K}$  and  $\tilde{\mathbf{N}}_{h_g} \in \mathbb{C}^{M_{h_g} N_{h_g} \times K}$  consist of independent and identically distributed (i.i.d) complex Gaussian noise entries. Our approach is based on the hypothesis that in a complex environment, there is a non-linear relationship between both received signals corresponding to small and large antenna setups, which is a priori unknown due to the unknown locations of different targets. We hence train a DNN to learn this mapping in a data-driven fashion. In the training phase, both received signals of small and large antenna setups are available, and the DNN learns the relationship between them. The DNN consists of four fully connected layers,

where the input layer is of dimension  $L_w$ , followed by three hidden layers of dimensions  $L_w$ ,  $L_w$ , and  $H_g$ , respectively, and the output layer is of dimension  $H_g$ . The **DNN** architecture is shown in Fig. 5.1. Different **DNNs** with different configurations were tested to validate this selection. It was observed that the **DNN** with three hidden layers is the smallest **DNN** architecture that led to a good performance, on average. Since the **DNN** is not designed for special processing of complex data, the input and output are defined as  $\mathbf{Y}_{l_w} = [\Re(\bar{\mathbf{Y}}_{l_w}); \Im(\bar{\mathbf{Y}}_{l_w})]$ , and  $\mathbf{Y}_{h_g} = [\Re(\bar{\mathbf{Y}}_{h_g}); \Im(\bar{\mathbf{Y}}_{h_g})]$ . Both received and reconstructed signals are normalized to lie between 0 and 1 through min-max normalization. **ReLU** is used as the activation function for all the hidden layers. For the output layer, we tried both linear activation and **ReLU**, and then we chose the best performance for each experiment. The available dataset is divided into training, validation, and testing, with split ratios of 60%, 20% and 20%, respectively. Training takes place over a maximum of 150 epochs with a batch size of 120. For the training process, we used an Adam optimizer. Furthermore, the network loss function is defined as the mean squared error between  $\mathbf{Y}_{h_g}$  and  $\mathbf{Y}_{l_w}$ . In the testing phase, the **DNN** is tested using  $\mathbf{Y}_{l,\text{tst}} \in \mathbb{R}^{2L_w \times \hat{P}}$ , where it predicts  $\mathbf{Y}_{\text{pre}} \in \mathbb{R}^{2H_g \times \hat{P}}$ , as shown in Fig. 5.2. Here,  $\hat{P}$  is the number of testing samples. It is important to note that in the testing phase, only the received signal of the small antenna setup is available. The trained **DNN** is used to predict the received signal of the large antenna setup using the received signal of the small antenna setup. Next, **DOA** estimation is calculated from the predicted received signal  $\bar{\mathbf{Y}}_{\text{pre}} \in \mathbb{C}^{H_g \times \hat{P}}$  through the **MUSIC** algorithm as previously explained in 2.6. The covariance matrix is calculated using  $N_s$  snapshots as

$$\begin{aligned} \mathbf{R}_{\text{pre}} &= \mathbb{E}[\bar{\mathbf{Y}}_{\text{pre}} \bar{\mathbf{Y}}_{\text{pre}}^H] = \mathbf{A}(\theta) \mathbb{E}[\Phi \Phi^H] \mathbf{A}^H(\theta) + \sigma_n^2 \mathbf{I}, \\ &= \mathbf{U}_\phi \mathbf{\Lambda}_\phi \mathbf{U}_\phi^H + \mathbf{U}_{\bar{n}} \mathbf{\Lambda}_{\bar{n}} \mathbf{U}_{\bar{n}}^H, \end{aligned} \quad (5.7)$$

where  $\mathbb{E}[\cdot]$  denotes the expected value,  $\mathbf{U}_\phi$  and  $\mathbf{U}_{\bar{n}}$  are matrices containing the eigenvectors, which represent the signal and noise subspaces, respectively.  $\mathbf{\Lambda}_\phi = \text{diag}(\lambda_1, \dots, \lambda_L)$  and  $\mathbf{\Lambda}_{\bar{n}} = \text{diag}(\lambda_{L+1}, \dots, \lambda_{MN})$  contain the corresponding eigenvalues of the target and the noise, respectively. Hence, the expression of the **MUSIC** spectrum which provides the received signal energy distribution for all receive directions is given by

$$P_{MU}(\theta) = (\mathbf{d}^H(\theta) \mathbf{U}_{\bar{n}} \mathbf{U}_{\bar{n}}^H \mathbf{d}(\theta))^{-1}. \quad (5.8)$$

It is worth mentioning that since **MUSIC** uses the covariance matrix to calculate the **DOA**, it is also possible to use the covariance matrix for training instead of the received signal. However, both approaches yield the same result. For a comprehensive evaluation of our model performance, we define two metrics. First, we define the covariance matrix error as

$$R_e = \|\mathbf{R}_{h,\text{tst}} - \mathbf{R}_{\text{pre}}\|_F / \|\mathbf{R}_{h,\text{tst}}\|_F, \quad (5.9)$$

where  $\|\cdot\|_F$  is the Frobenius norm,  $\mathbf{R}_{h,\text{tst}} = \mathbb{E}[\bar{\mathbf{Y}}_{h,\text{tst}} \bar{\mathbf{Y}}_{h,\text{tst}}^H]$ , and  $\bar{\mathbf{Y}}_{h,\text{tst}}$  is the received signal of the large antenna setup during inference. The analysis of the covariance

matrix of the received signal has a significant importance here as it is directly used to calculate the **MUSIC** spectrum. Second, to evaluate the **DOA** estimation performance, the average **MSE** over  $Q_s$  trials is used as the performance metric. Here,  $Q_s = \hat{P}/N_s$ . The **MSE** in radians is given by

$$\text{MSE} = \frac{1}{LQ_s} \sum_{q_s=1}^{Q_s} \sum_{l=1}^L (\hat{\theta}_{q_s,l} - \theta_{q_s,l})^2 \quad (5.10)$$

Here, the estimated and actual angles of the  $l$ -th target in the  $q_s$ -th trial are given as  $\hat{\theta}_{q_s,l}$  and  $\theta_{q_s,l}$ , respectively.

### 5.3.1 Can the same DNN estimate the DOA directly ?

To answer this question, we have tried to use a **DNN**, with a similar architecture, to map the relationship between the received signal of the small antenna setup and estimate as well the **DOA**. However, this approach failed, as the **DNN** could not simply learn the direct mapping between the received signal and the spatial angles. The difficulty here lies in the fact that there are two different tasks to be done subsequently. The first one is the mapping relationship between both received signals, while the second one is mapping the received signal to the **DOA** directly. Hence, for an end-to-end data-driven approach, two different cascaded **DNN** must be used, each trained for the corresponding task. Therefore, one could think of using another **DNN** to replace **MUSIC** in our work after the **DNN** mapping step to estimate the **DOA** directly. However, this would require further investigation regarding the **DNN** architecture, which we plan to consider as an extension to this work.

### 5.3.2 Computational Complexity

The computational complexity of **DNN** training is governed by that of backpropagation, which is given by  $\mathcal{O}(\hat{P}n_e(H_g^2 + L_w^2))$ . Here,  $n_e$  is the number of training epochs, and  $\mathcal{O}(\cdot)$  represents the Big O notation for asymptotic computational complexity analysis. The test-time computational cost for a single trial which consists of  $N_s$  snapshots is  $\mathcal{O}(N_s H_g^2 + N_s L_w^2)$ , which is governed by inference cost along with **MUSIC** complexity, which is given by  $\mathcal{O}(n_p H_g^2 + N_s H_g^2)$  where  $n_p$  is the spatial grid search over the angles. Thus, the total test-time computational cost is  $\mathcal{O}(N_s(H_g^2 + L_w^2) + n_p H_g^2)$ .

## 5.4 Numerical Analysis

To train the **DNN**, we use a GPU server with 32 GB memory and a single NVIDIA Quadro RTX 5000. The simulation parameters are listed in table Tab. 5.1. We consider three angle ranges, which span the scope of the incident signal, however,



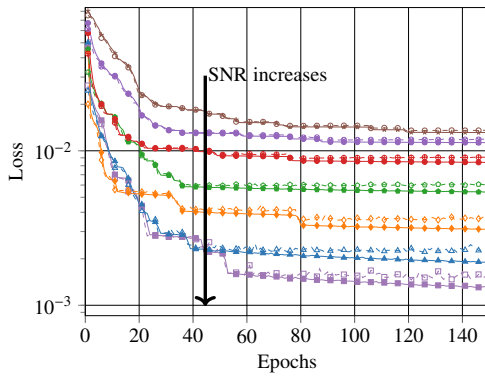
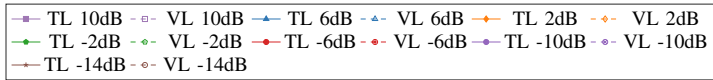
$N_{t_w} = M_{t_w}$	10	$N_{h_g} = M_{h_g}$	16
Angle grid 1	0 : 25	Angle grid 2	20 : 45
Angle grid 3	40 : 65	Number of targets ( $L$ )	4

Table 5.1: Simulation Parameters

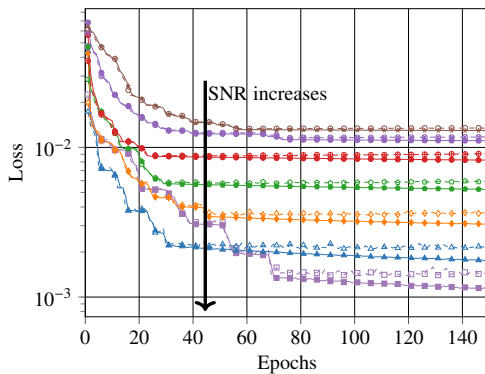
similar results were obtained for others. Each range is chosen to span 25 degrees to place the targets. Also, here we set the minimum spatial distance of five degrees between two targets to ensure the best spatial resolution of the actual large antenna setup of  $16 \times 16$  antennas. The proposed results assume that the training and testing are performed in the same angular ranges of the targets. In order to identify the corresponding trained **DNN** for each target, the testing sample is predicted using the trained **DNN** of the three ranges and the **DNN** with the lowest **MSE** is chosen. This approach was adopted to reduce the complexity of training on the whole angle range, however, this is still feasible with a large number of data to span the whole angle range  $[0 : 65]$ . Different training sets are considered in the training phase. For our simulations, we consider 16 datasets. In those datasets, we use different training data, where 14 datasets consist of 60000 samples for training and validation, in each of those sets we train the **DNN** using a single **SNR** value from the **SNR** range  $[-16 : 2 : 10]$  dB. The last two datasets, M1 and M2, contain however data with a mix of **SNR** within the same range. M1 and M2 contain equal percentage of data samples from each training **SNR** ( $\text{SNR}_{\text{train}}$ ). The only difference in constructing these two datasets is the size, as M1 consists of 840000 and M2 consists of 60000 samples for both training and validation. For the testing phase, we estimate the **DOA** for 15000 samples in the testing **SNR** ( $\text{SNR}_{\text{test}}$ ) range of  $[-16 : 2 : 10]$  dB. Here, we set the number of snapshots  $N_s$  as 150, resulting in a number of trials  $Q_s = 100$ . We assume that changing the **SNR** affects the noise of the received signal and not the target matrix  $\Phi$ .

### 5.4.1 Deep Neural Network (DNN) Performance Analysis

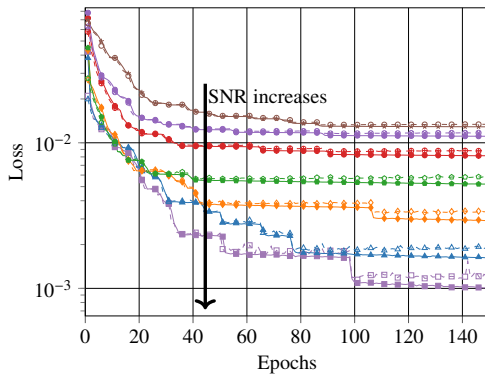
To gain insights on how the performance of the **DNN**, we evaluated the **training loss (TL)** and **validation loss (VL)** of the **DNN** for different training **SNRs** as shown in Fig. 5.3. The relation between **TL** and **VL** indicates when the patterns learned by the **DNN** do not generalize well to unseen data (overfitting regime). In case the **TL** is significantly smaller than the **VL**, then it is highly likely that the **DNN** is overfitting. In Fig. 5.3, we used the same **SNR** in training and validation. Based on the results, it can be seen that in low **SNR** regimes (i.e.,  $-14$ ,  $-10$ , and  $-6$  dB), there is almost no gap between both losses. However, as the **SNR** increases, the **TL** becomes slightly lower than the **VL** at  $-2$  dB, as we train the network for a number of epochs needed to obtain good accuracy. In addition, the gap between the **TL** and **VL** increases as the **SNR** increases (i.e.,  $2$ ,  $6$ , and  $10$  dB). Furthermore, it can be noticed from



(a) Angle range 0-25



(b) Angle range 20-45



(c) Angle range 40-65

Figure 5.3: TL and VL of the DNN for different angle ranges and training SNRs.

the figure that the **TL** and **VL** are much lower in positive **SNR** regimes compared to the negative ones. This in turn suggests that at high **SNR**, the learning task becomes easy, which makes the **DNN** more amenable to overfitting. Fortunately, in such noiseless scenarios, the problem motivating this work with smaller antenna arrays is mild, and one can choose to directly use the small antenna array received signal for **DOA** estimation.

## 5.4.2 DOA Performance

The average **MSEs** for different training datasets are shown in Fig. 5.4. In this figure, **DOA** estimation using the predicted signal of the **DNN** is compared with the **DOA** estimation obtained by directly using the signals obtained from the actual small and large antenna setups.

Three cases for the **DNN** prediction task are explored:

- Case 1: Training the **DNN** with the M1 dataset (mix of **SNR** values).
- Case 2: Training the **DNN** with the same **SNR** as that used in testing.
- Case 3: Selecting the lowest **MSE** of **DOA** estimation achieved across all 16 training sets for each testing **SNR**.

Fig. 5.4 shows that the predicted signal typically leads to better performance than directly using the signal of the small antenna setup ( $10 \times 10$ ), especially in the low **SNR** regime and for high angle ranges. However, there is one exception to this statement. As shown in Fig. 5.4(a) and (b), where the small antenna setup performs slightly better compared to the **DNN** prediction in high **SNR** regimes. This is due to the fact, that both received signals of the small and large setups have similar **DOA** performance in high **SNR**, where the **MSE** decreases dramatically in both cases. We believe that the inferior **DNN** performance, in this case, can be attributed to overfitting as the **TL** is lower than the **VL** as previously mentioned in section 5.4.1. We consider that Case 2 is the best training scenario, where the same **SNR** is used for testing and training. This case might be unrealistic in practical applications unlike Case 1. However, we use it here as a benchmark for comparison. In section 5.4.4, we address the performance when there is uncertainty about the test **SNR**. Fig. 5.4 also demonstrates that training and testing with the same **SNR** closely follow the best achievable performance, hence highlighting the impact of knowing the test **SNR** value and choosing the simple strategy of training at only that value. In addition, Fig. 5.4 demonstrates the difference in behavior among different angle ranges. More specifically, the performance of the **DOA** estimation obtained from using the signals corresponding to the actual antenna setups becomes worse for higher angle ranges. We believe that this is due to the loss of spatial resolution of the **ULA** as the target directions shift to the endfire direction of the antenna array (i.e.  $|\theta_l| \geq 60$ ). This is due to the fact that in this range, the beam sharpness reduces remarkably as the effective array aperture decreases towards those directions [IB05].

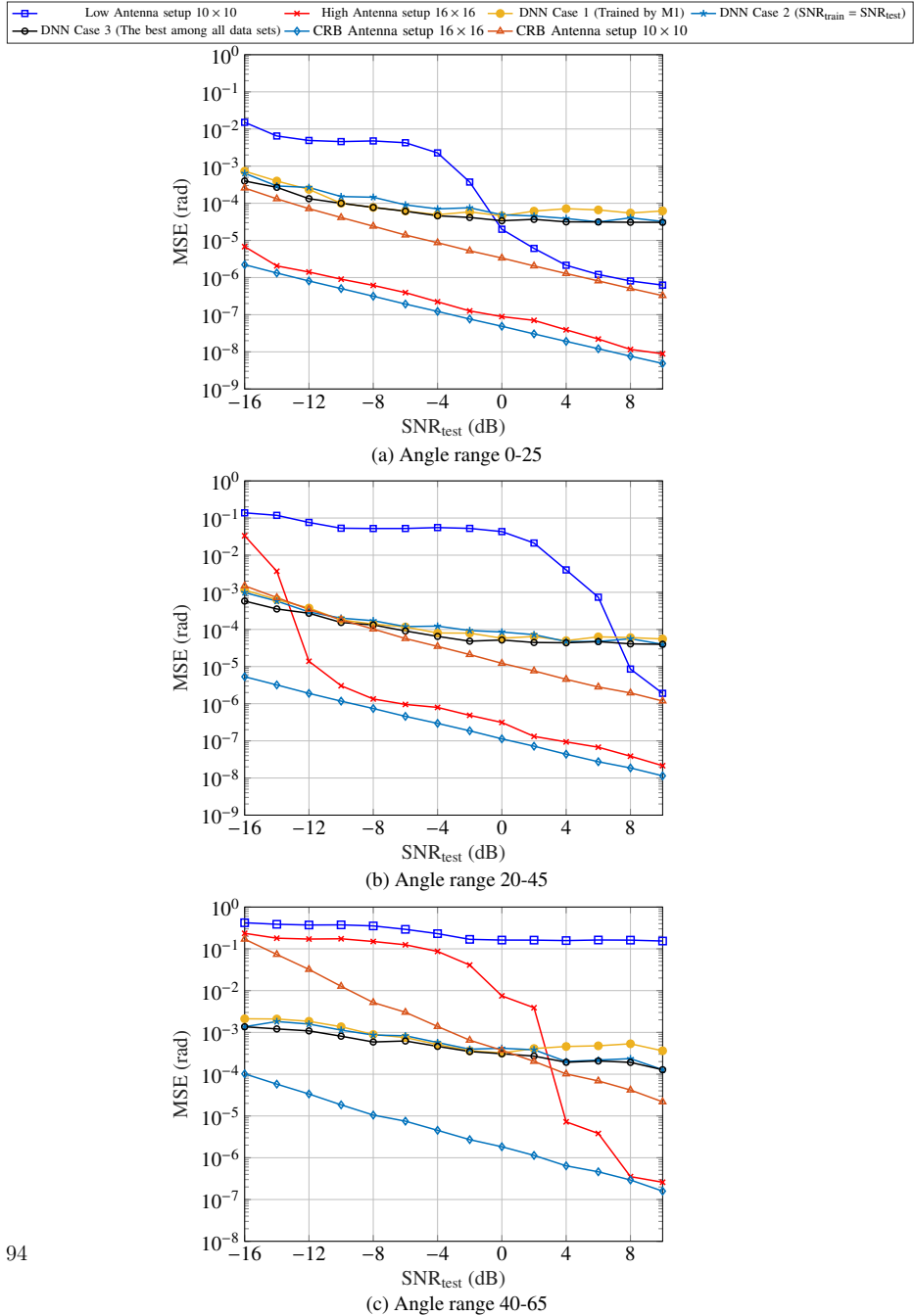


Figure 5.4: DOA estimation results and Cramér Rao Bounds.

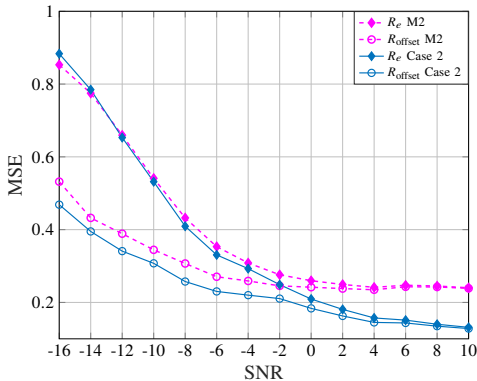


Figure 5.5: MSE of covariance matrix of predicted received signal compared to the actual large antenna setup at the same SNR and with SNR offset with ReLU output activation function.

To further assess the performance of our approach, Fig. 5.4 shows the Cramér Rao bound (CRB) of the DOA estimation of small and large antenna setups. It can be seen that the DOA estimation of the DNN-predicted signal approaches the CRB of the small antenna setup, specifically in the low SNR regime. Further, for higher angle ranges at low SNR, the MSE of the DNN-based DOA estimation is lower than the CRB of the small antenna setup. We believe that this is due to the side information benefit from the large antenna setup training signals, as well as the denoising effect. Thus, it can be deduced that our approach can enhance the estimation accuracy and improve the resolution of small arrays as well.

Interestingly, DOA estimation using our DNN-emulated signal outperforms the one generated using the actual large antenna setup at low SNR and high angle ranges. A possible explanation of this behavior is that, while pursuing improvement in generalization performance, the DNN performs denoising to the received signal. We further examine this hypothesis by evaluating  $R_e$  as defined in eq. (5.9). Then, we compare the predicted signal with the actual received signal at a certain SNR offset. Hence, we define  $R_{\text{offset}}$  as

$$R_{\text{offset}} = \frac{\|\mathbf{R}_{ho,\text{tst}} - \mathbf{R}_{\text{pre}}\|_F}{\|\mathbf{R}_{ho,\text{tst}}\|_F}, \quad (5.11)$$

where  $\mathbf{R}_{ho,\text{tst}} = \mathbb{E}[\bar{\mathbf{Y}}_{ho,\text{tst}} \bar{\mathbf{Y}}_{ho,\text{tst}}^H]$ , and  $\bar{\mathbf{Y}}_{ho,\text{tst}}$  is the actual received signal at a certain SNR offset (e.g., if  $\bar{\mathbf{Y}}_{h,\text{tst}}$  and  $\bar{\mathbf{Y}}_{\text{pre}}$  are evaluated using  $\text{SNR}_{\text{test}} = -16$  dB, then  $\bar{\mathbf{Y}}_{ho,\text{tst}}$  is evaluated using  $\text{SNR}_{\text{test}} = -8$  dB with an offset of 8 dB).

In Fig. 5.5, we plot  $R_e$  and  $R_{\text{offset}}$  using the training datasets of M2 and case 2 with offset values of 8 and 12 dB, respectively. Those offset values are chosen

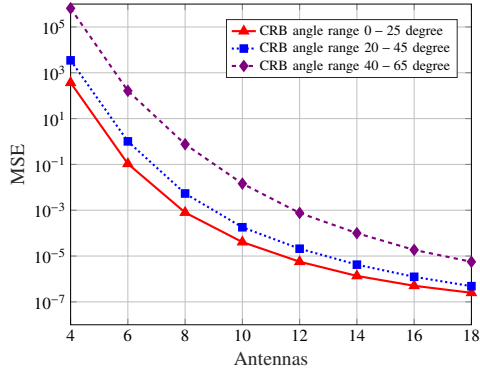


Figure 5.6: CRB of the DOA estimation vs Antennas.

based on the observed performance corresponding to both cases. Fig. 5.5 shows that  $R_{\text{offset}}$  has much lower values compared to  $R_e$  in both cases. That signifies the statistical similarity between the predicted signal of the DNN and the less noisy version of the actual received signal of the large antenna setup. Further, as the SNR increases,  $R_{\text{offset}}$  and  $R_e$  converge to the same value. This underlines the validity of the hypothesis that the DNN denoises the received signal.

### 5.4.3 Cramér Rao Bound (CRB) Analysis

The maximum number of targets ( $K_{\text{max}}$ ) that theoretically can be uniquely identified by a MIMO radar is given by [LSXR07]

$$L_{\text{max}} \in \left[ \frac{2(M+N)-5}{3}, \frac{2MN}{3} \right). \quad (5.12)$$

However, those bounds are asymptotic bounds, and rely on the assumptions that either the SNR or the number of snapshots is infinite [LS07]. In addition, it is worth noting that the accuracy of the MUSIC algorithm in identifying the targets is very sensitive to variations in the SNR and the number of antennas. In Fig. 5.4, we used the small antenna setup  $M = N = 10$  antennas, while for the large antenna setup we used  $M = N = 16$  and number of targets  $L = 4$  in both cases. In low SNR regimes, the small antenna setup suffers from high MSE values of DOA estimation, while the MSE enhances gradually as it approaches 0 when the SNR increases. One way to overcome the performance degradation is to increase the number of antennas, which is not always possible. In Fig. 5.6, we use the CRB to further elaborate this idea. The CRB of unbiased DOA estimation of MIMO radar is calculated and derived as

in [HV11].

$$CRB(\theta) = \frac{\sigma_n^2}{2N_s} \left\{ \text{Re} \left[ \mathbf{\Phi}^H \mathbf{A}_e^H \left( I - \mathbf{A} (\mathbf{A}^H \mathbf{A})^{-1} \mathbf{A}^H \right) \mathbf{A}_e \mathbf{\Phi} \right] \right\}^{-1}.$$

Here,  $\mathbf{A}_e$  represents first derivative information of the steering vector matrix  $\mathbf{A} = \mathbf{A}(\theta)$  as given by  $\mathbf{A}_e = \mathbf{A}_e(\theta) = \left[ \frac{\partial \mathbf{d}(\theta_1)}{\partial \theta_1}, \frac{\partial \mathbf{d}(\theta_2)}{\partial \theta_2}, \dots, \frac{\partial \mathbf{d}(\theta_L)}{\partial \theta_L} \right]$ . It is well known that the estimation error covariance of any unbiased estimator is lower bounded by the **CRB**. The figure shows the **CRB** for the **DOA** estimation error versus the number of antennas for different angle ranges at **SNR** = -10 dB and  $L = 4$ . It can be observed that the **CRB** decreases as the number of antennas increases. In addition, it can be noticed that **CRB** increases as the angle range go higher. This can be explained due to the loss of spatial resolution of the **ULA** as the target directions shift to the endfire direction of the antenna array (i.e.,  $|\theta_l| \geq 60$ ) previously explained. Hence, in our proposed method we aim at reducing the **DOA** estimation error for low **SNR** systems and in high angle ranges without the need to increase the number of antennas. In general, subspace methods as **MUSIC**, are highly dependent on the **SNR** of the received signal. As a matter of fact, those methods suffer from the so-called ‘‘threshold effect’’. This involves a severe degradation when either the **SNR** and/or the number of snapshots are not large enough [VML15]. Therefore, in case the received signals suffer from low **SNR** values, the algorithm cannot detect the desired targets [LYL<sup>+</sup>17]. In general, for uncorrelated sources, the **MUSIC** algorithm is asymptotically efficient (i.e., the noise variance tends to zero). This can be seen clearly in our results. Hence, our proposed method offers an efficient solution to enhance the efficiency of the small antenna setup in low **SNR** and/or high angle range regimes without the need to increase the antennas or the number of snapshots taken.

It is hence feasible to detect four targets for both considered small and large antenna setups in the scenario depicted in Fig. 5.4. However, the accuracy of **MUSIC** suffers severe degradation as the **SNR** decreases, and this performance degradation can be significantly overcome by increasing the number of antennas, which we do through DNN emulation.

#### 5.4.4 The Best Training Signal-to-Noise ratio (SNR) Values

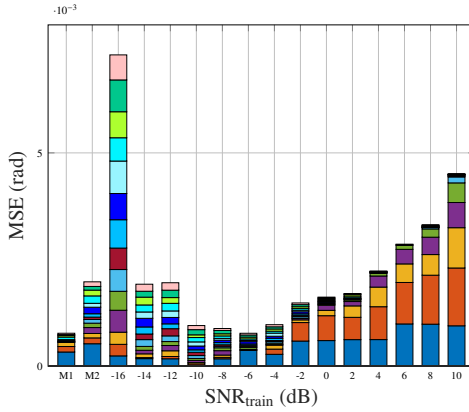
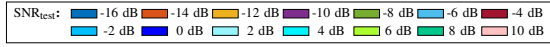
We first investigate the performance when training with a single **SNR** value across all testing **SNR** values. Fig. 5.7 shows the cumulative average **MSEs** of the **DOA** estimation over all testing **SNRs** for each training **SNR**. We observe that the training set M1 consistently provides a low cumulative **MSE**. However, it may be difficult in practice to acquire - and train with - a large dataset due to latency and computational constraints. Interestingly, the best training **SNR** value, in terms of cumulative **MSE**, shifts from low to high as we move towards higher angle ranges. Further, perhaps counterintuitively, training with high **SNR** values can lead to mild performance for low angle ranges in presence of uncertainty about the testing **SNR**. Further analysis is conducted to elaborate the relationship between the training and test **SNR**, and

the results are shown in Fig. 5.8. With respect to the average **MSE** for each pair of training and testing **SNR** values, in We observe that positive training **SNR** values are in general more favorable, especially as we move towards higher angle ranges and higher **SNR** values. However, when comparing with the results in Fig. 5.7. Thus, we conclude that knowledge of the test **SNR** favors higher training **SNR** values, while a significant uncertainty about the test **SNR** favors lower training **SNR** values, especially for lower angle ranges.

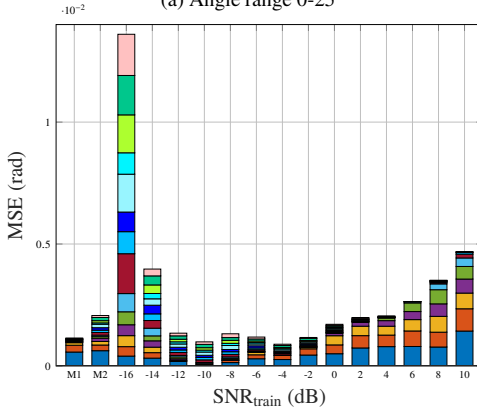
## 5.5 Summary

We introduced a novel strategy that employs deep learning for emulating large antenna arrays and demonstrated how it boosts the accuracy of **MUSIC** for **DOA** estimation. We highlighted how the emulated array leads to superior performance than an actual antenna array with the same number of antennas for high angle ranges and low **SNR** values, probably due to the denoising abilities of deep neural networks. Further, the effectiveness of training at low **SNR** values in presence of uncertainty about the test **SNR** was demonstrated, especially for low angle ranges. Finally, we investigated the best training **SNR** values as a function of the test **SNR**, and particularly noted the shift in ideal training **SNR** values from low to high as we move towards higher angle ranges and higher test **SNR** values. In this chapter, we did not address the correlation between different targets, as we assumed perfect received signals for both arrays. In the next chapter, we propose an approach to deal with this problem.

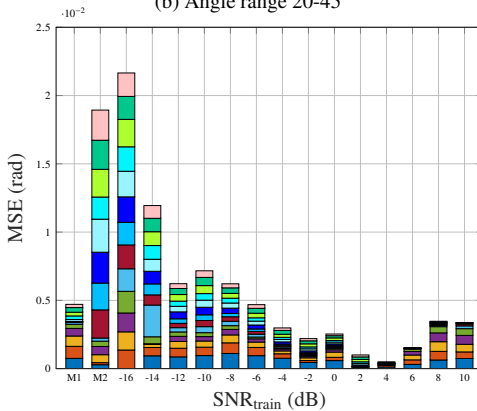




(a) Angle range 0-25



(b) Angle range 20-45



(c) Angle range 40-65

Figure 5.7: DOA estimation comparison of the DNN based signal prediction by training at a single SNR.

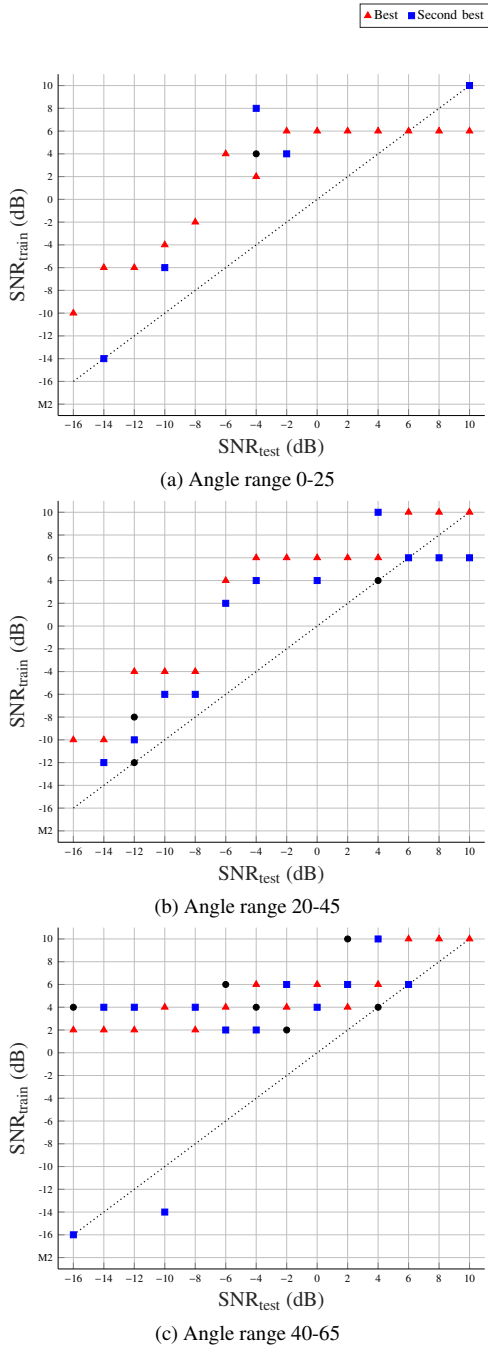


Figure 5.8: The best training SNR selection for different test SNRs.

# 6 Deep Learning for DOA for Coherent Targets using Imperfect Antenna Array

In the previous chapter, we introduced deep learning to overcome angular resolution limitations for DOA estimation in MIMO radar utilizing a small antenna array. The deep NN has shown denoising capabilities for very low SNR regimes. One related question is: can we benefit from deep learning as well to overcome other sources of signal distortion? As a matter of fact, multipath and antenna array imperfections are both considered the foremost challenges facing DOA algorithms. In this chapter, we aim to investigate the possible advantages of deep learning techniques to solve the problem of DOA estimation of coherent targets, originating due to the presence of multipath. Furthermore, we assume the existence of an imperfect antenna array such as mutual coupling, gain, phase mismatches, and position errors. In section 6.1, we review the effect of multipath and antenna array imperfections on DOA estimation, examining prior work done to solve those problems. In addition, we briefly discuss the contribution of this chapter. Afterward, in sections 6.2 and 6.3, we reformulate the system model proposed in eq. (2.11), introducing the effects of errors due to imperfections and multipath component into the model. Then, we propose a DNN framework solving both problems simultaneously in section 6.4. The performance of this framework is assessed against other algorithms from the literature in section 6.5. Finally, in 6.6, we conclude the work done in this chapter.

## 6.1 Related Work

There are various challenges affecting the accuracy and precision of DOA estimates in non-ideal scenarios, e.g., multipath and antenna imperfections. In general, the application of conventional DOA methods in real-life applications is very limited, as it requires accurate knowledge of the received signal without any errors. Hence, they are limited to specific scenarios where the antenna array measurements are ideal and the targets are not correlated. For example, the MUSIC algorithm can detect and measure multiple targets at the same time with high-precision measurement only under ideal array conditions as explained in the previous chapter. In addition, to those limitations mentioned in chapter 5, its performance degrades significantly in the existence of array imperfections. Furthermore, phased array radar fails to correctly detect coherent (fully correlated) targets in a multipath environment using

**MUSIC.** Since, unlike **MIMO**, phased array radars are only capable of transmitting the same waveform from all antennas. Thus, with the presence of multipath, the rank of the signal covariance matrix becomes less than the number of impinging signals, which significantly affects the estimation performance. To solve this problem, spatial smoothing techniques have been widely used to remove the coherence between targets or de-correlate their signals by reconstructing a full rank covariance matrix before going through the estimation algorithm [QR11b]. However, this adds processing overhead, making it difficult to use in real-time applications. Moreover, spatial smoothing only solves the coherence problem and does not solve other problems like antenna array imperfections which is a common problem in practice. As a matter of fact, those imperfections generally occur in practical applications due to the non-idealities in the antenna array such as mutual coupling, gain and phase gradual changes over time and as well as changes in the antenna locations. For instance, mutual coupling occurs due to interference from nearby antennas during transmitting [FW91], while gain and phase inconsistency can result from the aging of electrical components or thermal effects. All of those factors change the antenna array response, causing significant degradation in the performance of DOA algorithms like MUSIC [FW91]. Many approaches in the literature addressed those problems using auto-calibration algorithms as in [Sva99, LY06]. However, such algorithms require prior knowledge of the imperfections formulations, which can be challenging in practical applications. Other approaches used the latest advances in machine learning, and deep learning to solve this problem as in [LZY18a]. However, the authors in [LZY18a] only focused on the imperfections problem, where they proposed a neural network followed by a classifier. However, they didn't take into consideration the potential correlation among the targets that can result from multipath.

The contribution of this chapter is the following:

- **DOA** estimation of spatially close coherent targets with a phased array radar without any prior spatial smoothing techniques. This is done in the presence of array imperfections using a unified **DNN** framework to solve both problems.
- Significant performance enhancement compared to state-of-the-art methods for coherence removal as **SS-MUSIC** [QR11b], and to similar algorithms for imperfections as aforementioned approach found in [LZY18a].

## 6.2 Array Imperfections

The phased array model in eq. (2.11) is the idealistic received signal without any imperfections in the antenna array, which is commonly used in the literature. However, it is quite impractical. Hence, we re-define eq. (2.11) as

$$\mathbf{z}(k_s) = \sum_{l=1}^L \mathbf{a}(\theta_l, \mathbf{e}) s_k(k_s) + \tilde{\mathbf{n}}(k_s), \quad k_s = 1, \dots, K_s \quad (6.1)$$

where  $\mathbf{a}(\theta_l, \mathbf{e})$  is the array response after adding the array imperfections and  $k_s$  is the time instant. Here we consider gain and phase errors ( $\mathbf{e}_g$  and  $\mathbf{e}_p$ ), antenna position error ( $\mathbf{e}_{\text{pos}}$ ), and mutual coupling error ( $\mathbf{e}_{\text{mc}}$ ). To this end, the definition of  $\mathbf{a}(\theta_k, \mathbf{e})$  would be as [LZY18a]

$$\mathbf{a}(\theta, \mathbf{e}) = (\mathbf{I}_N + \alpha_{\text{mc}} \mathbf{E}_{\text{mc}}) \times (\mathbf{I}_N + \text{diag}(\alpha_g \mathbf{e}_g)) \times \text{diag}(\exp(j\alpha_e \mathbf{e}_p)) \times \mathbf{a}(\theta, \alpha_{\text{pos}} \mathbf{e}_{\text{pos}}) \quad (6.2)$$

$$\mathbf{e}_g = [0, \underbrace{0.2, \dots, 0.2}_{\frac{N}{2}}, \underbrace{-0.2, \dots, -0.2}_{\frac{N}{2}-1}]^T \quad (6.3)$$

$$\mathbf{e}_p = \left[ 0, \underbrace{-\frac{\pi}{6}, \dots, -\frac{\pi}{6}}_{\frac{N}{2}}, \underbrace{\frac{\pi}{6}, \dots, \frac{\pi}{6}}_{\frac{N}{2}-1} \right]^T \quad (6.4)$$

The position biases are

$$\mathbf{e}_{\text{pos}} = [0, \underbrace{-0.2, \dots, -0.2}_{\frac{N}{2}}, \underbrace{0.2, \dots, 0.2}_{\frac{N}{2}-1}]^T \times d \quad (6.5)$$

The mutual coupling coefficient vector is

$$\mathbf{e}_{\text{mc}} = [0, \gamma^1, \dots, \gamma^{N-1}]^T \quad (6.6)$$

where  $\gamma = 0.3e^{j\frac{\pi}{3}}$  is the mutual coupling coefficient between adjacent antennas,  $\alpha_i \in [0, 1], i \in \{g, p, \text{pos}, \text{mc}\}$  is weighting parameter for each error. The choice of the error values in equations (6.3), (6.4), (6.5) and (6.6) is system dependent and can be changed accordingly.  $\mathbf{E}_{\text{mc}}$  is defined as a Toeplitz matrix with parameter vector  $\mathbf{e}_{\text{mc}}$ . The imperfections model used is a simplified version of the commonly used models, such a model is adopted similarly to [LZY18a] to facilitate the analysis. However, the model is irrelevant to the proposed generic machine learning framework, since no prior information is assumed on the model nor the used imperfection values.

In addition to array imperfections, in any real scenario, the received signals would be highly correlated, due to the contribution of multipath which makes  $\mathbf{R}$  rank deficient or singular. Hence, the next section will define the model of coherent targets.

## 6.3 Multipath

In order to generate the multipath component of each target, we consider having  $L$  targets arriving from  $L$  directions. At time instant  $k_s$ , there are  $L$  transmit signals  $s_l(k_s), \forall l = 1, \dots, L$ , which arrive as replica of one of them i.e.,  $s_1(t_n)$ , but phase

delayed and magnitude weighted [QR11b]. Hence, the transmit waveform  $s_l(k_s)$  in eq. (6.1) can be redefined as

$$s_l(k_s) = g_l e^{j\phi_l} s_1(k_s), \quad l = 1, \dots, L, \quad (6.7)$$

where  $g_l$  is the amplitude factor of targets  $l$  and  $\phi_l$  is its phase change. Such a model will impose rank deficiency on the covariance matrix structure in eq. (2.13), causing the existing DOA algorithms to fail accordingly. The proposed model simulates a multipath propagation case, which leads to the presence of perfectly coherent sources. To solve such a problem, in the next section, we propose a deep auto-encoder to remove the effects of both coherence and array imperfections.

## 6.4 DOA based on Deep Learning

In this section, we investigate the use of deep learning to eliminate the errors resulting from antenna array imperfections and at the same time mitigate the effect of multipath, thus enhancing the DOA. We propose a composite framework, which consists of AE that selects the spatial sector where the sources and multipath are located followed by a beamformer that applies scanning to find the exact DOA. In the following, we will explain in detail this framework.

### 6.4.1 DNN Architecture

Here, for the DNN architecture, we propose an AE. AE is a specific type of DNN which consists of two networks: an encoder and a decoder. The encoder takes in the input vector, then compresses it to a reduced dimension. This procedure extracts the main features in the input, afterwards, the decoder takes the encoder's output and reconstructs the initial input dimension. In our proposed AE, the first hidden layer performs the function of an encoder as it reduces the dimension of the input by extracting the main features of the input. Afterwards, the encoding layer is followed by four hidden layers that help in the decoding process by retrieving the information to restore back the input of the AE. Table 6.1 shows the size of all the hidden layers. The output layer consists of six sub-regions and each region is considered as a decoder by itself. The AE acts as a spatial filter that divides the region of interest into six regions, the filters the input using those six output decoders. Therefore, each decoder retrieves specific information from the input, as shown in Fig. 6.1. The proposed architecture is different from a fully connected neural network due to the presence of the encoder in the first hidden layer. The process of encoding-decoding helps decrease the impact of disturbances in the AE input, by de-noising the input, retrieving only the useful information. The disturbance in our case is mainly due to array imperfections, noise, and coherent targets.

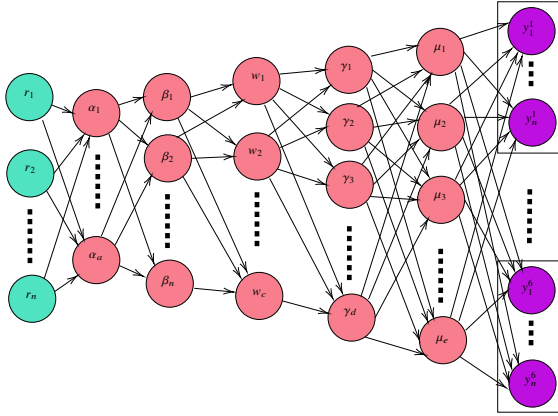


Figure 6.1: Proposed AE consisting of 5 hidden layers with hidden layer 1 acts like an encoder and the following layers combined act like a decoder.

Layer	Size
Input Layer	$n = 380$
Hidden Layer 1	$a = 190$
Hidden Layer 2	$b = 380$
Hidden Layer 3	$c = 570$
Hidden Layer 4	$d = 760$
Hidden Layer 5	$e = 950$
Output Layer	$6 \times 380 = 2280$

Table 6.1: Sizes of all layers

## 6.4.2 Learning Scheme

The input of the proposed **DNN** is the covariance matrix of the received signal as defined by eq. (2.13). In order to reduce the dimension of the input layer, we consider only the correlated elements in the covariance matrix. By exploiting the symmetry in the correlation matrix, only the strict upper or strict lower triangular part of the matrix can be considered [LZY18a]. In this design, the off-diagonal upper right matrix of the covariance matrix is considered. For example, if we have  $N = 3$  antennas, the covariance matrix will be

$$\mathbf{R} = \begin{bmatrix} r_{11} & r_{12} & r_{13} \\ r_{21} & r_{22} & r_{23} \\ r_{31} & r_{32} & r_{33} \end{bmatrix}, \quad (6.8)$$

then the following input is obtained

$$\hat{\mathbf{r}} = \begin{bmatrix} r_{12} & r_{13} & r_{23} \end{bmatrix}^T. \quad (6.9)$$

Generally, let  $\mathbf{R} \in \mathbb{C}^{N \times N}$ , then the input vector is  $\hat{\mathbf{r}} \in \mathbb{C}^{N(N-1)/2}$ . Additionally, the input of the **DNN** must be real-valued, hence,  $\hat{\mathbf{r}}$  is converted from complex to real by concatenating  $\Re(\hat{\mathbf{r}}^T)$  and  $\Im(\hat{\mathbf{r}}^T)$  such that

$$\mathbf{r} = [\Re(\hat{\mathbf{r}}^T); \Im(\hat{\mathbf{r}}^T)]^T, \quad (6.10)$$

where  $\mathbf{r} \in \mathbb{C}^n$  and  $n = N(N-1)$ . The proposed **AE** is trained to restore the rank of the matrix, which suffers from rank deficiency due to the coherent targets. Furthermore, it learns to de-noise the imperfections in the signal similar to the previous chapter. The proposed **AE** in Fig. 6.1 decomposes its input into 6 spatial subregions, each spatial subregion is a specific range of angles and all subregions are of the same size. To define these subregions, 7 particular spatial angles were chosen such as

$$\theta^{(1)} < \theta^{(1)} < \dots < \theta^{(7)} \quad (6.11)$$

with constant gaps such that  $\theta^{i+1} - \theta^i = \text{constant} \forall i, i = 1, \dots, 7$ , and each subregion  $j$  is defined as  $[\theta^j, \theta^{j+1}]$  where  $j = 1, \dots, 6$ . Therefore, if the input vector of the **AE**  $\mathbf{r}_k$  is generated using a signal impinging from targets  $k$  on the antenna array at angle  $\theta_k$  within grid  $\Theta_j$  in the  $j$ -th subregion, then the output of the  $j$ -th decoder will be  $\hat{\mathbf{r}}_k$ , which is the estimated value of  $\hat{\mathbf{r}}$ . while the output of the other decoders will be zero as there are no signals impinging from those range of angles. The **AE** is trained to be able to separate multiple signals transmitted from targets located in different subregions impinging onto the array simultaneously. Hence, it is able to decompose the input vector with components belonging to different subregions and extract the information that belongs to every subregion by retrieving it in the related decoders.



### 6.4.3 Training Process

The data set is constructed by generating  $I$  training samples of the covariance vector  $\mathbf{r}$  corresponding to single-signal scenarios. The data was generated with random angles that span all subregions. The output of each decoder is determined based on which subregion the generated  $\mathbf{r}$  belongs to. Alternatively, the decoder can be considered a spatial filter. This filter extracts the covariance vector information that belongs to a particular subregion. In order to build up the training label of the entire output of the AE, the outputs of the six decoders are concatenated as follows

$$\bar{\mathbf{y}} = [\bar{\mathbf{y}}_1^T, \dots, \bar{\mathbf{y}}_6^T]^T \quad (6.12)$$

in which  $\bar{\mathbf{y}}_j$  is the output of the  $j$  decoder. Thus, in a perfect case scenario, the output of all decoders should be the following

$$\bar{\mathbf{y}} = \left[ \mathbf{0}_{n \times 1}, \dots, \mathbf{0}, \underbrace{\tilde{\mathbf{r}}^T(\Theta_j)}_{j \text{ th subregion}}, \mathbf{0}, \dots, \mathbf{0} \right]^T. \quad (6.13)$$

To train the AE, MSE between the actual output and the expected one is used as the loss function. That is,

$$\mathbf{L}(\Theta_j) = \frac{1}{2} \|\bar{\mathbf{y}}_j - \mathbf{r}(\Theta_j)\|_2^2$$

where  $\bar{\mathbf{y}}_j$  is the output of decoder  $j$  when  $\mathbf{r}(\Theta_j)$  is the input as shown in Fig. 6.1. The optimizer used in the training process to minimize the loss function is a RMSProp optimizer [LZY18a].

### 6.4.4 Scanning

After training the network shown in Fig. 6.1, the training label in eq. (6.12) is used to estimate the original directions of the correlated targets impinging on the array<sup>1</sup>. This is done through spatial scanning of the output of each decoder (i.e., filter)  $\bar{\mathbf{y}}_j$ . The scanning phase aims at calculating the gain of each filter in all directions, in which the actual targets angles would have large gain values, while the other directions would have much smaller gains. Afterward, a threshold value is used to select the angles whose gains have peaks surpassing the threshold. The gain response of each filter is obtained by

$$g^{(j)} = |\tilde{\mathbf{r}}^H(\Theta_i) \mathbf{y}_j|, \quad j = 1, \dots, 6, \quad (6.14)$$

where the superscript  $(\bullet)^H$  is the conjugate transpose of the matrices and vectors,  $\tilde{\mathbf{r}}^H$  is the estimated value of  $\hat{\mathbf{r}}$ , and the complex version of  $\bar{\mathbf{r}}$ , while  $\mathbf{y}_j$  is the complex

<sup>1</sup>It is worth noting that it is possible to directly estimate the DOA from the input signal using a more complex DNN, but this is left for future work.

version of the output of the  $j$ -th decoder  $\bar{\mathbf{y}}_j$ .  $\mathbf{y}_j$  is obtained from  $\bar{\mathbf{y}}_j$  by concatenating the first half that represents the real values in  $\bar{\mathbf{y}}_j$  with their corresponding imaginary values in the second half of  $\bar{\mathbf{y}}_j$ , similarly  $\hat{\mathbf{r}}^H(\Theta_i)$  is obtained from  $\bar{\mathbf{r}}^T(\Theta_i)$ .

## 6.5 Numerical Analysis

In this section, we carry out simulations to evaluate our proposed DNN. We used the python library *tensorflow* to design and process our DNN. The network is trained on  $I = 1200$  samples, with learning rate of 0.001, while the batch size is 100 and the number of epochs is 1000 epochs. We use a ULA of size  $N = 20$  elements with spacing  $d = \lambda_c/2$  to predict directions of signals impinging from targets located in the spatial range of  $[-60^\circ, 60^\circ]$ , which is divided equally into six subregions. The training samples are generated randomly from the spatial range with a step of 0.1. The covariance input vector  $\mathbf{r}(\Theta_i)$  is generated using  $N_s = 800$  snapshots. To evaluate the performance of our algorithm, we use forward/backward spatial smoothing along with the SS-MUSIC in [PK89], and compared it against our DNN in multipath environment by randomly changing  $g_l$  and  $\phi_l$  in eq. (6.7) for every target  $l$ .

### 6.5.1 Gain Responses of each Decoder (i.e., Filter)

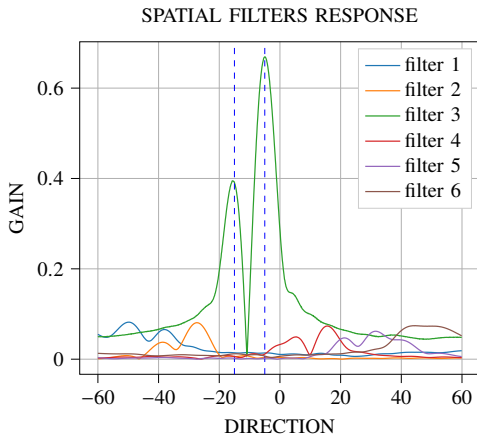


Figure 6.2: Spatial filters response at  $\text{SNR} = 10$  dB when two coherent signals located at  $(\theta_1 = -15^\circ, \theta_2 = -5^\circ)$  are incident to the antenna array. The blue dashed lines are at  $-15^\circ$  and  $-5^\circ$  respectively

The DNN is tested using a covariance vector obtained from two correlated targets located at  $\theta_1 = -15^\circ, \theta_2 = -5^\circ$  respectively, which belongs to subregion 3, i.e.

$[-20^\circ, 0^\circ]$ , with signal to noise ratio  $\text{SNR} = 10$  dB. Those specific directions were chosen, because they are in the same subregion, making them spatially close, hence it would be harder to separate them compared to distant targets. The threshold value to find the peaks in the scanning process is set to 0.3, which is set by experience. Fig. 6.2 shows the gain obtained from eq. (6.14) for all the filters. It can be depicted that the spatial gain response of the filter corresponding to the assigned subregion has higher peaks compared to the other filters. It is clear that the filter managed to differentiate between both angles despite the fact they are coherent, and the antenna array suffers from imperfection errors as stated in eq. (6.2).

### 6.5.2 Performance against Spatial Smoothing-MUSIC

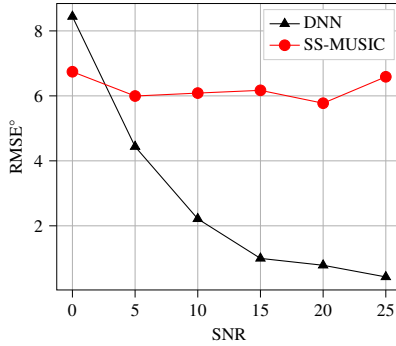


Figure 6.3: DOA estimation root mean square error (RMSE) in degrees of the proposed DNN method and SS-MUSIC algorithm for two impinging signals from directions ( $\theta_1 = -15^\circ, \theta_2 = -5^\circ$ )

Fig. 6.3 compares DOA estimation performance of our proposed DNN with SS-MUSIC in presence of correlated targets and array imperfections combined. The average RMSE in degrees is used to measure the accuracy of DOA estimates for various SNR. It can be shown from the figure that the of our DNN starts high at  $\text{SNR} = 0$  dB, then decreases significantly compared to SS-MUSIC as the SNR increases. It can be seen from the figure that the RMSE of SS-MUSIC algorithm is heavily impacted by the presence of imperfections due to the fact that it assumes an ideal steering vector model with no imperfections as in eq. (2.11). It is worth noting that the proposed machine learning method was only tested in the presence of both sources of disturbance present at the same time.

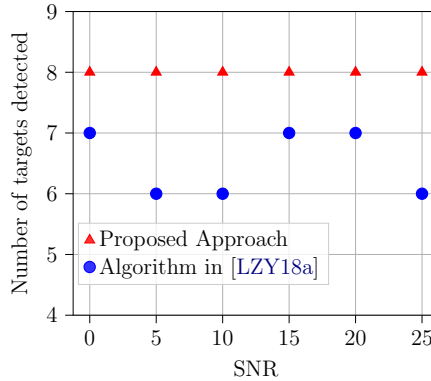


Figure 6.4: DOA estimation RMSE of the proposed DNN framework and DNN found in [LZY18a] for  $L = 8$  coherent targets

### 6.5.3 Performance against Algorithm in [LZY18a]

Fig. 6.4 compares the detection performance of our DNN compared to the algorithm in [LZY18a], where the authors only considered array imperfections and assumes perfectly uncorrelated targets for DOA estimation. The same training data was used for both algorithms for fair comparison. The figure shows a consistent behavior for our algorithm detecting all 8 targets, however, the algorithm in [LZY18a] shows a lower probability of detection due to its failure to detect all coherent targets.

## 6.6 Summary

In this chapter, we presented a framework for DOA estimation of correlated targets in presence of array imperfections. Our approach was based on Deep AE with 5 hidden layers, one acting as an encoder and 4 as a decoder. From the simulations, we showed that the AE acts as a denoiser, where it could successfully remove the effect of coherence and imperfections producing accurate DOA estimates compared to the commonly used SS-MUSIC. Moreover, we compared our algorithm with the approach in [LZY18a] where the authors only deal with imperfections, and our algorithm showed better and more consistent behavior.

# 7 Conclusion and Future Work

In this chapter, we conclude the main contributions of this thesis and outline some directions to extend the results addressed in this work.

## 7.1 Summary of Main Contributions

This dissertation shed the light on some of the major challenges facing the current radar systems as depicted in Fig. 1.1 proposing robust solutions from machine learning and information theory perspectives. This thesis studied such problem according to two main research strands (a) waveform design at the Tx side (b) DOA estimation at the Rx side. In the first main part of the thesis, chapters 3 and 4, we proposed to overcome the potential effects of the environmental undesired returns through waveform design. To this end, we proposed different strategies to tackle this problem based on the radar operation mode and the priori information available. In this context, the first radar scene examined in Chapter 3 comprised of multiple extended targets whose second order statistics are known a priori. Meanwhile, the radar's goal was to extract more information about those targets despite the presence of mutual interference resulting from the overlapping of their PSD. Therein, we proposed a joint transmit-receive beamforming design using MI as a metric through two step optimization algorithm. The results demonstrated the potential superiority of optimizing the beamformers compared to conventional beamforming, particularly when the targets are spatially close. Interestingly, the results further showed that as the targets are sufficiently far from each other, only then the conventional beamformers become optimal. Motivated by those findings, we mathematically analyzed the influence of spatial correlation on the general MI expression. We proved that MI is a Schur-convex function with respect to spatial correlation at low SNR, i.e., monotonically increasing function. Contrarily, at high SNR, the function becomes Schur-concave.

The second radar scene examined in chapter 4 proposed different environmental challenge, where the radar's goal was to detect multiple point targets within disturbance (clutter plus noise). In this regard, the surrounding environment was totally unknown and dynamic, since the targets can fade away, or change directions. We addressed this issue through proposing a RL algorithm, where the radar acts as an agent learning the environment through trial and error. In our case, the agent seeks to maximize a reward function defined in terms of the closed form asymptotic expression of the  $P_D$  as the number of virtual spatial antenna channels go to infinity. This was done through optimizing cognitive beamformers based on the feedback from the environment. The gains achieved when deploying our approach are illustrated

through simulations for different system scenarios. Our **RL** based approach showed resilient performance for targets embedded in heavy-tailed disturbance. Furthermore, the probability of detecting the low- SNR targets improved significantly compared to adaptive approaches. The proposed **RL**-based beamformer was even able to adapt to fast changing environment, where the targets angles, number, and **SNR** changed rapidly without requiring any a priori knowledge. Moreover, the robustness of the algorithm has been examined for various disturbance models, where it showed a remarkable increase in the  $P_D$  while keeping the **CFAR** property.

In the second main part of the thesis, chapters 5 and 6, we discussed possible challenges related to **DOA** estimation. Armed with data driven approaches, we addressed **DOA** algorithms common problems like poor resolution, multipath and physical array imperfections. In chapter 5, a novel strategy utilizing deep learning to emulate a large antenna array was introduced. The proposed algorithm enabled the state of the art **MUSIC** to resolve more targets using a small antenna array, enhancing the **DOA** estimation accuracy. Multiple observations were drawn from the obtained results. Most notably, the emulated array had superior resolution capabilities compared to the actual large antenna array with the same number of antennas for high angle ranges and low **SNR** values. This is due to the fact that the **DNN** has denoising capabilities, thus it can remove signal distortions. Based on those interesting findings, we were motivated to explore further advantages of such approaches in chapter 6. Therein, we used **DNN** to overcome possible signal distortions resulting from both physical antenna array imperfections and multipath. **DNN** was used to enable the state of the art **MUSIC** algorithm to detect coherent targets, mainly caused by multipath. To make the problem more practically significant, we assumed that the signal was further distorted by array imperfections, for instance, phase, gain and mutual coupling errors. The **DNN** framework was composed of an **AE** acting as a denoiser, that could remove the effects of both coherence and imperfections. The simulations showed that **DOA** performance of our approach surpassed common approaches in the literature that deal with each of those problems separately.

## 7.2 Future Work Directions

Based on our findings in this thesis, several interesting aspects may be explored further as future research directions as highlighted next:

- **MIMO Radar Waveform Design for THz Regimes** : It is expected that 6G systems will soon transition to become multi-modal systems, meaning it will evolve from communication only to an integrated joint communication and sensing. Thus, a key question here, is how the radar would be able to detect far objects within such high attenuation at 6G frequencies, mainly in the THz band. In addition, THz bands are characterized by molecular absorption loss, which is caused by water vapor. This phenomena might result in absorption peaks in the channel response. One interesting approach here, is to design the waveform to overcome such shortcoming. In addition, a reconfigurable intelligent surface

reconfigurable intelligent surface (RIS) can be designed and placed to substitute those losses. This is done through controlling the reflection of each element on the RIS to obtain a lens focusing behavior forming constructive multipath. In this context, preliminary work in joint beamforming and RIS design for radar detection is done in [C7]. Furthermore, the metric to optimize the beamformers and RIS phases can be derived using an information theoretic criteria. Kullback Leibler distance between the densities of observations under two hypothesis can be a fitting metric in this case, from a detection point of view [CT06].

- **RL based DOA for Multiple Targets:** In chapter 4, we focus our attention on the detection aspect of the radar problem, i.e., whether a point-like target exists in a certain range - angle cell. This is done through binary hypothesis testing for each cell. One research frontier is to further exploit the DOA of the targets using RL. The exploited scenarios can be reevaluated in terms of DOA estimation error. Generally, the reward function plays an important role in any RL algorithm. Thus, it would be interesting to try a different reward function in this case and examine its effect on the whole performance.
- **Non Linearity Mitigation for FMCW Radars:** In chapter 4, we dealt with unknown clutter statistics by means of RL. Likewise, such solution might be explored to mitigate one of the main issues facing Frequency modulated Continuous Waveform (FMCW) radars. The non linearity of the frequency sweep causes major degradation in the range resolution. This occurs due to imperfections in the voltage controlled oscillator (VCO) which is unknown in practice. Thus, the RL technique presented in chapter 4 can be reused in this case, where the agent, through trial and error, can learn those errors and try to correct them.





# Appendix

## A.1 Asymptotic distribution of $\Lambda_{b,\text{RW}}^k$

In general, the disturbance statistics  $\mathbf{\Gamma}_{b,k}$  is unknown. Hence according to [FSG+20, Remark 1], an estimate of  $\mathbf{\Gamma}_{b,k}$  are given by

$$\left[\widehat{\mathbf{\Gamma}}_{b,k}\right]_{i,j} = \begin{cases} \left[\hat{\mathbf{c}}_b^k\right]_i \left[\hat{\mathbf{c}}_b^k\right]_j^* & j - i \leq b \\ \left[\hat{\mathbf{c}}_b^k\right]_i^* \left[\hat{\mathbf{c}}_b^k\right]_j & i - j \leq b \\ 0 & |i - j| > b \end{cases} \quad (\text{A.1})$$

where  $\hat{\mathbf{c}}_b^k = \mathbf{y}_b^k - \hat{\alpha}_b^k \mathbf{h}_b^k$ . Generally speaking, if Assumption 1 holds, then the asymptotic distribution under  $H_0$  and  $H_1$  of the Wald statistic is [FSG+20]

$$\Lambda_{b,\text{RW}}^k(\mathbf{y}_b^k | H_0) \underset{MN \rightarrow \infty}{\overset{d}{\sim}} \chi_2^2(0), \quad (\text{A.2})$$

$$\Lambda_{b,\text{RW}}^k(\mathbf{y}_b^k | H_1) \underset{MN \rightarrow \infty}{\overset{d}{\sim}} \chi_2^2(\hat{\zeta}), \quad (\text{A.3})$$

such that

$$\hat{\zeta} = 2|\alpha_b^k|^2 \frac{\|\mathbf{h}_b^k\|^4}{(\mathbf{h}_b^k)^H \mathbf{\Gamma}_{b,k} \mathbf{h}_b^k}. \quad (\text{A.4})$$

Furthermore, under asymptotic detection performance of (A.3), a closed form expression for  $P_D$  can be formulated as

$$P_D(\lambda) \rightarrow_{N \rightarrow \infty} Q_1\left(\sqrt{\hat{\zeta}}, \sqrt{\lambda}\right), \quad (\text{A.5})$$

where  $Q_1(\cdot, \cdot)$  is first order *Marcum Q function* [Nut74]. For detailed proof, please refer to [FSG+20].

## A.2 Proof of Proposition 1

Let us write the non-convex constraint eq. (4.25) in problem (4.23) as

$$g_j(\zeta, \mathbf{W}) \leq 0 \quad \forall j \in \mathcal{T}_i \quad (\text{A.6})$$

where  $g_j(\zeta, \mathbf{W}) \triangleq \zeta - f_j(\mathbf{W})$ . In the approximate problem, we replace the constraint as written in eq. (A.6) with the constraint:

$$\tilde{g}_j(\zeta, \mathbf{W}; \widetilde{\mathbf{W}}^m) \leq 0 \quad \forall j \in \mathcal{T}_i \quad (\text{A.7})$$

such that  $\tilde{g}_j(\zeta, \mathbf{W}; \widetilde{\mathbf{W}}^m) \triangleq \zeta - \tilde{f}_j(\mathbf{W}; \widetilde{\mathbf{W}}^m) \leq 0, \forall j \in \mathcal{T}_i$ . The function  $\tilde{g}_j(\zeta, \mathbf{W}; \widetilde{\mathbf{W}}^m)$  satisfy the following properties:

- 1 The function  $\tilde{g}_j(\zeta, \mathbf{W}; \widetilde{\mathbf{W}}^m)$  is differentiable for all the values of  $\{\zeta, \widetilde{\mathbf{W}}^m\} \in \mathcal{F}$  where,  $\mathcal{F} = \{\zeta, \mathbf{W} \mid \zeta \in \mathbb{R}_+, \text{tr}(\mathbf{W}^H \mathbf{W}) = P_T\}$
- 2  $g_j(\zeta, \mathbf{W}) \leq \tilde{g}_j(\zeta, \mathbf{W}; \widetilde{\mathbf{W}}^m) \quad \forall \widetilde{\mathbf{W}}^m \in \mathcal{F}$
- 3  $g_j(\tilde{\zeta}, \widetilde{\mathbf{W}}^m) = \tilde{g}_j(\tilde{\zeta}, \widetilde{\mathbf{W}}^m; \widetilde{\mathbf{W}}^m) \quad \forall \{\tilde{\zeta}, \widetilde{\mathbf{W}}^m\} \in \mathcal{F}$
- 4  $\nabla_{\mathbf{W}} g_j(\tilde{\zeta}, \widetilde{\mathbf{W}}^m) = \nabla_{\mathbf{W}} \tilde{g}_j(\tilde{\zeta}, \widetilde{\mathbf{W}}^m; \widetilde{\mathbf{W}}^m)$

By following similar steps to [MW78], we conclude that sequence generated by algorithm 4 converges to a KKT solution of the non-convex optimization problem eq. (4.23).

# Bibliography

- [Ami17] M. Amin, *Radar for Indoor Monitoring Detection, Classification, and Assessment*, 1st ed. CRC Press, 2017.
- [BBS<sup>+</sup>15] K. L. Bell, C. J. Baker, G. E. Smith, J. T. Johnson, and M. Rangaswamy, “Cognitive radar framework for target detection and tracking,” *IEEE Journal of Selected Topics in Signal Processing*, vol. 9, no. 8, pp. 1427–1439, Dec 2015.
- [Bel88] M. Bell, “Information theory and radar : mutual information and the design and analysis of radar waveforms and systems,” Ph.D. dissertation, California Institute of Technology, 1988.
- [Bel93] M. R. Bell, “Information theory and radar waveform design,” *IEEE Transactions on Information Theory*, vol. 39, no. 5, pp. 1578–1597, Sep 1993.
- [Ber08] D. P. Bertsekas, *Non Linear Programming*, 3rd ed. Belmont, Mass, U.S.A: Athena Scientific, 2008.
- [BF03] D. W. Bliss and K. W. Forsythe, “Multiple-input multiple-output (MIMO) radar and imaging: Degrees of freedom and resolution,” in *Asilomar Conf. on SSC, 2003*, vol. 1, 2003.
- [BL98] D. K. Barton and S. A. Leonov, *Radar technology encyclopedia*. Artech house, 1998.
- [BSW<sup>+</sup>19] E. Björnson, L. Sanguinetti, H. Wymeersch, J. Hoydis, and T. L. Marzetta, “Massive MIMO is a reality-what is next?: Five promising research directions for antenna arrays,” *Digital Signal Processing*, vol. 94, pp. 3 – 20, 2019, special Issue on Source Localization in Massive MIMO.
- [Che09] S. C.-Y. Chen, “Signal Processing Algorithms for MIMO Radar,” phd, California Institute of Technology, 2009. [Online]. Available: <https://resolver.caltech.edu/CaltechETD:etd-06082009-131045>
- [CT06] T. M. Cover and J. A. Thomas, *Elements of Information Theory (Wiley Series in Telecommunications and Signal Processing)*. Wiley-Interscience, 2006.

- [FG12] L. K. P. F. Gini, A. De Maio, Ed., *Waveform Design and Diversity for Advanced Radar Systems*. London, UK: IET Press, 2012.
- [FGG16] S. Fortunati, F. Gini, and M. S. Greco, "The misspecified Cramer-Rao bound and its application to scatter matrix estimation in complex elliptically symmetric distributions," *IEEE Transactions on Signal Processing*, vol. 64, no. 9, pp. 2387–2399, 2016.
- [FGGR17] S. Fortunati, F. Gini, M. S. Greco, and C. D. Richmond, "Performance bounds for parameter estimation under misspecified models: Fundamental findings and applications," *IEEE Signal Processing Magazine*, vol. 34, no. 6, pp. 142–157, Nov 2017.
- [FHB+06] E. Fishler, A. Haimovich, R. S. Blum, L. J. Cimini, D. Chizhik, and R. A. Valenzuela, "Spatial diversity in radars-models and detection performance," *IEEE Transactions on Signal Processing*, vol. 54, no. 3, pp. 823–838, March 2006.
- [Fie71] M. Fiedler, "Bounds for the determinant of the sum of hermitian matrices," *Proceedings of the American Mathematical Society*, vol. 30, no. 1, pp. 27–31, 1971. [Online]. Available: <http://www.jstor.org/stable/2038212>
- [Fri07] B. Friedlander, "Waveform design for MIMO radars," *IEEE Transactions on Aerospace and Electronic Systems*, vol. 43, no. 3, pp. 1227–1238, 2007.
- [Fri12a] B. Friedlander, "On signal models for MIMO radar," *IEEE Transactions on Aerospace and Electronic Systems*, vol. 48, no. 4, pp. 3655–3660, October 2012.
- [Fri12b] —, "On transmit beamforming for MIMO radar," *IEEE Transactions on Aerospace and Electronic Systems*, vol. 48, no. 4, pp. 3376–3388, October 2012.
- [FS08] D. R. Fuhrmann and G. San Antonio, "Transmit beamforming for MIMO radar systems using signal cross-correlation," *IEEE Transactions on Aerospace and Electronic Systems*, vol. 44, no. 1, pp. 171–186, 2008.
- [FSG+20] S. Fortunati, L. Sanguinetti, F. Gini, M. S. Greco, and B. Himed, "Massive MIMO radar for target detection," *IEEE Transactions on Signal Processing*, vol. 68, pp. 859–871, 2020.
- [FW91] B. Friedlander and A. J. Weiss, "Direction finding in the presence of mutual coupling," *IEEE Transactions on Antennas and Propagation*, vol. 39, no. 3, pp. 273–284, March 1991.
- [GB14] M. Grant and S. Boyd, "CVX: Matlab software for disciplined convex programming, version 2.1," <http://cvxr.com/cvx>, Mar. 2014.

- [GDH<sup>+</sup>15] L. Guo, H. Deng, B. Himed, T. Ma, and Z. Geng, "Waveform optimization for transmit beamforming with MIMO radar antenna arrays," *IEEE Transactions on Antennas and Propagation*, vol. 63, no. 2, pp. 543–552, 2015.
- [GGDD20] A. Guerra, F. Guidi, D. Dardari, and P. M. Djuric, "Reinforcement learning for uav autonomous navigation, mapping and target detection," *CoRR*, May 2020. [Online]. Available: <http://arxiv.org/abs/2005.05057>
- [GGSB18] M. S. Greco, F. Gini, P. Stinco, and K. Bell, "Cognitive radars: On the road to reality: Progress thus far and possibilities for the future," *IEEE Signal Processing Magazine*, vol. 35, no. 4, pp. 112–125, 2018.
- [Gin21] F. Gini, "Grand challenges in radar signal processing," *Frontiers in Signal Processing*, vol. 1, p. 1, 2021. [Online]. Available: <https://www.frontiersin.org/article/10.3389/frsip.2021.664232>
- [Gue10] J. R. Guerci, "Cognitive radar: A knowledge-aided fully adaptive approach," in *2010 IEEE Radar Conference*, May 2010, pp. 1365–1370.
- [GVN07] N. A. Goodman, P. R. Venkata, and M. A. Neifeld, "Adaptive waveform design and sequential hypothesis testing for target recognition with active sensors," *IEEE Journal of Selected Topics in Signal Processing*, vol. 1, no. 1, pp. 105–113, 2007.
- [Hay06] S. Haykin, "Cognitive radar: a way of the future," *IEEE Signal Processing Magazine*, vol. 23, no. 1, pp. 30–40, Jan 2006.
- [HBC08] A. M. Haimovich, R. S. Blum, and L. J. Cimini, "MIMO radar with widely separated antennas," *IEEE Signal Processing Magazine*, vol. 25, no. 1, pp. 116–129, 2008.
- [HBH10] Q. He, R. S. Blum, and A. M. Haimovich, "Noncoherent mimo radar for location and velocity estimation: More antennas means better performance," *IEEE Transactions on Signal Processing*, vol. 58, no. 7, pp. 3661–3680, 2010.
- [Hua] Huawei. Huawei launches 5g simplified solution. [Online]. Available: <https://www.huawei.com/en/press-events/news/2019/2/huawei-5g-simplified-solution>
- [HV11] A. Hassanien and S. A. Vorobyov, "Transmit energy focusing for DOA estimation in MIMO radar with colocated antennas," *IEEE Trans. Signal Process.*, vol. 59, no. 6, pp. 2669–2682, 2011.
- [Hwa79] F. K. Hwang, "Majorization on a partially ordered set," *Proceedings of the American Mathematical Society*, vol. 76, no. 2, pp. 199–203, 1979. [Online]. Available: <http://www.jstor.org/stable/2042988>

- [HXS12] S. Haykin, Y. Xue, and P. Setoodeh, "Cognitive radar: Step toward bridging the gap between neuroscience and engineering," *Proceedings of the IEEE*, vol. 100, no. 11, pp. 3102–3130, Nov 2012.
- [IB05] P. Ioannides and C. A. Balanis, "Uniform circular arrays for smart antennas," *IEEE Antennas and Propag. Mag.*, vol. 47, no. 4, pp. 192–206, 2005.
- [JB07] E. A. Jorswieck and H. Boche, *Majorization and Matrix Monotone Functions in Wireless Communications*, ser. Foundations and Trends in Communications and Information Theory. Now Publishers, Jul. 2007, vol. 3, no. 6.
- [JHS19] W. Jiang, A. M. Haimovich, and O. Simeone, "End-to-end learning of waveform generation and detection for radar systems," in *2019 53rd Asilomar Conference on Signals, Systems, and Computers*, 2019, pp. 1672–1676.
- [JLY16] H. Jiang, Y. Lu, and S. Yao, "Random matrix based method for joint DOD and DOA estimation for large scale MIMO radar in non-Gaussian noise," in *2016 IEEE International Conference on Acoustics, Speech and Signal Processing (ICASSP)*, March 2016, pp. 3031–3035.
- [KB10] D. Khan and K. L. Bell, "Analysis of DOA estimation performance of sparse linear arrays using the Ziv-Zakai bound," in *IEEE Radar Conf.*, 2010.
- [LAA14] J. Lipor, S. Ahmed, and M.-S. Alouini, "Fourier-based transmit beam pattern design using MIMO radar," *IEEE Transactions on Signal Processing*, vol. 62, pp. 2226–2235, 2014.
- [LDL11] Y. F. Liu, Y. H. Dai, and Z. Q. Luo, "Coordinated beamforming for miso interference channel: Complexity analysis and efficient algorithms," *IEEE Transactions on Signal Processing*, vol. 59, no. 3, pp. 1142–1157, March 2011.
- [LLH14a] J. Liu, H. Li, and B. Himed, "Joint optimization of transmit and receive beamforming in active arrays," *IEEE Signal Processing Letters*, vol. 21, no. 1, pp. 39–42, Jan 2014.
- [LLH14b] —, "Joint design of transmit and receive beamforming for interference mitigation," in *2014 International Radar Conference*, Oct 2014, pp. 1–5.
- [LLH<sup>+</sup>19] P. Liu, Y. Liu, T. Huang, Y. Lu, and X. Wang, "Cognitive radar using reinforcement learning in automotive applications," *CoRR*, vol. abs/1904.10739, 2019. [Online]. Available: <http://arxiv.org/abs/1904.10739>

- 
- [LMS<sup>+</sup>10] Z. Luo, W. Ma, A. M. So, Y. Ye, and S. Zhang, “Semidefinite relaxation of quadratic optimization problems,” *IEEE Signal Processing Magazine*, vol. 27, no. 3, pp. 20–34, 2010.
- [LNN07] A. Leshem, O. Nappartek, and A. Nehorai, “Information theoretic adaptive radar waveform design for multiple extended targets,” *IEEE Journal of Selected Topics in Signal Processing*, vol. 1, no. 1, pp. 42–55, June 2007.
- [LS07] J. Li and P. Stoica, “MIMO radar with colocated antennas,” *IEEE Signal Process. Mag.*, vol. 24, no. 5, pp. 106–114, Sep. 2007.
- [LS08] J. Li and P. Stoica, *MIMO Radar Signal Processing*. Wiley, 2008.
- [LSXR07] J. Li, P. Stoica, L. Xu, and W. Roberts, “On parameter identifiability of MIMO radar,” *IEEE Signal Process. Lett.*, vol. 14, no. 12, pp. 968–971, 2007.
- [LV18] C. Liu and P. P. Vaidyanathan, “Comparison of sparse arrays from viewpoint of coarray stability and robustness,” in *IEEE 10th SAM*, 2018, pp. 36–40.
- [LWS05] J. Li, Z. Wang, and P. Stoica, *Robust Adaptive Beamforming*, 2005, ch. 3, pp. 91–200.
- [LY06] M. Lin and L. Yang, “Blind calibration and DOA estimation with uniform circular arrays in the presence of mutual coupling,” *IEEE Antennas and Wireless Propagation Letters*, vol. 5, pp. 315–318, 2006.
- [LYL<sup>+</sup>17] S. Lee, Y. Yoon, J. Lee, H. Sim, and S. Kim, “Two-stage DOA estimation method for low SNR signals in automotive radars,” *IET Radar, Sonar Navigation*, vol. 11, no. 11, pp. 1613–1619, 2017.
- [LZY18a] Z. Liu, C. Zhang, and P. S. Yu, “Direction-of-arrival estimation based on deep neural networks with robustness to array imperfections,” *IEEE Transactions on Antennas and Propagation*, vol. 66, no. 12, pp. 7315–7327, Dec 2018.
- [LZY18b] —, “Direction-of-arrival estimation based on deep neural networks with robustness to array imperfections,” *IEEE Trans. Antennas Propag.*, vol. 66, no. 12, pp. 7315–7327, 2018.
- [Mar10] T. L. Marzetta, “Noncooperative cellular wireless with unlimited numbers of base station antennas,” *IEEE Transactions on Wireless Communications*, vol. 9, no. 11, pp. 3590–3600, November 2010.

- [MBH15] J. Metcalf, S. D. Blunt, and B. Himed, "A machine learning approach to cognitive radar detection," in *2015 IEEE Radar Conference (RadarCon)*, May 2015, pp. 1405–1411.
- [Mck] Mckinsey. Automotive revolution: perspective towards 2030. Accessed: 30 Sept 2021. [Online]. Available: <https://www.mckinsey.com/industries/automotive-and-assembly/our-insights/disruptive-trends-that-will-transform-the-auto-industry/de-DE>
- [Mie17] J. Mietzner, "MIMO arrays versus conventional thin arrays for 2D and 3D radar applications," in *EURAD*, 2017.
- [MOA11] A. W. Marshall, I. Olkin, and B. C. Arnold, *Inequalities: Theory of Majorization and its Applications*, 2nd ed. Springer, 2011, vol. 143.
- [Mof68] A. Moffet, "Minimum-redundancy linear arrays," *IEEE Trans. on Antennas and Propag.*, vol. 16, no. 2, pp. 172–175, 1968.
- [MRT12] M. Mohri, A. Rostamizadeh, and A. Talwalkar, *Foundations of Machine Learning*. The MIT Press, 2012.
- [MW78] B. R. Marks and G. P. Wright, "A general inner approximation algorithm for nonconvex mathematical programs," *Operations Research*, vol. 26, no. 4, pp. 681–683, 1978. [Online]. Available: <http://www.jstor.org/stable/169728>
- [NSW09] U. Niesen, D. Shah, and G. W. Wornell, "Adaptive alternating minimization algorithms," *IEEE Transactions on Information Theory*, vol. 55, no. 3, pp. 1423–1429, March 2009.
- [Nut74] A. H. Nuttall, "Some integrals involving the (q sub m)-function," 1974.
- [OMBK17] J. Ochodnický, Z. Matousek, M. Babjak, and J. Kurty, "Drone detection by Ku-band battlefield radar," in *2017 International Conference on Military Technologies (ICMT)*, May 2017, pp. 613–616.
- [PK89] U. Pillai and B. Kwon, "Forward/backward spatial smoothing techniques for coherent signal identification," *IEEE Transactions on Signal Processing*, vol. 37, no. 1, pp. 8–15, 1 1989.
- [PM17] D. Poole and A. Mackworth, *Artificial Intelligence: Foundations of Computational Agents*, 2nd ed. Cambridge, UK: Cambridge University Press, 2017. [Online]. Available: <http://artint.info/2e/html/ArtInt2e.html>
- [PV10] P. Pal and P. P. Vaidyanathan, "Nested arrays: A novel approach to array processing with enhanced degrees of freedom," *IEEE Trans. on Signal Process.*, vol. 58, no. 8, pp. 4167–4181, 2010.



- [PV11] —, “Copriime sampling and the MUSIC algorithm,” in *DSP/SPE*, 2011, pp. 289–294.
- [QR11a] Qing Chen and Ruolun Liu, “On the explanation of spatial smoothing in music algorithm for coherent sources,” in *International Conference on Information Science and Technology*, March 2011, pp. 699–702.
- [QR11b] —, “On the explanation of spatial smoothing in music algorithm for coherent sources,” in *International Conference on Information Science and Technology*, March 2011, pp. 699–702.
- [QZA15] S. Qin, Y. D. Zhang, and M. G. Amin, “Generalized coprime array configurations for direction-of-arrival estimation,” *IEEE Trans. on Signal Process.*, vol. 63, no. 6, pp. 1377–1390, 2015.
- [RBG11] R. A. Romero, J. Bae, and N. A. Goodman, “Theory and application of snr and mutual information matched illumination waveforms,” *IEEE Transactions on Aerospace and Electronic Systems*, vol. 47, no. 2, pp. 912–927, 2011.
- [SB18] R. S. Sutton and A. G. Barto, *Reinforcement Learning: An Introduction*, 2nd ed. The MIT Press, 2018. [Online]. Available: <http://incompleteideas.net/book/the-book-2nd.html>
- [Sch15] J. Schmidhuber, “Deep learning in neural networks: An overview,” *Neural Networks*, vol. 61, pp. 85 – 117, 2015.
- [SFL<sup>+</sup>16] G. Scutari, F. Facchinei, L. Lampariello, P. Song, and S. Sardellitti, “Parallel and distributed methods for nonconvex optimization-part II: applications,” *CoRR*, vol. abs/1601.04059, 2016. [Online]. Available: <http://arXiv.org/abs/1601.04059>
- [Sha48] C. E. Shannon, “A Mathematical Theory of Communication,” *Bell System Technical Journal*, vol. 27, no. 3, pp. 379–423, Jul. 1948. [Online]. Available: <https://ieeexplore.ieee.org/document/6773024>
- [Sva99] T. Svantesson, “Modeling and estimation of mutual coupling in a uniform linear array of dipoles,” in *1999 IEEE International Conference on Acoustics, Speech, and Signal Processing. Proceedings. ICASSP99*, vol. 5, March 1999, pp. 2961–2964.
- [Swe60] P. Swerling, “Probability of detection for fluctuating targets,” *IRE Trans. on Inf. Theory*, vol. 6, no. 2, pp. 269–308, April 1960.
- [TC13] S. Theodoridis and R. Chellappa, *Academic Press Library in Signal Processing, Volume 3: Array and Statistical Signal Processing*, 1st ed. Orlando, FL, USA: Academic Press, Inc., 2013.

- [Tre02] H. L. V. Trees, *Optimum Array Processing: Part IV of Detection, Estimation, and Modulation Theory*. John Wiley and Sons, Ltd, 2002.
- [TTP10] B. Tang, J. Tang, and Y. Peng, "MIMO radar waveform design in colored noise based on information theory," *IEEE Transactions on Signal Processing*, vol. 58, no. 9, pp. 4684–4697, Sept 2010.
- [UY16] M. Ulrich and B. Yang, "Multi-carrier MIMO radar: A concept of sparse array for improved DOA estimation," in *IEEE Radar Conf.*, 2016.
- [VML15] P. Vallet, X. Mestre, and P. Loubaton, "Performance analysis of an improved MUSIC DoA estimator," *IEEE Trans. Signal Process.*, vol. 63, no. 23, pp. 6407–6422, 2015.
- [WD53] P. M. Woodward and I. L. Davies, Eds., *Probability and Information theory with Applications to Radar*. London, U.K: Pergamon, 1953.
- [WFGG18] L. Wang, S. Fortunati, M. S. Greco, and F. Gini, "Reinforcement learning-based waveform optimization for MIMO multi-target detection," in *2018 52nd Asilomar Conference on Signals, Systems, and Computers*, Oct 2018, pp. 1329–1333.
- [WYWL14] X. Wang, S. Yang, X. Wang, and X. Lin, "Concurrent exploration of MIMO radar and co-prime array for faster and higher resolution scanning," in *Asilomar Conf. on Signals, Systems and Computers*, 2014.
- [WZLT18] L. Wang, Y. Zhang, Q. Liao, and J. Tang, "Robust waveform design for multi-target detection in cognitive MIMO radar," in *2018 IEEE Radar Conference (RadarConf18)*, April 2018, pp. 0116–0120.
- [WZY+18] X. Wang, W. Zhang, J. Yan, X. Yuan, and H. Zha, "On the flexibility of block coordinate descent for large-scale optimization," *Neurocomputing*, vol. 272, no. Supplement C, pp. 471 – 480, 2018. [Online]. Available: <http://www.sciencedirect.com/science/article/pii/S0925231217312705>
- [YB07] Y. Yang and R. S. Blum, "MIMO radar waveform design based on mutual information and minimum mean-square error estimation," *IEEE Transactions on Aerospace and Electronic Systems*, vol. 43, no. 1, pp. 330–343, January 2007.
- [Zhe17] G. Zheng, "DOA estimation in MIMO radar with non-perfectly orthogonal waveforms," *IEEE Commun. Lett.*, vol. 21, no. 2, pp. 414–417, 2017.
- [ZZY08] F. Zhou, D. Zhou, and G. Yu, "Target tracking in interference environments reinforcement learning and design for cognitive radar soft processing," in *2008 Congress on Image and Signal Processing*, vol. 4, May 2008, pp. 73–77.

# Curriculum Vitae

Name: Aya Mostafa Ibrahim Ahmed  
Date of birth: August 1, 1988  
Place of birth: Cairo, Egypt

## Education

02/2017 – 2022 **PhD program**, Ruhr-Universität Bochum  
03/2014 – 03/2015 **Master of Science (M.Sc.)**, Electrical Engineering and Information Technology, German University in Cairo (GUC), Egypt  
09/2006 – 07/2011 **Bachelor of Science (B.Sc.)**, Electrical Engineering and Information Technology, German University in Cairo (GUC), Egypt  
1993 – 06/2006 Notre Dame-Gymnasium, Cairo, Egypt

## Work Experience

02/2017 – 2022 **Research Assistant**, Lehrstuhl für Digitale Kommunikationssysteme  
07/2012 – 12/2016 **Senior VAS Engineer**, Vodafone Egypt  
12/2011 – 06/2012 **NMC Internet and Data Engineer**, Vodafone Egypt  
10/2011 – 12/2011 **IP Network Trainee**, Professional Services - Raya Integration Company  
07/2007 – 10/2007 **IP Network Trainee**, Star Communications - GPP Communications and Network department



# List of Publications

## Peer-Reviewed Journal Publications

- [J1] A. M. Ahmed, A. Alameer, D. Erni and A. Sezgin, "Maximizing Information Extraction of Extended Radar Targets Through MIMO Beamforming," *IEEE Geoscience and Remote Sensing Letters*, vol. 16, no. 4, pp. 539-543, April 2019.
- [J2] A. M. Ahmed, U. S. K. P. Miriya Thanthrige, A. El Gamal and A. Sezgin, "Deep Learning for DOA Estimation in MIMO Radar Systems via Emulation of Large Antenna Arrays," *IEEE Comm. Letters.*, vol. 25, no. 5, pp. 1559-1563, May 2021.
- [J3] A. M. Ahmed, A. A. Ahmad, S. Fortunati, A. Sezgin, M. S. Greco and F. Gini, "A Reinforcement Learning based approach for Multi-target Detection in Massive MIMO radar," *IEEE Trans. on Aerospace and Electronic Systems.*, vol. 57, no. 5, pp. 2622-2636, Oct. 2021.
- [J4] P. Hillger, M. van Delden, U.S.M. Thanthrige, A.M. Ahmed et al., "Toward Mobile Integrated Electronic Systems at THz Frequencies," *Journal of Infrared Milli Terahz Waves*, vol. 41, pp. 846-869, July 2020.

## Peer-Reviewed Conference Publications

- [C1] A. M. Ahmed, O. Eissa and A. Sezgin, "Deep Autoencoders for DOA Estimation of Coherent Sources using Imperfect Antenna Array," *3rd International Workshop on Mobile Terahertz Systems (IWMTS)*, Essen, Germany, 2020, pp. 1-5.
- [C2] A. M. Ahmed, A. Sezgin and E. A. Jorswieck, "Impact of Spatial Correlation in MIMO Radar," *Asilomar Conference on Signals, Systems, and Computers*, CA, USA, 2019, pp. 1528-1533.
- [C3] A. M. Ahmed, S. Fortunati, A. Sezgin, M. S. Greco and F. Gini, "Robust Reinforcement Learning-based Wald-type Detector for Massive MIMO Radar," *European Signal Processing Conference (Eusipco)*, Dublin, Ireland, August 2021, pp. 846-850.

- [C4] J. Witte-meier, A. M. Ahmed, T. N. Tran, A. Sezgin and N. Pohl, “3D Localization Using a Scalable FMCW MIMO Radar Design,” *German Microwave Conference (GeMic)*, Cottbus, Germany, 2020, pp. 100-103.
- [C5] U. S. M. Thantrige, A. M. Ahmed and A. Sezgin, “Supervised Learning based Super-Resolution DoA Estimation utilizing Antenna Array Extrapolation,” *IEEE 91st Vehicular Technology Conference (VTC2020-Spring)*, Antwerp, Belgium, 2020, pp. 1-5.
- [C6] M. H. Hassan, A. A. Abbas, A. Jimenez-Saéz and A. M. Ahmad, et al., “Passive Orbital Angular Momentum RFID Tag based on Dielectric Resonator Arrays,” *3rd International Workshop on Mobile Terahertz Systems (IWMTS)*, Essen, Germany, 2020, pp. 1-4.
- [C7] E. Čišija, A. M. Ahmed, A. Sezgin and H. Wymeersch, “Ris-Aided mmWave MIMO Radar System for Adaptive Multi-Target Localization,” *2021 IEEE Statistical Signal Processing Workshop (SSP)*, Rio de Janeiro, Brazil, 2021, pp. 196-200.